

OPTICALLY-PUMPED CW MID-INFRARED NH_3 LASERS

by

CLAUDE ROLLAND, B.Sc., M.Sc.

A Thesis

Submitted to the School of Graduate Studies

in Partial Fulfilment of the Requirements

for the Degree

Doctor of Philosophy

McMaster University

© September 1984

OPTICALLY-PUMPED CW MID-INFRARED NH_3 LASERS

DOCTOR OF PHILOSOPHY (1984)
(Physics)

McMASTER UNIVERSITY
Hamilton, Ontario

TITLE: Optically-Pumped CW Mid-Infrared NH_3 Lasers

AUTHOR: Claude Rolland, B.Sc. (Université de Montréal)

M.Sc. (McMaster University)

SUPERVISORS: Professor J. Reid and Professor B.K. Garside

NUMBER OF PAGES: xvii, 135

ABSTRACT

The work presented in this thesis concerns the development and characterization of the first optically-pumped continuous (cw) lasers in the mid-infrared. Ammonia is chosen as the active lasing medium, and this research describes experiments in which NH_3 is pumped both off- and on-resonance with a CO_2 laser using several innovative techniques. The new lasers provide efficient, powerful and line-tunable cw radiation in a region (10 to 30 μm) where such sources are scarce.

Initial experiments were performed with several off-resonantly pumped 12- μm NH_3 transitions and, at low pumping powers, a Raman two-photon process was identified as the dominant mechanism responsible for the gain. The two-photon process results from the coherent interaction of two laser fields with a three-level system and can create gain in the absence of a population inversion. This property was essential to the successful operation of the first optically-pumped cw laser in the mid-infrared as the available pump intensity was insufficient to produce a population inversion.

A detailed understanding of this new cw laser was achieved by probing the small-signal gain with a tunable diode laser in an amplifier cell. A theoretical model based on a density matrix formalism approach was developed and good agreement was found between experiment and theory. The tunable diode laser measurements emphasized the importance of the pump intensity in determining the magnitude of the Raman gain. Following this study, an optimized 12- μm cavity was constructed in which

the pump intensity was maximized by using a small capillary tube.

Quantum efficiencies as high as 45% and output powers up to 10.5 W were obtained.

Line-tunability between 10.7 and 13.3 μm was accomplished with a novel pumping scheme. The frequency of the CO_2 laser is shifted into coincidence with the line center of an NH_3 transition using acousto-optic modulators. This on-resonance pumping enabled us to create a vibrational inversion between the NH_3 ground state and the upper vibrational level $v_2=1$. By adding a buffer gas, gain was obtained in the entire P- and Q-branches. A simple model which assumes thermalization among the rotational levels fully accounts for the lasing behavior.

ACKNOWLEDGEMENTS

I wish to express my deep appreciation to my supervisors, Dr. J. Reid and Dr. B.K. Garside for their guidance and support throughout the course of this work.

I would like to thank my colleagues at McMaster, past and present, who have actively contributed to the accomplishment of this work and to whom I am indebted for their generous help and collaboration. Many thanks are also due to Kathy Goodram, for her excellent typing of this thesis and to Mr. David Kroeker for his critical reading of this manuscript.

Finallement à Sonja, un gros merci pour les encouragements qu'elle m'a apportés dans les moments difficiles.

TABLE OF CONTENTS

	Page
CHAPTER 1 INTRODUCTION	1
CHAPTER 2 THEORY	10
2.1 Introduction	10
2.2 NH ₃ Molecular Structure	10
2.3 Energy Diagram and Selection Rules	11
2.4 The Density Matrix Formalism	14
2.4.1 Theory of two laser fields interacting with a three-level system	15
2.4.2 Laser transition and input data	20
2.4.3 Model predictions	24
2.5 Summary	27
CHAPTER 3 PRELIMINARY EXPERIMENTS	29
3.1 Introduction	29
3.2 12- μ m Raman Lasers Pumped by Low-Power CO ₂ Laser Pulses	29
3.2.1 Experimental apparatus and results	32
3.3 CW Optically-Pumped 12.08- μ m Laser	38
3.3.1 Results	41
3.4 Discussion and Conclusions	45
CHAPTER 4 INVESTIGATIONS OF THE 12- μ m SMALL-SIGNAL GAIN	47
4.1 Introduction	47
4.2 Experimental Technique and Preliminary Results	48
4.3 Detailed Small-Signal Gain Measurements	58

	Page
4.4 Discussion and Conclusions	68
CHAPTER 5 HIGH POWER CW 12- μ m NH_3 LASER	70
5.1 Introduction	70
5.2 Experimental Apparatus and Results	71
5.3 Extension to Other NH_3 Transitions	82
5.4 Summary	83
CHAPTER 6 GAIN SATURATION IN CW 12- μ m NH_3 RAMAN LASERS	85
6.1 Introduction	85
6.2 Experimental Apparatus	86
6.3 Results	89
6.4 Discussion and Conclusions	99
CHAPTER 7 LINE-TUNABLE OSCILLATION OF A CW NH_3 LASER	102
7.1 Introduction	102
7.2 Theory	103
7.3 Experimental Apparatus and Results	107
7.4 Future Prospects	116
7.5 Summary	119
CHAPTER 8 CONCLUSIONS	120
APPENDIX A DENSITY MATRIX SOLUTION	126
REFERENCES	129

LIST OF FIGURES

	Page
Fig. 1.1: Typical energy level structure of an optically-pumped molecule. In one case, the ground state is pumped and FIR lasing occurs between two rotational levels ($J' \rightarrow J''(\text{FIR})$) within the same excited vibrational state. In the MIR case, the emission is a vibrational-rotational transition ($J' \rightarrow J''(\text{MIR})$). Also shown are typical thermal populations relative to the pumped level population of 100.	2
Fig. 2.1: Energy levels of the lower vibrational modes in NH_3 . The values of the corresponding inversion doubling are also given.	12
Fig. 2.2: Energy level scheme for an optically-pumped MIR laser. ω_{02} and ω_{01} are the pump and lasing transition frequencies respectively, ω_p and ω_{mir} represent the field frequencies and ρ_{00} , ρ_{11} , ρ_{22} correspond to the population in levels 0, 1 and 2, respectively.	16
Fig. 2.3: Vibrational-rotational energy levels of NH_3 relevant to 12.08- μm lasing. The insert is a high-resolution NH_3/CO_2 absorption spectrum taken near 1084.6 cm^{-1} . The CO_2 absorption is indicated by the arrow. The other absorption peaks belong to the $\text{SR}(5,K)$ mani-	22

fold of NH_3 . The offset between the R(30) and sR(5,0) line center is $\Delta\nu_p = 190 \pm 7$ MHz.

Fig. 2.4: Small-signal gain profile for co- and counter-propagating 9- and 12- μm beams calculated using the computer code. The small-signal gain is plotted as a function of the lasing offset frequency ($\Omega_{01} - \omega_{\text{mir}}$). The pump intensity is 500 W/cm^2 at an ammonia pressure of 500 mTorr. The pump offset is equal to 190 MHz. Note the large reduction in the peak value and the wider gain linewidth obtained in the counter-propagating case.

Fig. 3.1: Relevant energy levels of the four NH_3 transitions investigated. $\Delta\nu_p$ represents the pump offset frequency.

Fig. 3.2: Schematic diagram of the experimental apparatus used to pump NH_3 with low-power CO_2 laser pulses. Mirror M_2 is mounted on a piezoelectric translator (Pzt).

Fig. 3.3: Small-signal absorption of the 12.81- μm laser as a function of the square of the NH_3 pressure in an external cell. The solid line is a best fit to the experimental data using a lasing offset frequency of 1.47 GHz. The dashed line indicates the large absorption which would be observed if the 12.81- μm laser was operating at line center.

Fig. 3.4: Schematic diagram of the optically-pumped ring laser.

The solid line indicates the path taken by the pump radiation while the 12.08- μm copropagating wave follows the dashed line.

Fig. 3.5: Absorption coefficient of the cw 12.08- μm laser as a function of the square of the NH_3 pressure in an external cell. The solid line is a best fit to the experimental data using a lasing offset frequency of 170 MHz and Taylor's calculated values for line strength and linewidth [41]. 42

Fig. 3.6: Chopped 12.08- μm output as a function of the MIR resonator length. The lower trace displays the linear ramp applied to the MIR piezoelectric translator. The horizontal scale is 3.7 MHz per division. 44

Fig. 4.1: Simplified energy level diagram of NH_3 . The insert as a TDL scan of the $\text{sR}(5, \text{K})$ multiplet in NH_3 near 1084.6 cm^{-1} . Also shown is the $\text{R}(30) \text{ CO}_2$ absorption line indicated by an arrow. The relevant energy levels of the transitions with the two smallest pump offsets are illustrated below. 49

Fig. 4.2: Schematic diagram of the apparatus used for the copropagating small-signal gain measurements. The pump CO_2 beam is represented by a dashed line and the probe TDL beam by a solid line. Dichroic mirrors M_1 and M_2 transmit 90% of the 9- μm CO_2 radiation and reflect 97% of the 12- μm beam. Two types of cell are 51

probed; either a large diameter cell or a waveguide capillary tube. The Freon cell is used to prevent residual CO_2 radiation from reaching the HgCdTe detector.

Fig. 4.3: TDL scan of the $\text{SP}(7,0)$ and $\text{SP}(7,1)$ transitions in the presence of CO_2 radiation. The two sharp spikes offset from the line center absorptions are the Raman transitions associated with the $\text{SP}(7,0)$ and $\text{SP}(7,1)$ lines. The pump and TDL probe beams are copropagating in a 60-cm long waveguide. Pump intensity is $\sim 1 \text{ kW/cm}^2$ at an NH_3 pressure of $\sim 800 \text{ mTorr}$. 53

Fig. 4.4: High-sensitivity scans of $12\text{-}\mu\text{m}$ Raman gain. The CO_2 laser is chopped and the TDL beam synchronously detected. Results are given for co- and counter-propagating beams in $\sim 400\text{-mTorr}$ NH_3 . Average pump intensity is $\sim 200 \text{ W/cm}^2$. The line centers of both the $\text{SP}(7,0)$ and $\text{SP}(7,1)$ lines are indicated with arrows. In each trace, the Raman feature near the $\text{SP}(7,1)$ line is shown on an expanded scale. In addition to the indicated amplitude expansion, the wave number scale has been expanded in the upper trace by a factor of 4. The signals observed near the $\text{SP}(7,0)$ and $\text{SP}(7,1)$ line centers are discussed in the text. 55

Fig. 4.5:	Comparison of experimental and theoretical spectra near the $\text{SP}(7,0)$ transition. The solid line is a conventional TDL scan taken with 500 mTorr of NH_3 in a 15-cm long waveguide. The calculated spectrum (\bullet) uses a pump intensity of 900 W/cm^2 to best fit the experimental peak gain. The sloping background caused by the TDL is included in the calculation.	Page 57
Fig. 4.6:	Differential scans of the $\text{SP}(7,0)$ region taken to illustrate the frequency tuning of the Raman gain. Results are shown as the CO_2 laser is tuned from -25 to 50 MHz around the line center. The TDL signal in the bottom trace was expanded by a factor of 2. The measurements were made in the 26-cm open cell at an NH_3 pressure of only ~ 300 mTorr to minimize pressure broadening.	59
Fig. 4.7:	Raman gain coefficient as a function of pump intensity measured in a 15-cm long waveguide at a constant pressure of 500 mTorr. The best fit straight line through the data gives a slope of $3.04 \times 10^{-5} \text{ cmW}^{-1}$.	62
Fig. 4.8:	Raman gain coefficient as a function of NH_3 pressure for copropagating beams. The low-pressure range is displayed in (a) and the high-pressure in (b).	64
Fig. 4.9:	Raman gain coefficient as a function of NH_3 pressure for counterpropagating beams.	65
Fig. 5.1:	Schematic diagram of the optically-pumped 12- μm waveguide laser.	72

	Page
Fig. 5.2: 12- μm output power as a function of NH_3 pressure for an input power of 31 W at 9 μm . The 1.2-m long capillary tube was not cooled for these measurements.	77
Fig. 5.3: 12- μm output power as a function of the total gas pressure. Measurements are shown in pure NH_3 (o) and for NH_3/He mixtures of 1:2 (x) and 1:20 (\square), respectively. The measurements were made in a 60-cm long tube at room temperature with a pump power of 38 W. Note that the maximum 12- μm power does not increase when the NH_3 is diluted with the buffer gas.	78
Fig. 5.4: 12- μm output power as a function of pump power for a room temperature (o) and with dry ice cooled (x), 1.2 m-long, 2.5-mm bore waveguide cavity. Most of the results were taken with a 1/5th duty cycle chopper. Also shown are measurements with a 1/2 duty cycle (\square) and without a chopper (\blacksquare). The chopped values have been scaled by the duty cycle to give cw values.	79
Fig. 6.1: Schematic diagram of the apparatus used to measure saturation of the 12.08- μm Raman gain. The dichroic mirrors (DM) transmit 90% of the 9- μm pump radiation, and reflect 97% of the 12.08- μm radiation.	87
Fig. 6.2: Experimental measurements of Raman gain coefficients at 12 μm . Measurements were made as a function of NH_3 pressure in a 56-cm long, 1.5-mm bore capillary	90

tube. The incident CO_2 power in the waveguide was 14 W, and the 12- μm probe signal was varied from 3.2 W (saturated gain) to <10 mW (small-signal gain).

Fig. 6.3: Experimental and calculated values of Raman gain coefficients in a 10-cm long, 1.5-mm bore capillary tube. Pump and probe powers incident in the waveguide are 14 W and 2.7 W, respectively. Calculated values are given for the relaxation rate $\gamma = 25 \times 10^6 \text{ s}^{-1} \text{ Torr}^{-1}$ and use the radial intensity distributions (normalized to the waveguide radius a) given in the inserts. The calculated values are scaled by a factor of 0.5 (see text). 92

Fig. 6.4: Ratio of saturated gain to small-signal gain, g_{sat}/g_0 as a function of incident 12- μm power. Measurements are made in the 56-cm long, 1.5-mm bore waveguide with 14 W of 9- μm pump power. Calculations are carried out using the same spatial intensity distributions and relaxation rates as those utilized for Fig. 6.3. 96

Fig. 6.5: Velocity hole burning in the $M=1$ sublevel of NH_3 . Calculations are performed for a 9- μm intensity of 700 W/cm^2 pumping 200 mTorr of NH_3 at a frequency offset of 190 MHz from the $\text{sR}(5,0)$ line. The middle curve 5(b) gives the unperturbed population difference between levels (5,0) and (7,0) in the NH_3 98

ground state (n_2-n_1): Velocities on the x-axis are normalized to the most probable velocity divided by $(\ln 2)^{1/2}$. The upper curves 5(a) show the two-photon contribution to the 12- μm small-signal Raman gain at an offset of 185 MHz. This Raman susceptibility (χ_{12}) is plotted as a function of molecular velocity for both co- and counter-propagating beam. Curve 5(c) illustrates the population hole-burning which occurs when a 12- μm beam of intensity 50 W/cm^2 is applied at an offset of 185 MHz from the $\text{SP}(7,0)$ line. The dashed lines indicate full-width-half-maximum line-widths.

Fig. 7.1: Calculations of gain versus wavelength for different N_1/N_0 ratio. The gain is calculated for a 1% NH_3/N_2 mixture at 8 Torr. The calculations are carried out for the $K=0$ lines in the R-branch, $J=K=3$ in the Q-branch and $K=0$ in the P-branch. The pumped transition is marked with an asterisk (*). Note that the absorption on the pumped line goes to zero with $N_1/N_0=2$. 108

Fig. 7.2: Schematic diagram of the apparatus used to produce line-tunable cw operation in NH_3 between 10.7 and 13.3 μm in the selective cavity. Mirrors M_1 and M_2 transmit 90% of the 9- μm CO_2 radiation, and have $\sim 98\%$ reflectivity between 11.2 and 13.5 μm . 109

Fig. 7.3: Calculated gain as a function of wavelength for the P, Q, and R branches in NH_3 . The calculation assumed N_1/N_0 is 1.1, and was carried out for a 1% NH_3/N_2 mixture of 8 Torr. Only lines with $K=0$ (R-branch), $K=J=3,6,9$ (Q-branch), and $K=0,3,6$ (P-branch) are plotted. Also shown is the approximate loss line in the selective cavity, calculated assuming waveguide losses of 0.3 %/cm, and coupling losses of $\sim 10\%$ per pass between 11.2 and 13.5 μm . The increase in the loss at shorter wavelength is caused by a transmission increase in the output coupler combined with larger grating losses.

Fig. 7.4: Conventional tunable diode scans of gain and absorption in the $\text{sP}(7,K)$ multiplet of NH_3 . 5 W of resonant 9- μm radiation pump a 1% NH_3 in N_2 gas mixture of a total pressure of 5 Torr. The gas is contained in a 2.5-mm bore, 30-cm long waveguide cell. Note that gain only appears on the ortho-lines ($K=3n$).

LIST OF TABLES

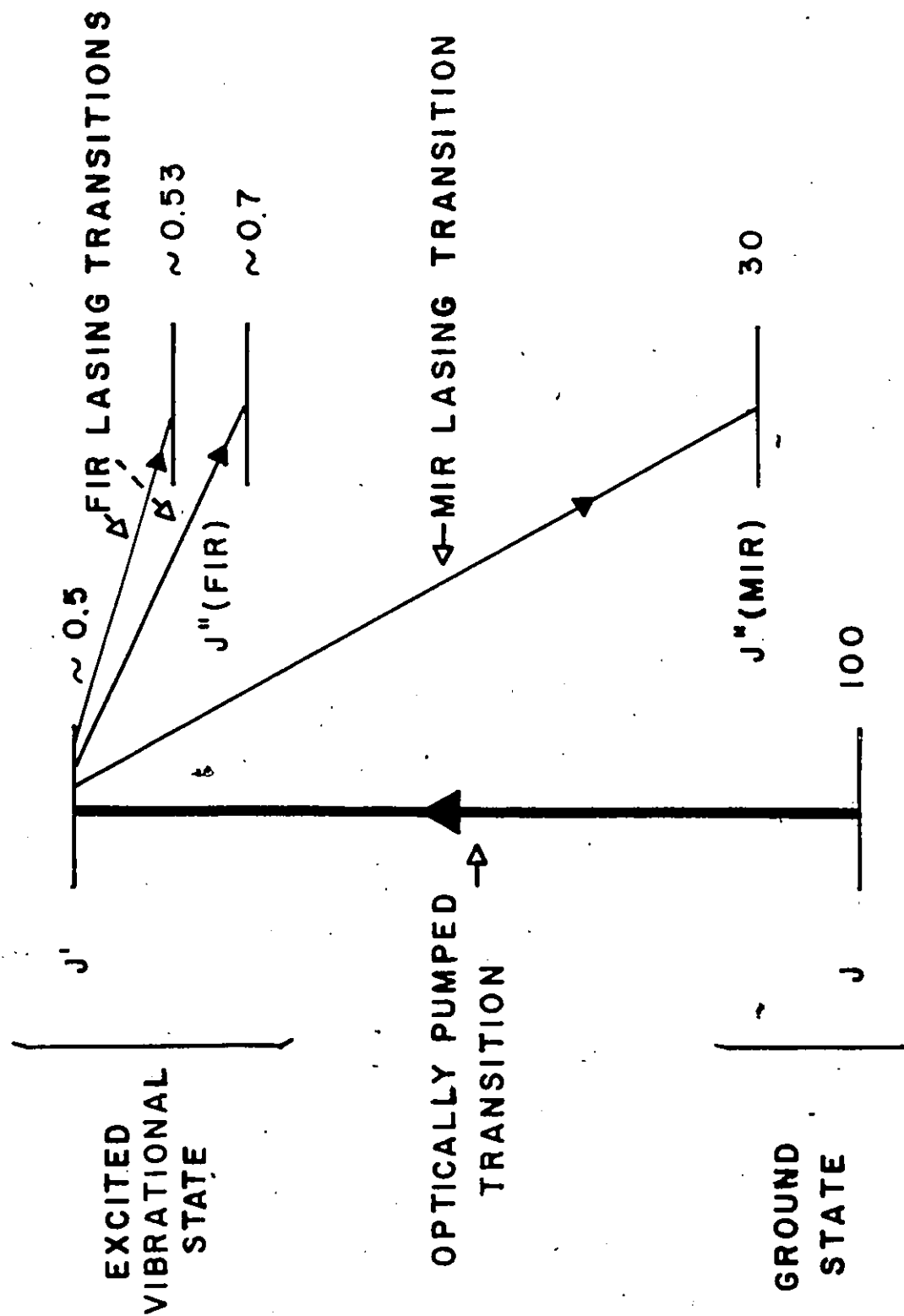
	Page
Table 2.1 NH_3 molecular data for the sR(5,0)/sP(7,0) coupled transitions used in the gain model.	23
Table 3.1 Variation of pump threshold power with pump offset frequency for the four NH_3 transitions investigated.	35
Table 4.1 Gain ratio versus pump offset.	67
Table 5.1 Performance of the 2.5-mm bore waveguide laser.	75
Table 7.1 Observed cw NH_3 laser lines.	111
Table 7.2 Other pump/ NH_3 combinations.	118

CHAPTER 1

INTRODUCTION

In 1970, Chang and Bridges reported the first optically-pumped far-infrared (FIR) laser [1]. This discovery came at a time when laser sources in the FIR region were very limited. The optical pumping technique uses powerful infrared lasers, such as carbon-dioxide, nitrous-oxide or hydrogen-fluoride, to excite vibrational modes in a molecular gas. The principal advantage of optical pumping over other excitation schemes (e.g. an electrical discharge), is that it enables the selective excitation of a particular molecular vibrational mode without appreciably disturbing the population of the other vibrational modes. Such an excitation mechanism is very energy specific and allows high operating efficiencies to be attained. Although optical pumping requires a pump frequency closely matched to the absorbing transition of the pumped molecule, the large number of FIR laser lines generated between 30 μm and 2 mm demonstrates the success of the technique for producing coherent millimeter and submillimeter radiation [2,3]. Figure 1.1 displays a molecular energy level diagram with typical level populations. Long wavelength emission occurs between two purely rotational levels within a specific vibrational level. In this case, a population inversion can easily be achieved since only a small fraction of the pumped level population needs to be transferred to the upper laser level. Thus, a large number of FIR lines has been observed. However, FIR lasers generally have low photon conversion efficiencies of a few percent or less [4,5].

Fig. 1.1: Typical energy level structure of an optically-pumped molecule. In one case, the ground state is pumped and FIR lasing occurs between two rotational levels ($J' \rightarrow J''$ (FIR)) within the same excited vibrational state. In the MIR case, the emission is a vibrational-rotational transition ($J' \rightarrow J''$ (MIR)). Also shown are typical thermal populations relative to the pumped level population of 100.



The search for powerful and efficient laser sources has concentrated in the past few years in the mid-infrared (MIR) region, i.e., between 10 μm and 30 μm . This interest in obtaining MIR lasers was motivated by the potential utilization of such sources in the fields of laser photochemistry, laser isotope separation and atmospheric monitoring [6-9]. MIR lasers are well suited for these applications since their emission frequencies are typical of vibrational transitions in gases. Optical pumping is a straightforward and simple technique to transfer the high efficiency and output power of a pump source such as the CO_2 laser to other molecules or lasers and to provide coherent output radiation across most of the mid-infrared region. The first optically-pumped MIR laser was reported by Chang and Wood in 1972 using a TEA HBr laser to pump CO_2 [10]. Soon thereafter, several other lasing transitions taking place between two vibrational levels were discovered using N_2O , OCS , SF_6 and NH_3 as the pumped molecules [11-14]. Because of the specific requirements imposed by several applications of MIR lasers, most researchers have directed their work toward the development of greater efficiency, higher output powers, and high repetition rate optically-pumped pulsed MIR lasers [15,16]. In favorable cases, peak output powers in excess of 1 MW and power conversion efficiencies up to 40% were attained [10,17]. The extension of this successful scheme from pulsed to continuous (cw) operation had never been attempted although powerful cw MIR sources would be extremely advantageous as a tool in fields such as spectroscopy and heterodyne detection. The main factor which contributed to the absence of efforts for producing an optically-pumped cw MIR laser is the high threshold pumping powers

reported for pulsed MIR lasers [18]. Since these threshold powers were several orders of magnitude larger than the power levels available with conventional cw sources, cw operation of optically-pumped MIR lasers did not appear practical. However, in this work, we will describe techniques which were used to overcome this apparent limitation. The work presented in this thesis is aimed at developing efficient, line-tunable optically-pumped cw lasers in the mid-infrared region. By using fairly simple pumping arrangements, cw lasing is reported for the first time on 20 different NH_3 transitions spanning the wavelength range between 10.7 and 13.3 μm . CW output powers as high as 10.5 W combined with quantum conversion efficiencies of up to 45% are achieved. These results are by far the best performances ever obtained for an optically-pumped cw laser in the infrared. The pumping schemes described in this work are general in their application and have opened the way to the generation of powerful new cw lasers in a region (10 μm to 30 μm) where such sources are rare.

Our initial experiments consisted of investigating several off-resonantly pumped 12- μm NH_3 transitions using low power CO_2 laser pulses. Ammonia was selected since when this work was initiated efficient pulsed operation had been reported in the MIR region using this molecule [19,20]. We succeeded in finding conditions under which the NH_3 threshold pumping power is decreased from the usual tens of kilowatts to power levels accessible with conventional cw CO_2 lasers. A key factor in the success of these experiments was the recognition that at low pumping powers the Raman process was the mechanism responsible for the 12- μm gain. A Raman transition occurs when a molecule in the

pumped level undergoes a coherent transition to the lower laser level by simultaneously absorbing a pump photon and emitting a second photon into the MIR or FIR field. The high thermal population present in the lower laser level (see figure 1.1 for typical level populations) combined with the large pump offset frequency (i.e. the difference between the line center of the absorbing transition and the pump frequency) used in our experiments makes the creation of a population inversion very difficult to achieve with the pumping power available from most cw sources. The Raman process can produce gain in the absence of a population inversion and consequently obviates the need for resonant pumping. Moreover, a Raman dominated laser is potentially very efficient since each photon absorbed from the pump is converted to the emission field. An important characteristic which differentiates Raman lasing from a single photon process is the laser frequency. A Raman transition lases at a frequency offset from the molecular transition by an amount equal to the pump offset frequency, thereby avoiding the strong line center absorption caused by the large population in the lower laser level. The Raman process was first proposed to explain the operation of an optically-pumped HF laser [21] and some experimental evidence for two-photon transitions was initially reported for off-resonantly pumped pulsed MIR lasers [22,23]. By measuring the lasing offset frequency of all the NH_3 transitions investigated, we clearly demonstrated the importance of the Raman process in the dynamics of low power pumped MIR lasers.

The low pumping thresholds obtained in the pulsed experiments indicated the feasibility of cw operation. The TE CO_2 pulsed laser

was replaced by a cw discharge tube, and cw lasing was obtained at 12.08 μm . This was the first optically-pumped cw laser to operate on a vibrational-rotational transition. The pumping scheme is very general and its extension to other NH_3 transitions is shown to be possible using pump offset frequencies as large as 1.4 GHz. Initially, ~ 1 W cw was produced at 12.08 μm in a nonoptimized ring laser cavity. A ring laser configuration was chosen for the MIR resonator to avoid the problems caused by the strong optical feedback from the linear MIR cavity to the pump source. In our later work, the 12- μm output is improved by an order of magnitude by redesigning the MIR cavity. A waveguide tube is now used to confine the pump radiation to a small diameter bore over a long interaction length, thus producing large amplification of the MIR radiation. The 12.08- μm NH_3 waveguide laser has the highest output power, energy efficiency and quantum conversion efficiency ever achieved in an optically-pumped cw infrared laser. Such a performance demonstrates that optical pumping is a very successful approach for generating new powerful cw sources in the mid-infrared.

Our objectives were not limited to producing efficient and line-tunable cw sources but were also aimed at understanding the fundamental processes governing the gain in such lasers. Such an understanding has been attained by measuring the 12- μm small-signal gain using a tunable diode laser (TDL) as a probe. The results were compared with a model based on a density matrix formalism. This comparison between experiment and theory represents one of the most detailed tests carried out on the interaction of a three-level system with two laser fields. A validation of the theory

is paramount if the model is to be used to predict gain on other NH_3 transitions or other molecules.

One of the difficulties encountered in extending the outstanding performance, achieved at $12.08\ \mu\text{m}$, to other NH_3 transitions lies in the limited number of good coincidences between available pump frequencies and absorbing transitions. Consequently, a novel approach was sought to develop a line-tunable cw source in the MIR region. Calculations based on our model showed that very efficient pumping should occur for exactly on-resonance pumping. By shifting the CO_2 pump frequency into resonance with an NH_3 absorption transition and adding a buffer gas, we were able to transfer a significant fraction of the NH_3 ground state population to the upper vibrational level $v_2=1$ (see Fig. 2.1 for a diagram of the NH_3 energy levels). The addition of a buffer gas ensured thermalization among the rotational distribution of each vibrational level, and cw lasing was observed on 20 NH_3 transitions by simply rotating the in-cavity $12\text{-}\mu\text{m}$ grating. This laser is the first line-tunable optically-pumped cw MIR laser. The technique is very attractive since by pumping on only one transition, lasing can be easily achieved on a multitude of lines. The simplicity of our pumping arrangement should prove to be extremely valuable in extending cw operation to other parts of the mid-infrared spectrum using other NH_3 isotopes and different molecules such as CH_3F , CF_4 or HF .

This thesis is divided into eight chapters and a brief outline of the individual chapters is given here. Theoretical considerations including a description of the ammonia molecule and the selection

rules governing infrared transitions are summarized in Chapter 2. Also a theoretical model of the gain in optically-pumped lasers is discussed, with a special emphasis on the differences between one-photon and Raman processes. Chapter 3 describes the results of a series of initial experiments performed with CO_2 laser pulses which lead to the development of the first optically-pumped cw MIR laser. Several characteristics of this new cw laser system are presented. In Chapter 4, we report on the investigation of the $12\text{-}\mu\text{m}$ small-signal gain over a wide range of experimental conditions. Rather than using a conventional oscillator-amplifier arrangement, we employed a tunable diode laser to probe various NH_3 amplifier cells. This probing technique is demonstrated to be very powerful for studying new lasers in the MIR region. The results of Chapter 4 helped in designing an improved $12\text{-}\mu\text{m}$ cavity. The new design described in Chapter 5 uses a waveguide tube for the $12\text{-}\mu\text{m}$ resonator. The performance of this new cavity is investigated and quantum efficiencies as large as 45% are measured. The high efficiency obtained at $12\text{-}\mu\text{m}$ is in part due to the Raman nature of the lasing process. In principle, a Raman dominated laser could have a quantum conversion efficiency of 100%. However for practical systems, the efficiency is strongly dependent upon the exact mechanism responsible for the gain saturation. To understand the $12\text{-}\mu\text{m}$ laser dynamics, the saturation process is examined in Chapter 6 using a conventional amplifier-oscillator arrangement. The measurements in Chapter 6 explain the lasing behavior observed in waveguide $12\text{-}\mu\text{m}$ systems and indicate several factors limiting the efficiency of the $12\text{-}\mu\text{m}$ Raman lasers. In Chapter 7, line-tunability between 10.7 and

13.3 μm is reported using a new pumping scheme. A simple model is presented to account for the output power distribution of the different lines. Several potential developments for this new laser system are also discussed. Finally, Chapter 8 contains a summary of the important results and conclusions of this thesis.

CHAPTER 2

THEORY

2.1 Introduction

This chapter gives a brief review of the NH_3 molecular structure, NH_3 energy levels, and the selection rules governing optical and collision induced transitions in the infrared region. A theoretical model based on a density matrix formalism is used to describe the gain in optically-pumped cw MIR lasers. Emphasis is given to the two-photon process which is demonstrated to be dominant in off-resonantly pumped cw MIR lasers. Finally, some model predictions are presented to underline the physical significance of the rather complicated gain expressions.

2.2 NH_3 Molecular Structure

Ammonia is a symmetric-top molecule with a pyramidal structure. The hydrogen atoms are situated at the corners of a regular triangle. The nitrogen atom lies above (or below) the hydrogen plane and forms the apex of the pyramid. The molecule has a strong permanent dipole moment which makes it a good candidate for optical pumping as the gain is directly proportional to the square of the dipole moment. The point group corresponding to the ammonia molecule is C_{3v} which implies the existence of four fundamental vibrational modes, two totally symmetric modes (A_1) ν_1 , ν_2 and two doubly degenerate modes (E) ν_3 , ν_4 [24].

2.3 Energy Diagram and Selection Rules

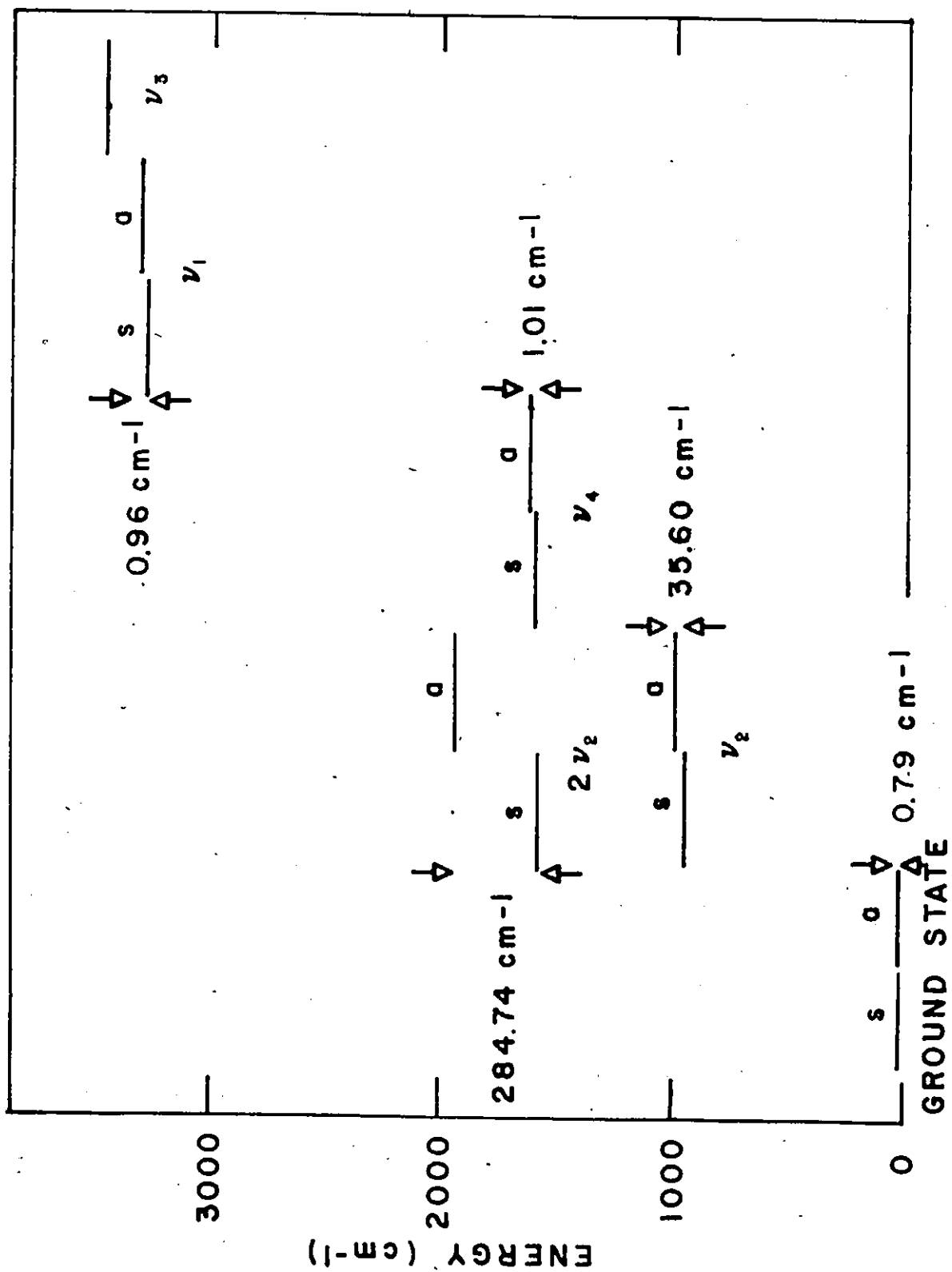
Over the years, the NH_3 molecule has been extensively studied by spectroscopists because of the intensity and richness of its spectrum. The multitude of transitions in the NH_3 spectrum is partly caused by the existence of both right and left handed forms [24]. These states are produced by the reflection of the nitrogen atom with respect to the hydrogen plane. The transformation of one form into the other occurs when the nitrogen atom is translated through the hydrogen plane (which acts as a potential barrier).

Each energy level of the pyramidal structure would be at least doubly degenerate if the potential barrier between the two forms was infinitely high. As predicted by quantum theory, a splitting appears in each vibrational-rotational level due to the tunnelling effect. In most pyramidal molecules the splitting is negligible or unresolved*. The energy separations between the inversion levels in ammonia are exceptionally large due to the small size of the potential barrier and the reduced mass [25]. For example in the $\nu_2=1$ vibrational level, the size of the splitting is $\Delta\nu=35.7 \text{ cm}^{-1}$. The energy splitting increases with the vibrational quantum number as illustrated for the ν_2 mode in Fig. 2.1. The levels are labelled symmetric (s) and antisymmetric (a). Figure 2.1 also shows the other fundamental modes, ν_1 , ν_3 , ν_4 and their respective inversion doubling [24,26].

Two rotational quantum numbers, J and K, characterize each NH_3 rotational level. J corresponds to the total angular momentum, and has

*For example in AsH_3 , the arsenic atom would take two years to tunnel through the hydrogen plane and thus AsH_3 has no observable splitting [25].

Fig. 2.1: Energy levels of the lower vibrational modes in NH_3 . The values of the corresponding inversion doubling are also given.



a $(2J+1)$ degeneracy associated with the various possible orientations of J in space ($M=J, J-1, \dots, -J$). $K=|k|$ where k represents the projection of J on the NH_3 molecular axis. The value k cannot be greater than J i.e. $k=0, \pm 1, \pm 2, \dots, \pm J$. Different selection rules are needed to describe the allowed transitions between a state (J,K) and (J',K') depending upon whether the transition is induced by an electric field or a collision. The selection rules for electric dipole transitions in the infrared spectrum are [24]

$$\begin{array}{lll} \Delta K = 0 & \Delta J = 0, \pm 1 & \text{if } K \neq 0 \\ \Delta K = 0 & \Delta J = \pm 1 & \text{if } K = 0 \\ a \longleftrightarrow s & a \nleftrightarrow a & s \nleftrightarrow s \end{array}$$

where \longleftrightarrow and \nleftrightarrow mean allowed and not allowed respectively. Each vibrational-rotational transition is written as: $xY(J,K)$ where x is either s or a , Y can be P, Q or R , corresponding to a change in J of $\Delta J=-1, 0, 1$ respectively. x, J and K always refer to the lower level of the transition. The special rule for $K=0$ arises from symmetry considerations involving the spin wave function which remove half of the levels. The a levels are missing when J is odd, while the s levels are missing if J is even [25]. Consequently, transitions with $\Delta J=0$ are not possible in levels with $K=0$. The selection rules for the Raman transitions differ from the infrared ones. In the Raman case we have [24]

$$\begin{array}{lll} \Delta K = 0 & \Delta J = 0, \pm 1, \pm 2 & \text{if } K \neq 0 \\ \Delta K = 0 & \Delta J = 0, \pm 2 & \text{if } K = 0 \\ a \nleftrightarrow s & a \longleftrightarrow a & s \longleftrightarrow s \end{array}$$

Two species of NH_3 exist ortho- NH_3 ($K=3n$, n an integer) and para- NH_3 ($K=3n\pm 1$) [24]. The strength of the infrared absorption depends

on the statistical weight associated with the nuclear spin function of the identical nuclei. Ortho- NH_3 has twice as many allowed states as para- NH_3 and hence twice the statistical weight [25]. The special case, $K=0$, has also twice the statistical weight of para- NH_3 .

The selection rules governing collision-induced transitions are in general not as rigorous as their optical counterparts. Nevertheless, the rules for collision-induced transitions greatly influence the rotational distribution inside a perturbed vibrational mode. Collision-induced transitions have been studied in detail by Oka [27,28] in both pure and buffered NH_3 . Conversion from the ortho- to para- NH_3 was found to be very slow as it requires the flip of a proton spin [27]. In addition to the absence of conversion between the ortho- and para- NH_3 , Oka gives the following dipole-type selection rules for collision-induced transitions in pure NH_3

$$\Delta K = 0 \qquad \Delta J = 0, \pm 1 \qquad s \longleftrightarrow a$$

The addition of a buffer gas such as He relaxes the selection rules to allow transitions between states with $\Delta k=3n$ (n an integer).

2.4 The Density Matrix Formalism

In recent years, considerable progress has been made in understanding the mechanisms involved in optically-pumped far-infrared (FIR) and mid-infrared (MIR) lasers. FIR lasers were initially analyzed by means of rate-equation models [29-31]. Such models describe the interaction of a molecule with two coherent fields in a stepwise fashion. The molecule is first excited to the upper laser level by a near resonant pump field and then contributes to the stimulated emission, provided a

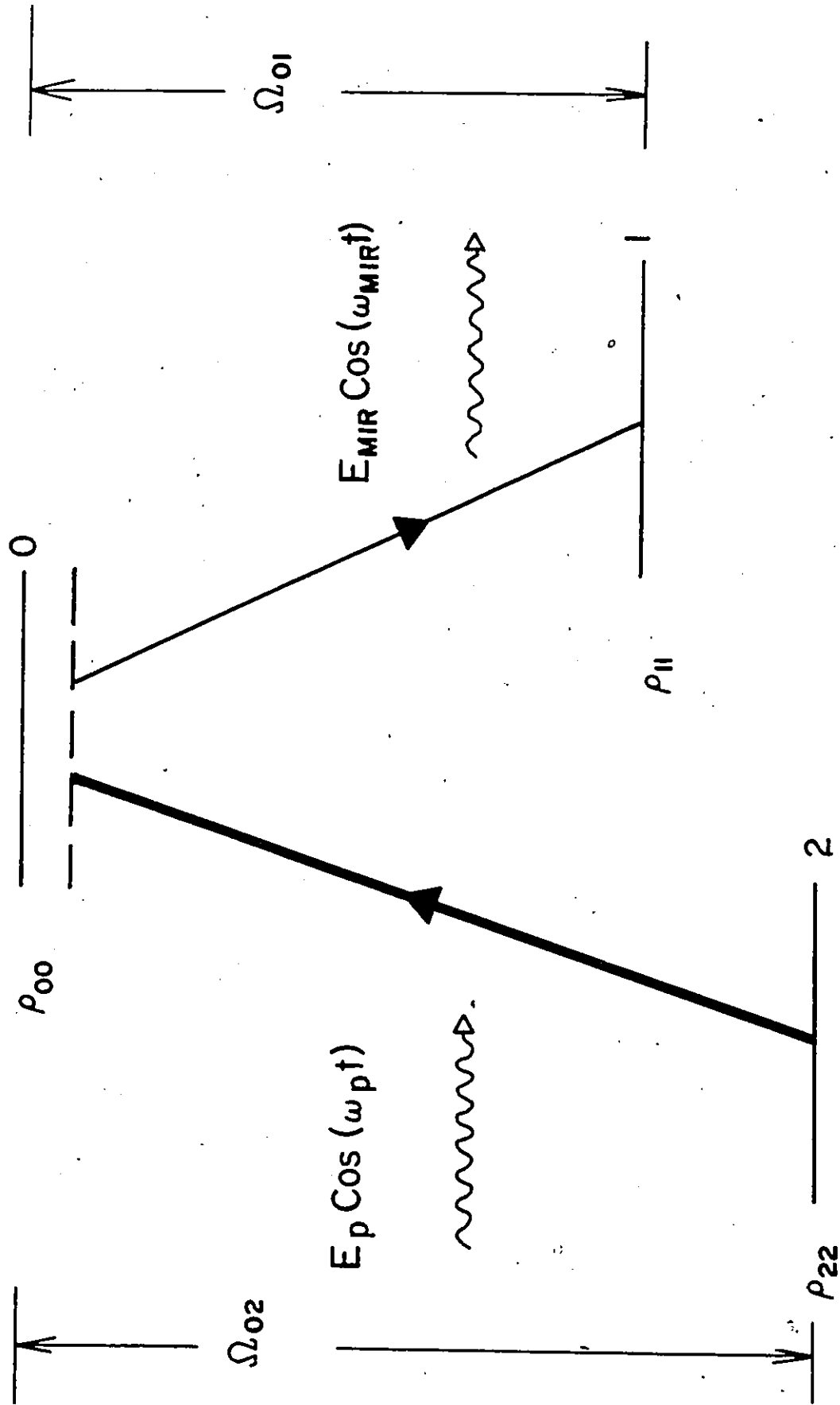
population inversion is achieved between the upper and lower laser levels. Emission will take place at the line center of the lasing transition. A simple rate-equation approach is inadequate to describe fully the interaction of a three-level system with two laser fields because it neglects important contributions to the gain due to multi-photon processes. A density matrix formalism has been used by several authors to describe the dynamics of a three-level system [32-37]. This quantum-mechanical approach emphasizes the importance of two-photon Raman processes in the interaction of two radiation fields with a three-level system, particularly important for off-resonantly-pumped transitions. With minor modifications, the models used to analyse optically-pumped FIR lasers can be utilized to examine the dynamics of cw MIR lasers. Such an approach is described below.

2.4.1 Theory of two laser fields interacting with a three-level system

An optically-pumped MIR laser can be represented as a three-level system interacting with two coherent fields. Figure 2.2 shows an energy level scheme representing such a system. We follow the nomenclature of Heppner *et al.* [37], in which levels 0, 1, and 2 are labeled in descending order of energy. The transition frequencies are Ω_{01} and Ω_{02} while ω_p and ω_{mir} represent the applied field frequencies. We have developed a computer code based on the equations of Heppner *et al.* The theory employs a density matrix formalism and its main features are summarized below. The time behavior of the density matrix is determined from Schrödinger's equation

$$\dot{\rho}_{mm} = -\gamma_{mm} (\rho_{mm} - \rho_{mm}^0) - i/\hbar [H, \rho]_{mm} \quad (2.1)$$

Fig. 2.2: Energy level scheme for an optically-pumped MIR laser. Ω_{02} and Ω_{01} are the pump and lasing transition frequencies respectively, ω_p and ω_{mir} represent the field frequencies and ρ_{00} , ρ_{11} , ρ_{22} correspond to the population in levels 0, 1 and 2, respectively.



$$\dot{\rho}_{mn} = -\gamma_{mn}\rho_{mn} - i/\hbar [H, \rho]_{mn} \quad (2.2)$$

where m, n vary from 0 to 2 and $[\]$ is the commutator bracket. ρ_{mm} and ρ_{mm}^0 give the probability for a molecule to be in the state m , in the presence and absence of a field respectively. The ρ_{mn} 's are off-diagonal terms related to the polarization induced by the applied fields. The decay rates γ_{mm} and γ_{mn} account for the molecular phase coherence times and are phenomenological terms. Only a quantum-mechanical treatment, where both the fields and molecules are quantized, fully accounts for the inclusion of these decay times. The γ_{mm} 's are called longitudinal relaxation rates and represent the rate at which the population in the m 'th level is restored to its thermal equilibrium value. The γ_{mn} parameters are the transverse relaxation rates and characterize the loss of molecular coherence [38]. Specifically, collisions between atoms can disrupt the phase of the radiating atomic dipole without a change of state, the final effect being an increase in the decay rate of the induced polarization.

The interaction under the applied external fields is solved in the rest frame of the molecule where the matrix element mn of the total Hamiltonian is given by

$$H_{mn} = \hbar W_m \delta_{mn} + V_{mn} \quad (2.3)$$

$\hbar W_m$ is the eigenvalue of the unperturbed Hamiltonian of the molecule (no external field present) and corresponds to the energy of a molecule in level m . V_{mn} is the interaction energy. The perturbation considered here is the dipole interaction

$$\dot{\rho}_{mn} = -\mu_{mn} \cdot E(\underline{r}, t) \quad (2.4)$$

where μ_{mn} is the electric dipole matrix element between level m and n . $E(\underline{r}, t)$ is the total field in the reference frame of the molecule and is divided into two plane travelling waves (for convenience we choose the z direction as the propagation axis)

$$E(z, t) = E_p \cos((\omega_p - k_p v)t - k_p z + \phi_1) + E_{mir} \cos((\omega_{mir} - \epsilon k_{mir} v)t - \epsilon k_{mir} z + \phi_2) \quad (2.5)$$

ϵ specifies the relative direction between the pump and MIR fields, and is positive ($\epsilon=+1$) for copropagating beams and negative ($\epsilon=-1$) for the counterpropagating case. $k_p v$ and $k_{mir} v$ are the Doppler shifts of the applied fields seen in the moving frame of a molecule with axial velocity v .

A general solution of equations (2.1) and (2.2) has not yet been obtained. However, these equations can be solved if certain approximations pertinent to our MIR system are made. Since most of our experiments used cw pumping sources, the density matrix equations are solved for the steady state by setting the population changes $\dot{\rho}_{mm}$ equal to zero. For the off-diagonal elements $\dot{\rho}_{mn}$, the standard rotating wave approximation (RWA) is used [38]. Hence only the terms in which the molecular polarization and the electric field wave rotate together, are retained. This approximation is justified because we are interested only in the resonant behavior of the induced polarization. Furthermore, the amplitudes ρ_{mn} are assumed to vary slowly in an optical period ($T \sim 10^{-13}$ sec).

The use of polarized light removes the M-degeneracy of the

molecular levels. This effect originates from the M dependence of the transition matrix elements ($\mu_{mn}(M)$). Most of our work was carried out with parallel linear polarization of the pump and the MIR fields. The M -selection rule is in this case $\Delta M=0$ and thus we can treat the M systems separately assuming slow (compared to the decay rates $\sim 150 \text{ sec}^{-1} \text{ Torr}^{-1}$) M -relaxation [39]. The total gain is calculated by summing the susceptibility of each individual M component. (The influence of other polarization combinations on the MIR gain will be discussed in Chapter 4.)

Under these approximations, the MIR gain for molecules moving with axial velocity v can be written as

$$\alpha_{\text{mir}}(M,v) = k_{\text{mir}} \text{Im}(S_1(M,v)r_{10}(M,v) + S_2(M,v)r_{21}(M,v)) \quad (2.6)$$

where S_1 and S_2 are related to lineshape functions and contain the resonance for maximum gain, power broadening effects, and ac Stark shifts due to both the pump and MIR intensities. The explicit expressions for S_1 and S_2 are given in Appendix A. The population difference between level m and n is denoted by r_{mn} . A careful examination of the two terms on the right hand side of equation (2.6) helps in gaining a better understanding of the MIR laser dynamics. The first term is proportional to r_{10} and represents the single-photon contribution to the gain. This term is responsible for absorption at the MIR frequency in the absence of population inversion between the upper and lower laser level ($\rho_{11} > \rho_{00}$). The second term deals with the two-photon Raman process where a molecule is transferred from level 2 to level 1 by simultaneously

absorbing a photon from the pump field and emitting one into the MIR field. Note that the Raman process is proportional to the population difference ($\rho_{22} - \rho_{11}$) and allows gain to be created even in the absence of a population inversion between levels 0 and 1.

The total gain expression is obtained by integrating expression (2.6) over all the velocity classes using a Doppler velocity profile and subsequently summing over all M-values.

$$\alpha_{\text{mir}} = \sum_{M=-J_0}^{J_0} \int \alpha_{\text{mir}}(M, v) f(v) dv \quad (2.7)$$

where

$$f(v) = \frac{1}{u\sqrt{\pi}} \exp - (v/u)^2$$

and u is the most probable velocity $\sqrt{2k_B T/M}$ (M is the mass of the NH_3 molecule, k_B the Boltzmann's constant and T the ambient gas temperature). The present model is valid in principle for arbitrary field strengths and mixed broadening transitions, i.e., in pressure regions where both the inhomogeneous and homogeneous linewidths must be considered. However the accuracy of the computer predictions based on equation (2.7) will be limited to some extent by the reliability of the various molecular constants used as input data. The next section discusses the input data for the particular set of NH_3 transitions used throughout most of this study.

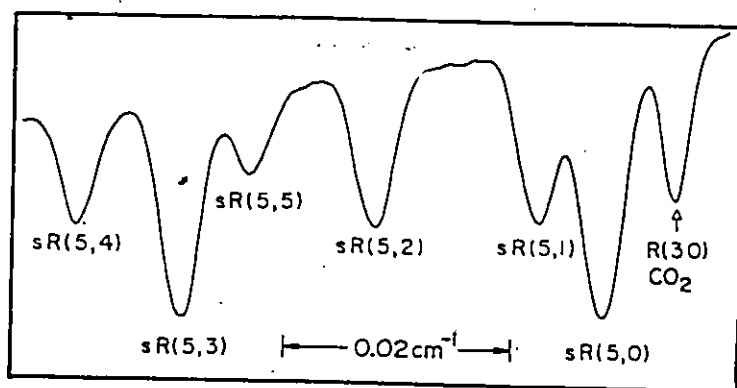
2.4.2 Laser transition and input data

A major portion of this thesis deals with the coupled transitions $\text{SR}(5,0)/\text{SP}(7,0)$ in NH_3 and thus this section will concentrate on the

molecular data relative to these lines. Figure 2.3 shows the vibrational-rotational energy levels of NH_3 relevant to $12.08 \mu\text{m}$ lasing. The $\text{sR}(5,0)$ transition is pumped by the $\text{R}(30)$ CO_2 laser line at $9.22 \mu\text{m}$, and lasing occurs on the coupled $\text{sP}(7,0)$ transition at $12.08 \mu\text{m}$. The insert of Fig. 2.3 is a high resolution absorption spectrum of NH_3/CO_2 taken with a tunable diode laser near $9.22 \mu\text{m}$. Note that the CO_2 pump line is offset from the nearby $\text{sR}(5,0)$ line by $190 \pm 7 \text{ MHz}$ [40]. This pump offset plays a crucial role in the operation of the cw $12\text{-}\mu\text{m}$ laser, as will be shown in the next section.

Table 2.1 summarizes the input data used in the computer code for this three-level system. Spectroscopic constants for NH_3 were taken from Refs. [41-46], and by combining these with the partition function given by Townes and Schawlow [25], we calculated the initial fractional population in each level at room temperature*. The vibrational matrix element for the ν_2 band of NH_3 is taken as 0.24 ± 0.01 Debye [46,47]. The combined uncertainty of the pump offset and matrix element gives $\sim \pm 20\%$ variation in the Raman gain calculations. A potentially more serious problem is the uncertainty in the level relaxation rates γ_m and the cross-relaxation rates or collisional broadening coefficients γ_{mn} . We have used a tunable diode laser operating near $12 \mu\text{m}$ to measure the NH_3 self-broadening coefficient $\Delta\nu_{01}$ ($=\gamma_{01}/\pi$) as $19.4 \pm 1 \text{ MHz/Torr}$ full width at half maximum (FWHM), while Taylor's calculated value was taken for the $\Delta\nu_{02}$ pressure

*These populations were adjusted appropriately when gain calculations were carried out at elevated or reduced temperatures.



PUMP OFFSET

$\Delta\nu_p = 190 \text{ MHz}$

$a(6,0)$

$v_2 \text{ MODE}$
 $V=1$

$R(30) \text{ CO}_2 \text{ PUMP}$

$9.22 \mu\text{m}$

$sR(5,0)$

OUTPUT $sP(7,0)$

$12.08 \mu\text{m}$

$s(7,0)$

$s(5,0)$

GROUND
STATE
 $V=0$

Fig. 2.3: Vibrational-rotational energy levels of NH_3 relevant to 12.08- μm lasing. The insert is a high-resolution NH_3/CO_2 absorption spectrum taken near 1084.6 cm^{-1} . The CO_2 absorption is indicated by the arrow. The other absorption peaks belong to the $\text{sr}(5,K)$ manifold of NH_3 . The offset between the $\text{R}(30)$ and $\text{sr}(5,0)$ line center is $\Delta\nu_p = 190 \pm 7 \text{ MHz}$.

Table 2.]

NH₃ molecular data for the sR(5,0)/sP(7,0) coupled transitions used in the gain model.

Transition	Frequency (cm ⁻¹)
sR(5,0)	1084.627
sP(7,0)	827.877

Pump frequency offset 190 ± 7 MHz

Vibrational dipole moment 0.24 ± 0.01 D

Fractional Population	Decay Rate (sec ⁻¹ Torr ⁻¹)
$n_0 = 1.16 \times 10^{-4}$	$\gamma_0 = 23.4 \times 10^6$
$n_1 = 7.16 \times 10^{-3}$	$\gamma_1 = 93.6 \times 10^6$
$n_2 = 1.82 \times 10^{-2}$	$\gamma_2 = 93.6 \times 10^6$

Pressure Broadening Rate
(sec⁻¹ Torr⁻¹)

$$\gamma_{01} = 60.9 \times 10^6$$

$$\gamma_{02} = 55.9 \times 10^6$$

$$\gamma_{12} = 93.6 \times 10^6$$

broadening [41]. To evaluate the individual relaxation rates γ_m and the cross-relaxation rate γ_{12} , we have assumed every collision to be an energy changing collision (hard-sphere collisions), i.e., $\gamma_{mn} = (\gamma_m + \gamma_n)/2$ and set $\gamma_1 = \gamma_2 = 4\gamma_0$. This factor of 4 is based on rates published for the aQ(8,7) transition [39] and is in qualitative agreement with other studies which show that $\gamma(\text{ground state}) > \gamma(\text{excited state})$ in the ν_2 mode of NH_3 [48]. The influence of variations in these relaxation rates on the small-signal Raman gain was examined by considering the extreme values of γ_{mn} and varying the ratio of $\gamma(\text{ground state})$ to $\gamma(\text{excited state})$ from 10:1 to 1:1. Under typical experimental conditions, we found a $\pm 10\%$ variation of the calculated gain. Although the uncertainties in the relaxation rates γ_m are large, they have a small impact on the calculated small-signal gain since very little population transfer occurs at low 12- μm intensities. At large 12- μm fields, the values of the rates γ_1 , γ_2 , γ_{12} are important in assessing the mechanism responsible for gain saturation and this situation will be addressed in detail in Chapter 6.

By combining the uncertainties in all the input data, we estimate that the calculated small-signal gain coefficients should be accurate to $\pm 30\%$, provided the gas temperature is accurately known. However, in any practical experiment, absorption of the pump radiation heats the NH_3 and leads to further uncertainties in comparing theory and experiment as shown in Section 4.3.

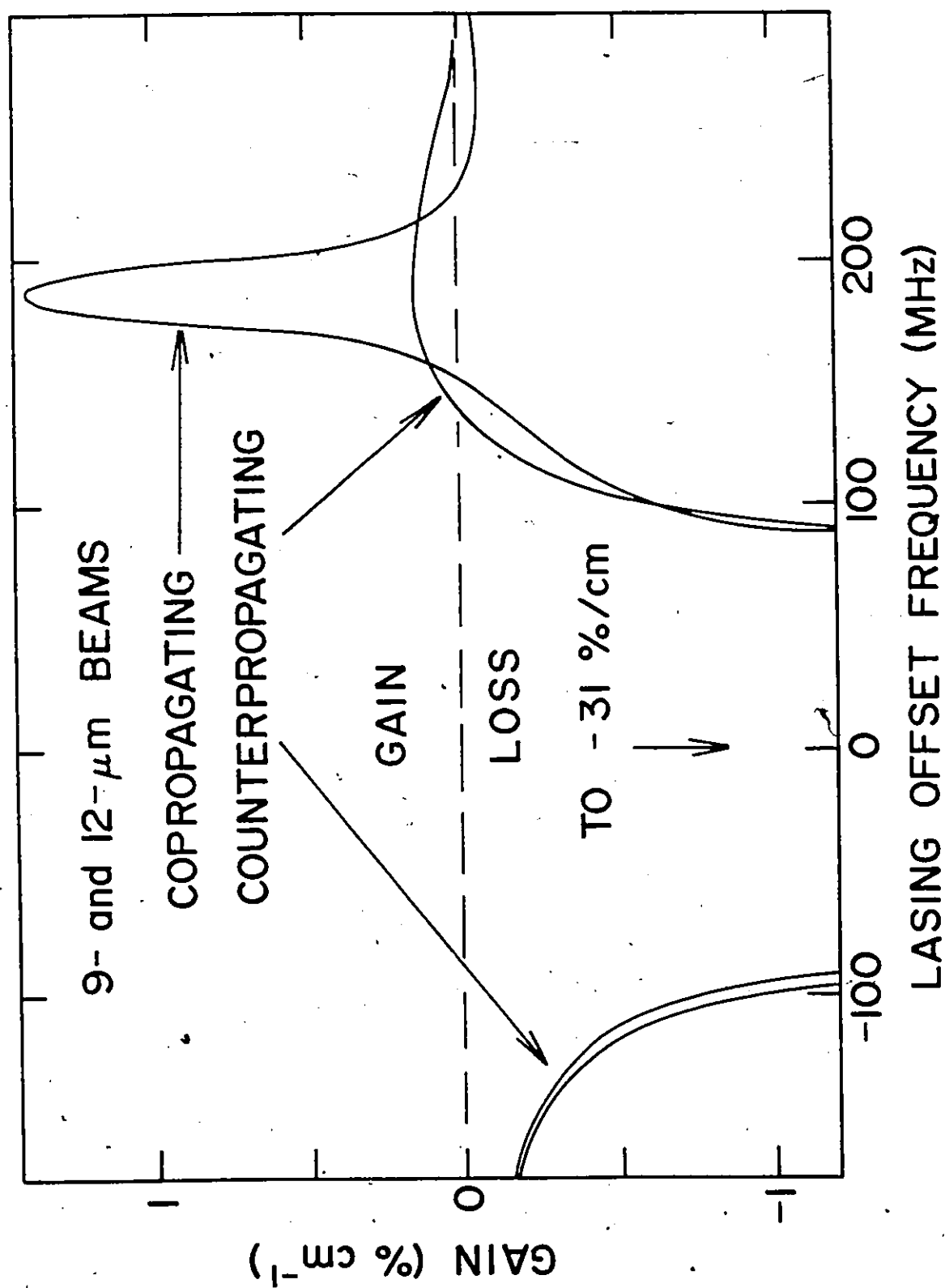
2.4.3 Model Predictions

The purpose of this section is to stress the important characteristics of the 12- μm small-signal gain based on our model. (A

detailed comparison between theory and experiment using a tunable diode laser as a 12- μm probe, will be given in Chapter 4). Figure 2.4 shows plots of the small-signal gain (for the co- and counter-propagating cases) versus the MIR detuning frequency ($\omega_0 - \omega_{\text{mir}}$), using the input data of Table 2.1, and a pumping intensity and pressure typical of our experimental conditions. Gain only appears near the Raman resonance condition, i.e., at a frequency shifted from the $\text{SP}(7,0)$ line center by an amount equal to the pump offset frequency (~ 190 MHz). Since population transfer to the upper level $\text{a}(6,0)$ is small, the single-photon contribution consists of a strong absorption at the $\text{SP}(7,0)$ line center. The Lorentzian wings of this absorption slightly reduce the peak Raman gain, but provided this absorption is taken into account, the model predicts that the Raman gain is linearly proportional to pump intensity. This linear dependence remains until pumping intensities are sufficiently intense to cause ac Stark shifts and splitting of the various M-components [49]. At the pump intensities used in this study ($\leq 1 \text{ kW/cm}^2$) these effects are negligible.

The difference between the co- and counterpropagating 9- and 12- μm beams is clearly displayed in Fig. 2.4. The calculated gain in both cases employed the same input parameters, except for reverse directions of the 12- μm radiation. Note the large difference in the gain linewidth between the two cases. For copropagating beams, a molecule with an axial velocity v experiences pump and MIR fields Doppler shifted by respectively $-k_p v$ and $k_{\text{mir}} v$ while in the counterpropagating case the Doppler shifts are $-k_p v$ and $-k_{\text{mir}} v$. Thus at low pressure, the limiting Raman linewidth is approximately given by the difference between

Fig. 2.4: Small-signal gain profile for co- and counter-propagating 9- and 12- μm beams calculated using the computer code. The small-signal gain is plotted as a function of the lasing offset frequency ($\omega_{01} - \omega_{\text{mir}}$). The pump intensity is 500 W/cm^2 at an ammonia pressure of 500 mTorr. The pump offset is equal to 190 MHz. Note the large reduction in the peak value and the wider gain linewidth obtained in the counterpropagating case.



the 9- and 12- μm Doppler linewidths (~ 23 MHz FWHM) for the copropagating beams and the sum of the 9- and 12- μm Doppler linewidths in the counter-propagating case (~ 176 MHz FWHM). One consequence of the increased linewidth is a reduction in the magnitude of the gain as illustrated in Fig. 2.4. In both cases, the Raman gain increases linearly with NH_3 pressure until pressure broadening becomes significant, and as a result the Raman gain begins to level off. The pressure region at which this nonlinear behavior occurs depends on the value of the Doppler-limited Raman linewidth*.

One of the main characteristics of Raman processes is the strong influence of the pump offset frequency on both the magnitude and frequency of the Raman gain. The model predicts that the line center of the Raman gain tunes with the pump offset (Raman resonance condition) and that the magnitude of the gain is inversely proportional to the square of the pump offset. We have confirmed these predictions and the results are presented in Chapter 4.

2.5 Summary

This chapter contains the description of the ammonia molecule and of the theoretical model used throughout most of this work. Two different terms contribute to the small-signal gain: the single-photon and two-photon Raman processes. In cw off-resonantly pumped systems, the single-photon contribution is generally a line center absorption, while the Raman process constitutes the dominant mechanism responsible for the gain. The properties of the Raman gain described here will

*The nonlinear dependence of the Raman gain with pressure becomes noticeable at a pressure of ~ 0.3 Torr for the copropagating case and ~ 2 Torr in the counterpropagating case.

serve in the next chapter to explain the gain dynamics present in optically-pumped MIR lasers:

CHAPTER 3

PRELIMINARY EXPERIMENTS

3.1 Introduction

In this chapter, initial experiments performed with NH_3 using low-power CO_2 laser pulses are described. The objective of these pulsed experiments is twofold; on the one hand to examine the possibility of reducing threshold pumping powers to values accessible to cw CO_2 lasers and on the other hand to study the applicability of the model described in Chapter 2 for off-resonantly-pumped MIR systems. Several NH_3 transitions with a range of pump offset frequencies are investigated. The low threshold pumping powers measured in our linear MIR cavity indicated the feasibility of cw operation at $12\text{ }\mu\text{m}$. In addition, the experiments demonstrate the importance of two-photon Raman processes at low pumping powers. A ring laser resonator is used to produce the first optically-pumped cw laser in the mid-infrared. Our pumping scheme is general and could be extended to other NH_3 transitions. Preliminary experiments demonstrating some of the important characteristics of this new laser system are presented.

3.2 $12\text{-}\mu\text{m}$ Raman Lasers Pumped by Low-Power CO_2 Laser Pulses

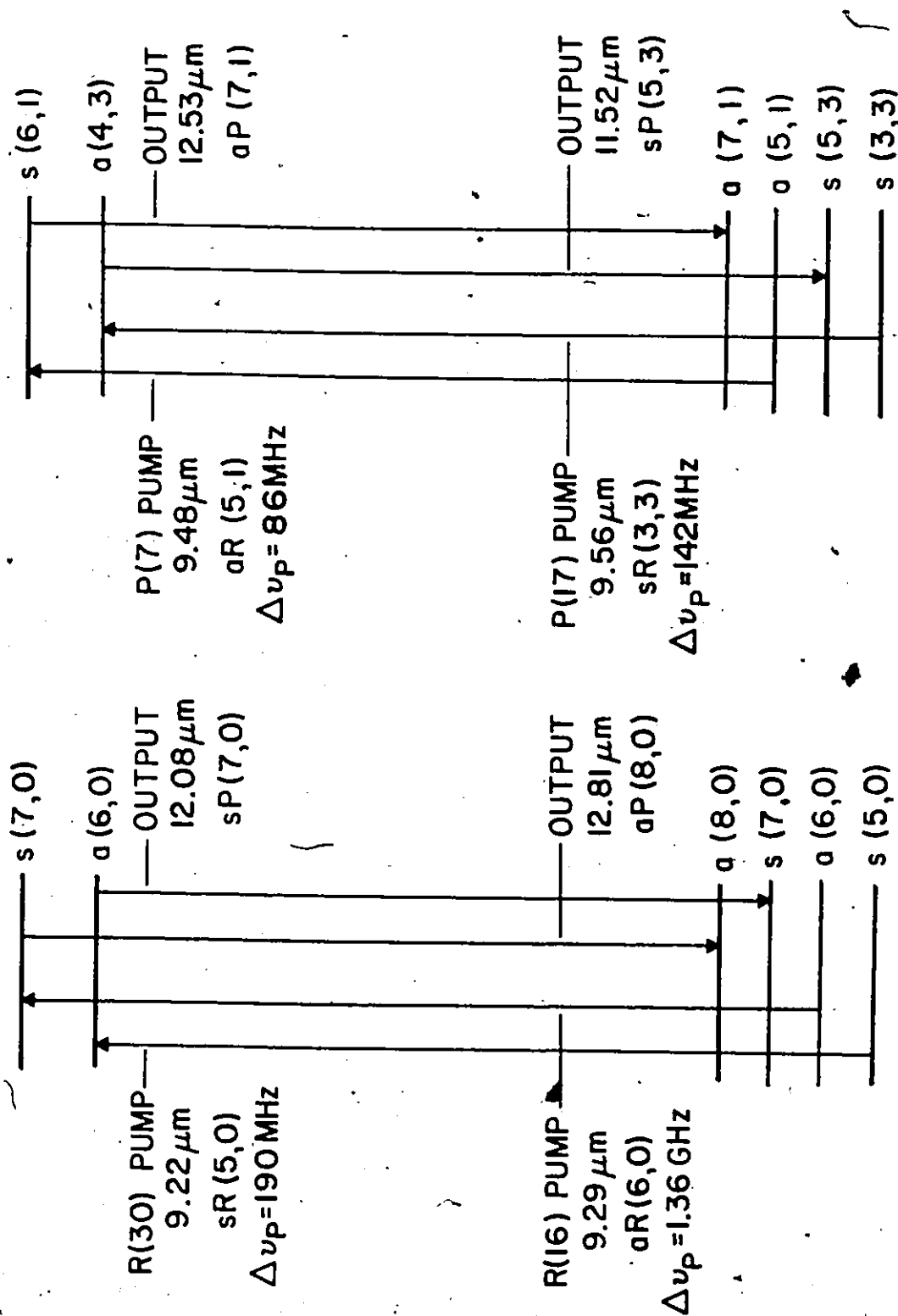
In recent years, optical pumping of molecular gases by CO_2 lasers has generated over 1000 lasing transitions in the mid- to far-infrared regions. However, cw operation of such lasers had been confined to wavelengths longer than $34\text{ }\mu\text{m}$ [2,3]. One of the major difficulties encountered in the development of optically-pumped cw MIR lasers relates

to the small energy difference between the pumped level and lower laser level which results in a high thermal population in the lower laser level. Consequently, a population inversion is in general difficult to achieve due to the low pumping power available from conventional cw laser sources. As a starting point, our initial experiments used pulses from a TE CO_2 laser to pump NH_3 and produce lasing in the $12\text{-}\mu\text{m}$ region. The experimental arrangement was designed to minimize optical pumping powers and thus examine the feasibility of cw MIR operation. In addition to reducing the threshold pumping powers, our arrangement facilitates the study of the gain dynamics present in $12\text{-}\mu\text{m}$ NH_3 laser systems. Different authors have suggested that the gain mechanism in $12\text{-}\mu\text{m}$ pulsed NH_3 lasers may be attributed to a Raman process [22,23]. However, little experimental evidence has been reported to support this interpretation. This lack of experimental evidence is associated with the fact that the intense electric fields generated with high-power pulsed lasers create such large ac Stark shifts and power broadenings that one-photon transitions and Raman processes become inextricably mixed. The low pumping powers used in our experiments greatly simplify the dynamics of the MIR laser by reducing the effects of ac Stark shifts and power broadening and have enabled us to identify the main mechanism responsible for the $12\text{-}\mu\text{m}$ gain.

Four different $9\text{-}\mu\text{m}$ CO_2 laser transitions were used to pump low-pressure NH_3 , and lasing on the coupled $12\text{-}\mu\text{m}$ transitions was investigated. Figure 3.1 shows the relevant energy levels in NH_3 . The two emission lines at $12.08\text{ }\mu\text{m}$ and $12.81\text{ }\mu\text{m}$ are pumped by regular CO_2 laser transitions and have been investigated by many authors [14,22,50-52].

Fig. 3.1: Relevant energy levels of the four NH_3 transitions investigated. $\Delta\nu_p$ represents the pump offset frequency.

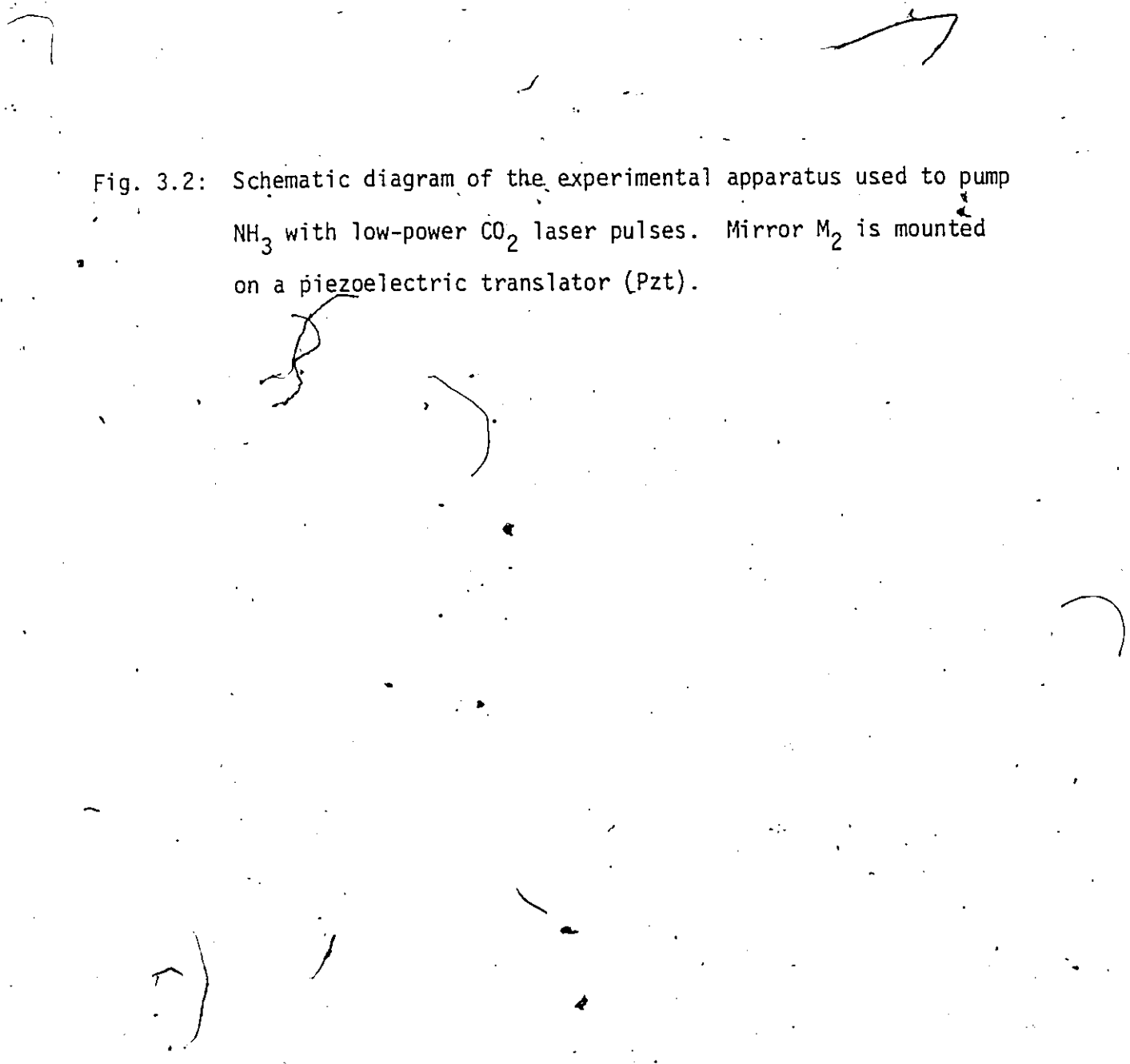
ν_2 MODE
 $V=1$



The emission lines at 11.52 μm and 12.53 μm are pumped by sequence CO_2 laser lines and were recently reported by Znotins *et al.* [53]. The crucial parameter which differentiates these four transitions is the frequency separation between the pump laser line and the center of the 9- μm NH_3 absorption line, i.e., the pump offset frequency $\Delta\nu_p$. The offset is given in Fig. 3.1, and ranges from 1.36 ± 0.01 GHz for the R(16)-aR(6,0) combination [54], to only 86 ± 3 MHz for the P(7)-aR(5,1) combination [53].

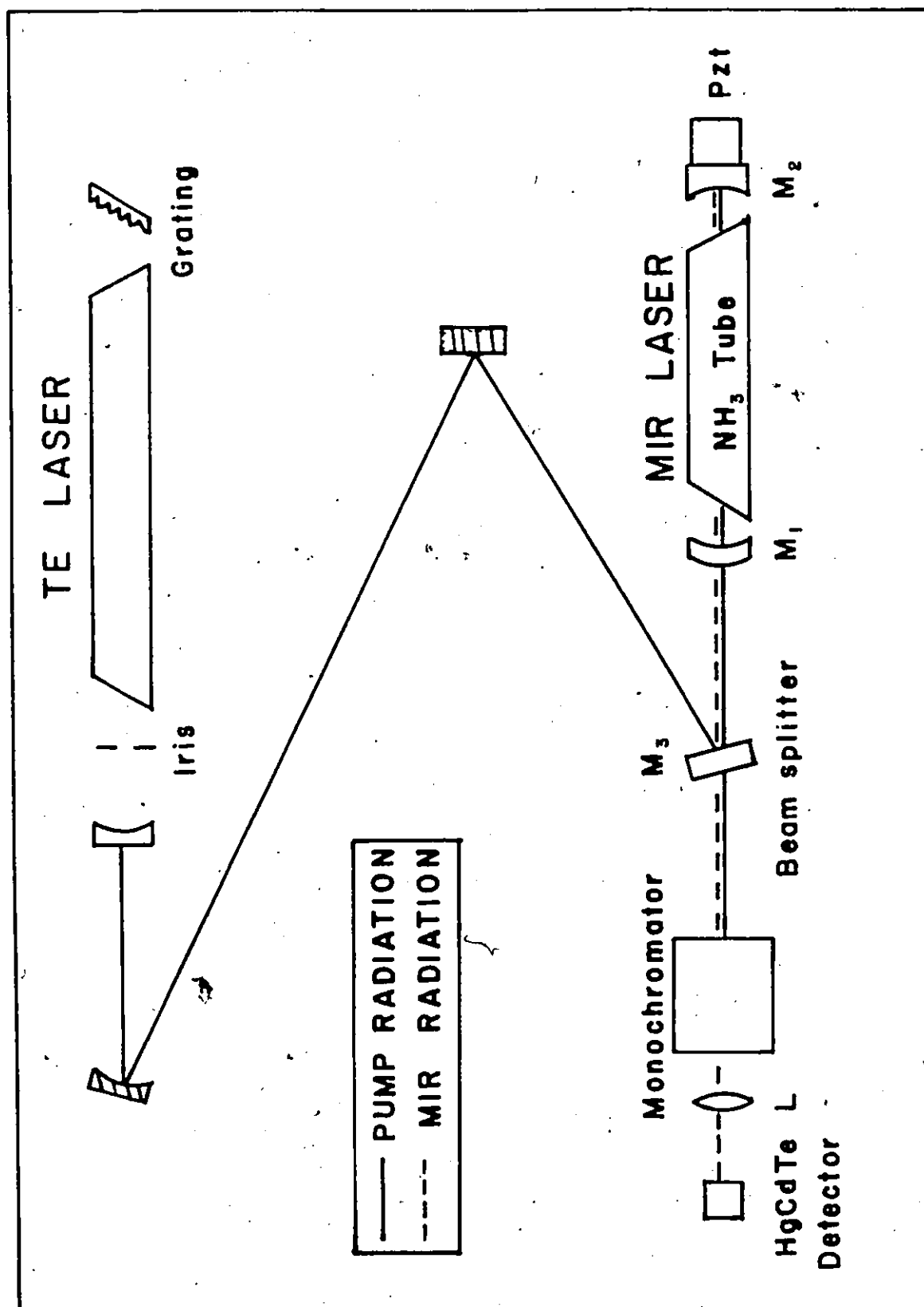
3.2.1 Experimental apparatus and results

Figure 3.2 is a schematic diagram of the apparatus. The optically-pumped NH_3 cell is in a short brass tube (~ 38 cm long) fitted with NaCl Brewster windows. Such a short cell enables us to focus the pump radiation tightly into the MIR cavity, while maintaining a reasonably constant CO_2 beam diameter along the entire tube length. A helical pin-pin TE laser is utilized as the pumping source and is generally operated at low pressure (~ 50 Torr) to ensure that lasing takes place at line center. An in-cavity hot CO_2 cell is inserted when CO_2 sequence transitions are required [55]. Typical output pulses from our CO_2 laser have peak powers of ~ 1 kW and pulse widths ~ 1 μs (FWHM). These pulses are usually strongly attenuated before entering the MIR cavity. All optics are designed to minimize the pump power requirements. A concave ($R=1.4$ m) gold coated mirror focuses the CO_2 laser beam into the short MIR cavity through a ZnSe dichroic mirror M_1 (9- μm transmission $\sim 60\%$). The pump beam slightly overfills the 12- μm TEM_{00} mode. The MIR resonator is formed by M_1 ($R=1.6$ m with a reflectivity of 95% at 12 μm) and a



The diagram is a hand-drawn schematic of an experimental setup. It features a horizontal line representing a central axis. On the left side, there is a vertical line segment. On the right side, there is a curved line segment. In the center, there is a small circle. The text 'Fig. 3.2: Schematic diagram of the experimental apparatus used to pump NH₃ with low-power CO₂ laser pulses. Mirror M₂ is mounted on a piezoelectric translator (Pzt).' is written below the diagram.

Fig. 3.2: Schematic diagram of the experimental apparatus used to pump NH_3 with low-power CO_2 laser pulses. Mirror M_2 is mounted on a piezoelectric translator (Pzt).



gold coated mirror mounted on a piezoelectric translator. The 12- μm laser pulses are coupled out through M_1 and a beam splitter (M_3 with a transmission of 15% of 12 μm), directed into a monochromator, and detected with a liquid-nitrogen-cooled HgCdTe detector. The linearity of the detector was verified using calibrated attenuators.

This apparatus was designed to examine the threshold behavior of the four laser systems shown in Fig. 3.1. For each CO_2 pump transition, NH_3 pressures and MIR cavity alignment were optimized as the pump beam was progressively attenuated until 12- μm lasing ceased. Table 3.1 summarizes the pump power required for threshold operation. These threshold powers are one-to-two orders of magnitude lower than previously published thresholds [18] and most of the values are well within the reach of conventional cw CO_2 lasers. Of fundamental importance is the very strong variation of threshold power with $\Delta\nu_p$, confirming the importance of the pump offset frequency in the MIR laser dynamics. As discussed in Chapter 2, a Raman-dominated cw laser will emit with a frequency offset equal to the pump offset value, whereas if a population inversion is created between the upper and lower laser levels the emission will occur at the line center of the lasing transition. These simple considerations led us to investigate the exact frequency of the 12- μm laser output, as this would clearly distinguish between Raman and single-photon processes.

An accurate method of differentiating between 12- μm lasing at line center, as opposed to lasing with a frequency offset $\Delta\nu_{\text{mir}}$, is to measure the absorption coefficient of the laser output in an

Table 3.1

Variation of pump threshold power with pump-offset frequency for the four NH_3 transitions investigated.

NH_3 Lasing Transition (μm)	CO_2 Pump Line 9- μm Band	Pump Offset (MHz)	Threshold (W)
aP(7,1) - 12.53	P(7) ^{a)}	86	5
sP(5,3) - 11.52	P(17) ^{a)}	142	18
sP(7,0) - 12.08	R(30)	190	20
aP(8,0) - 12.81	R(16)	1355	660

a) sequence transition

external NH_3 cell. This absorption is dramatically different for the two cases [56]. We used a 10-cm external cell and measured the absorption of the 12- μm laser pulses as a function of NH_3 pressure. The 12- μm pulses were attenuated to ensure small-signal absorption. Figure 3.3 shows the results of such an experiment for the 12.81- μm output. To estimate the offset frequency $\Delta\nu_{\text{mir}}$, we used Taylor's data for the 12- μm line strength and linewidth [41] and a Lorentzian absorption profile of the following form

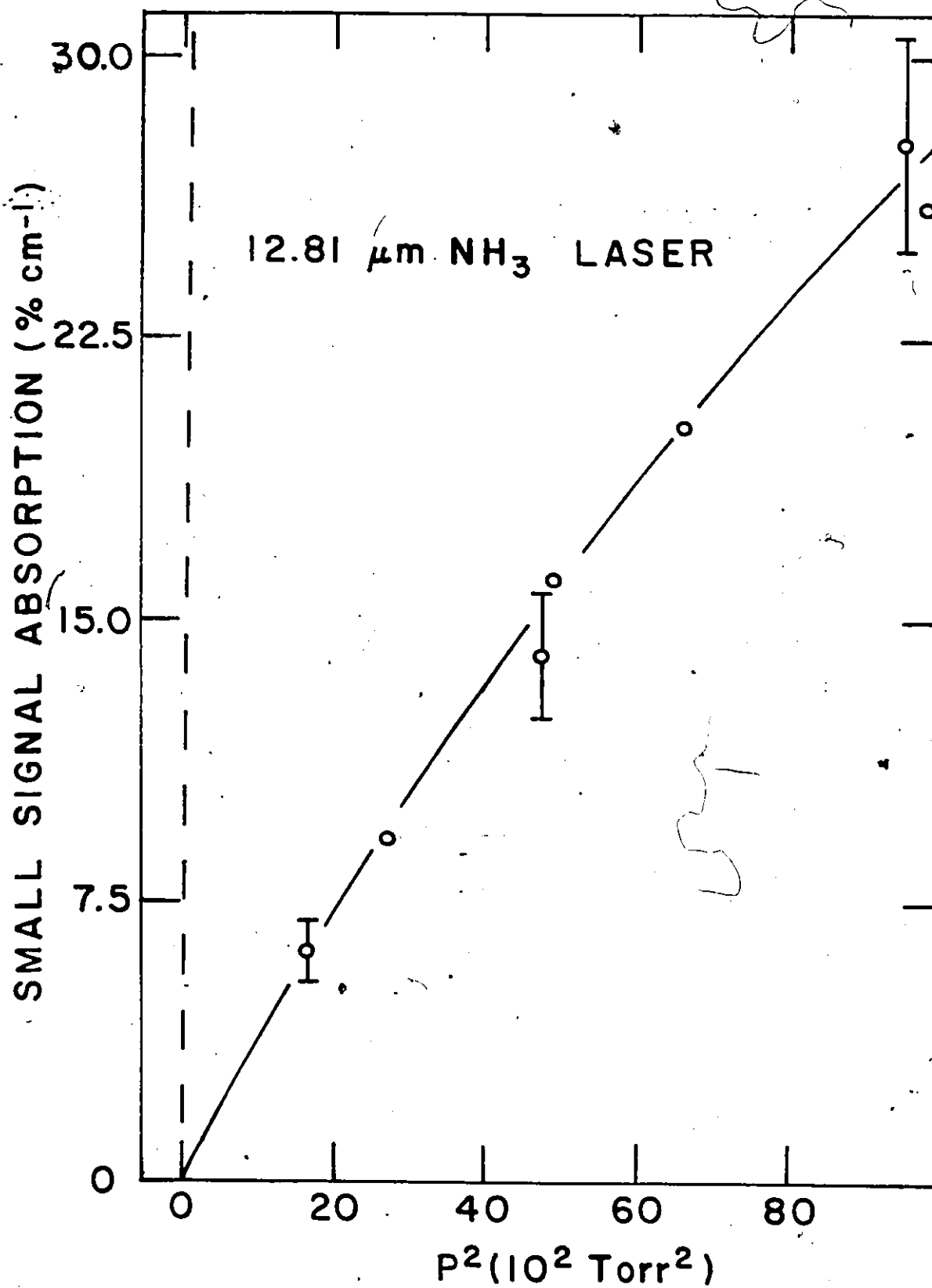
$$\alpha_{\text{mir}}(\nu) = \alpha_{\text{mir}}(\nu_0) \cdot \frac{\Delta\nu_L^2}{\Delta\nu_{\text{mir}}^2 + \Delta\nu_L^2} \quad (3.1)$$

where $\Delta\nu_L$ is the self-broadening width (half width at half maximum HWHM) and varies linearly with pressure. $\alpha_{\text{mir}}(\nu_0)$ is the absorption coefficient at line center (ν_0) and is given by

$$\alpha_{\text{mir}}(\nu_0) = S/\pi\Delta\nu_L \quad (3.2)$$

where S is the transition strength (in $\text{cm}^{-2}\text{atm}^{-1}$). The best fit is shown by the solid line in Fig. 3.3 and is obtained by varying the lasing offset frequency in equation (3.1). The optimum value of $\Delta\nu_{\text{mir}}$ is 1.47 ± 0.21 GHz and agrees well with the pump offset frequency of 1.36 GHz. The dashed line drawn in Fig. 3.3 is the calculated absorption assuming that lasing takes place at line center. Note the large difference between the dashed curve and the experimental measurements. Similar agreement between $\Delta\nu_{\text{mir}}$ and $\Delta\nu_p$ was found for the other 12- μm systems listed in Table 3.1, clearly demonstrating that at low pumping powers Raman processes are responsible for the gain.

Fig. 3.3: Small-signal absorption of the 12.81- μm laser as a function of the square of the NH_3 pressure in an external cell. The solid line is a best fit to the experimental data using a lasing offset frequency of 1.47 GHz. The dashed line indicates the large absorption which would be observed if the 12.81- μm laser was operating at line center.



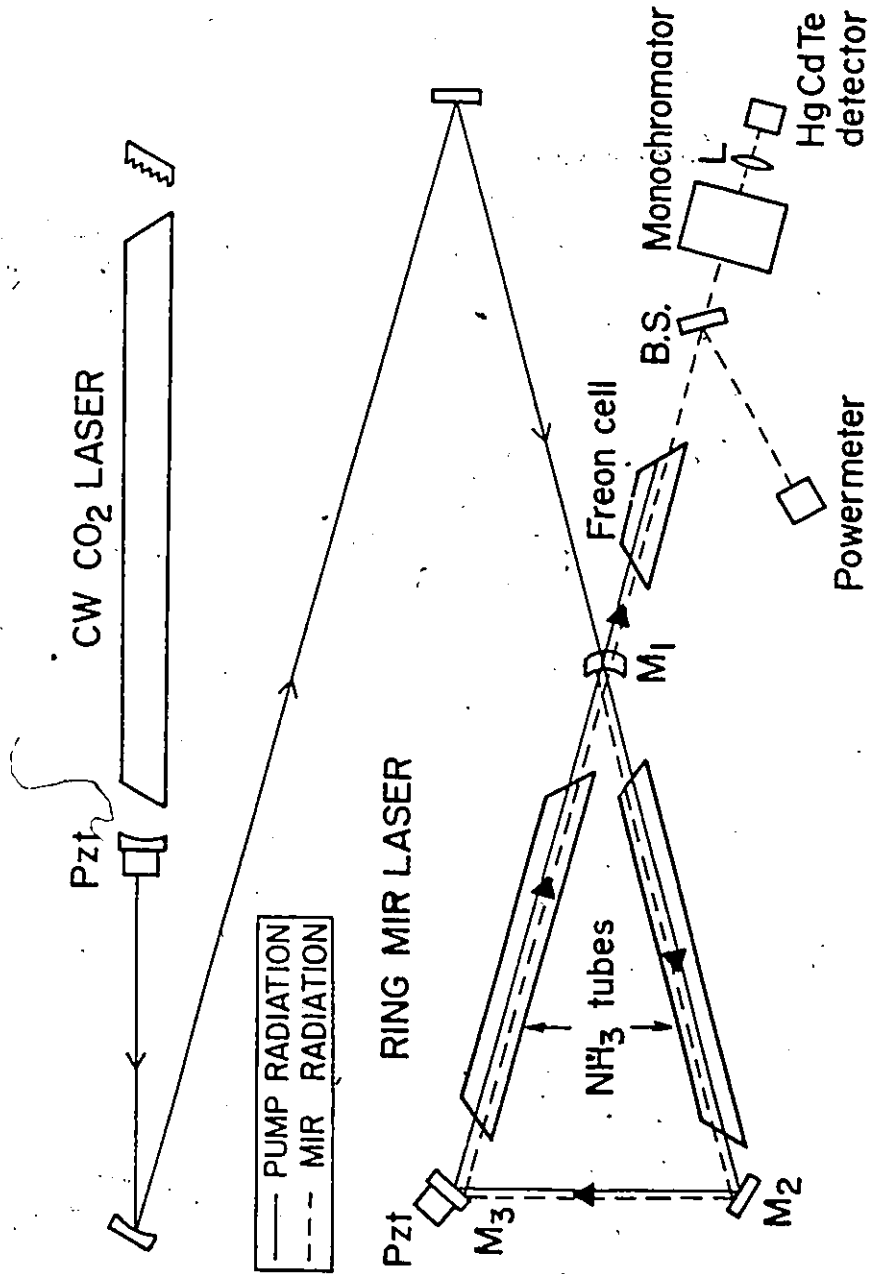
The threshold measurements in Table 3.1 qualitatively illustrate the dependence of the Raman gain as a function of the pump offset. In theory, the Raman gain is inversely proportional to the square of the pump offset and the results of Table 3.1 certainly display a non-linear dependence. An accurate comparison between theory and experiment is not appropriate in the present system because of different cavity losses and buildup times* for the various transitions. The next chapter will examine in detail the dependence of the Raman gain with pump offset.

3.3 CW Optically-Pumped 12.08- μ m Laser

From a practical viewpoint, the very low threshold powers required for 12- μ m lasing presented in the last section showed that power requirements would not be a problem in attaining cw operation. Consequently, the TE CO₂ laser was replaced with a continuous discharge tube. We chose to pump the SP(7,0) transition since its threshold pumping power could easily be attained with a conventional cw CO₂ laser. Our initial attempts were frustrated by strong optical feedback from the input mirror (M₁ in Fig. 3.2) of the MIR cavity into the CO₂ laser. This feedback caused severe instabilities in the CO₂ laser power and prevented true cw operation of the MIR laser. The linear pumping arrangement was thus changed to the ring-laser configuration as shown in Fig. 3.4. The geometry of this pumping scheme completely eliminates the CO₂ feedback since the pump radiation is never reflected back into the CO₂ laser.

* For work with pulsed lasers, an estimate of the peak gain must include a correction to the cavity losses to take into account the excess gain (i.e. gain above the cavity losses) required to build up the MIR pulse from the spontaneous level to detectable levels.

Fig. 3.4: Schematic diagram of the optically-pumped ring laser. The solid line indicates the path taken by the pump radiation while the 12.08- μm copropagating wave follows the dashed line.



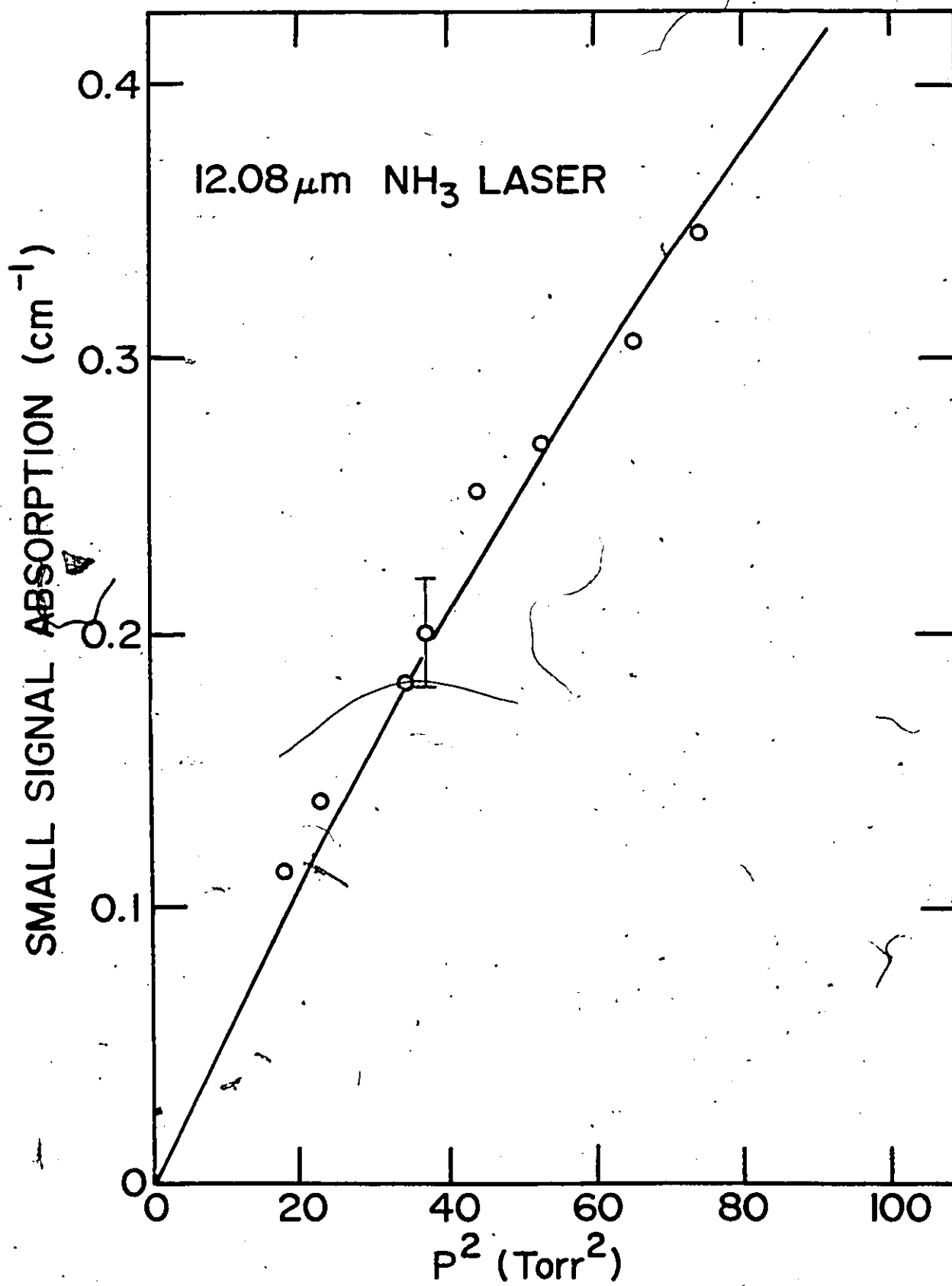
The laser tube has an inside diameter of 8 mm and an active discharge length of ~ 120 cm. The CO_2 cavity is formed by a 40% ZnSe mirror ($R=10$ m) and an original grating ($135 \text{ } \mu\text{m/mm}$) for line selectivity. The pump laser is cooled with methanol and emits ~ 33 W on the $R(30)$ 9- μm band CO_2 laser line. The laser amplitude is dither-stabilized at line center using a closed loop feedback system consisting of a lock-in stabilizer, a piezoelectric translator and a detector located at the grating zeroth-order. The piezoelectric translator applies the feedback correction to the cavity length to lock the laser to maximum power. The NH_3 resonator consists of two 35-cm long brass cells sealed with NaCl Brewster windows. NaCl is employed because it transmits both the 9- and 12- μm radiations with low losses. The CO_2 pump beam is focused into the MIR cavity through the dichroic mirror M_1 (same as in section 3.2.1), and is closely matched to the 12- μm mode size in the NH_3 resonator (TEM_{00} mode $w_0 \sim 2.2$ mm). The optics of the MIR cavity were chosen to provide low cavity losses at 12.08 μm . M_1 has a reflectivity of 95% at 12 μm while M_2 and M_3 are high reflectivity ($\sim 99\%$) broadband mirrors. Mirror M_3 is mounted on both a micrometer translation stage for a coarse tuning of the 12- μm cavity length and a piezoelectric translator for fine adjustments. The 12- μm emission emerges from mirror M_1 collinearly with several watts of CO_2 pump radiation which is removed by selective absorption in a cell containing Freon-12 [57]. The transmitted 12- μm beam is then split into two parts; 98% of the beam is directed to a power meter while the remainder is chopped and focused through a monochromator onto a HgCdTe detector.

3.3.1 Results

CW lasing at 12.08- μm was observed for all pump-power levels above 10 W, provided the MIR cavity length was carefully adjusted using the piezoelectric translator. At the maximum pump power of 33 W, the 12- μm output power was 900 mW at an optimum pressure of ~ 500 mTorr. Optimum MIR output arises when the MIR cavity length is resonant at both 9.22 μm and 12.08 μm . In such cases, the 12- μm output is enhanced by the larger CO_2 power present in the cavity. This enhancement was obtained by moving M_3 through approximately four 12- μm cavity resonance frequencies using the differential screw micrometer. Although no attempt was made to optimize the 12- μm output (the cavity used was substantially undercoupled), the photon conversion efficiency measured in this preliminary experiment was $\sim 4\%$. Chapter 5 describes improvements to the cavity design which resulted in 12- μm output powers in excess of 10 W and photon conversion efficiency $>40\%$.

For low-power pulsed optical pumping, we have shown in section 3.2.1 that the gain mechanism was a Raman process by measuring the exact MIR output frequency. To validate this interpretation for cw operation, we have determined the MIR lasing frequency by recording the absorption of the cw 12.08- μm output in an external NH_3 cell. Figure 3.5 shows the small-signal absorption of the 12.08- μm laser plotted against the square of the pressure in the external NH_3 cell. The solid line is a best fit to the experimental data obtained using line strength and linewidth values from Taylor [41], the Lorentzian profile given by equation (3.1) and by varying the lasing offset frequency $\Delta\nu_{\text{mir}}$. The fitted value of the offset was 170 MHz with an

Fig. 3.5: Absorption coefficient of the cw $12.08\text{-}\mu\text{m}$ laser as a function of the square of the NH_3 pressure in an external cell. The solid line is a best fit to the experimental data using a lasing offset frequency of 170 MHz and Taylor's calculated values for line strength and linewidth [41].

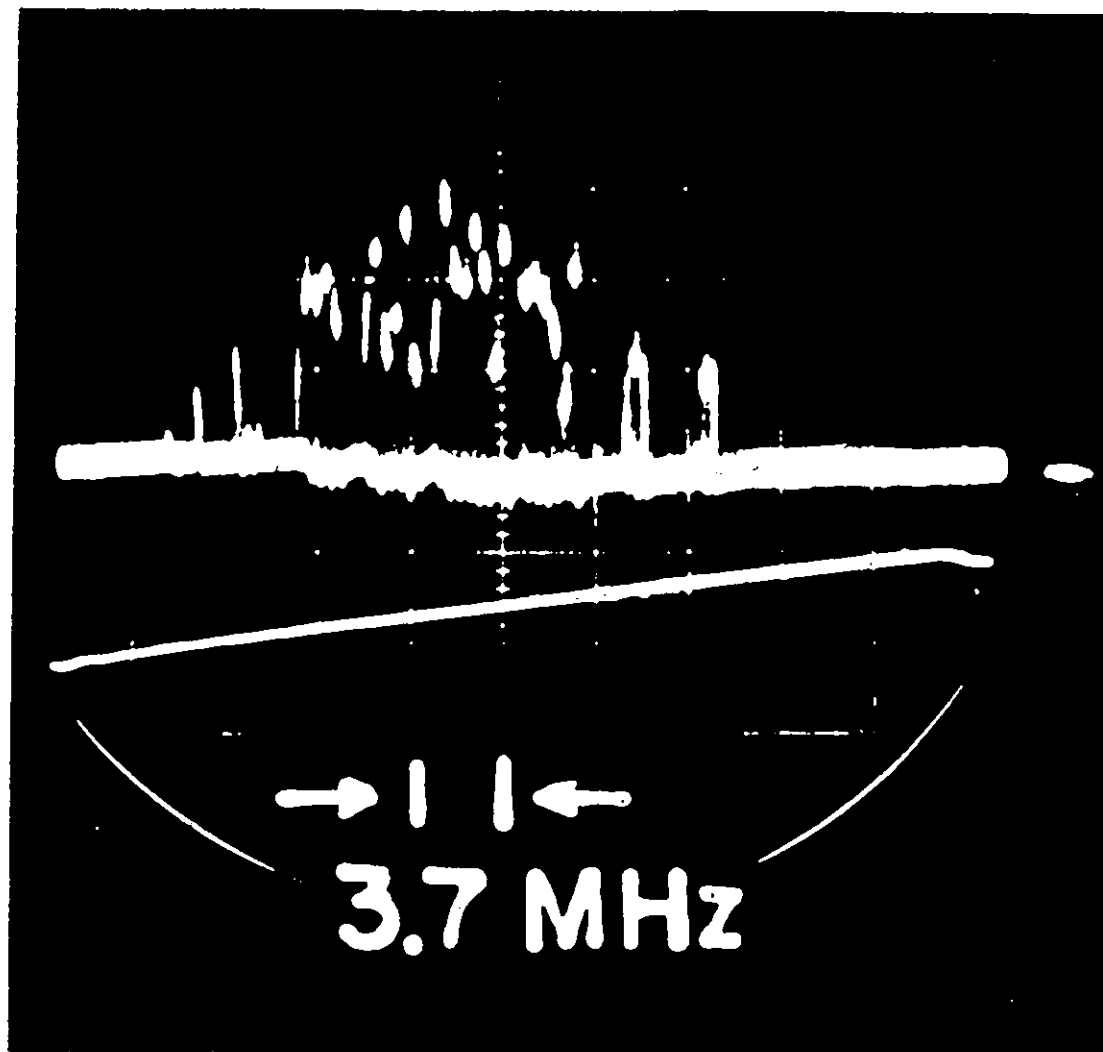


estimated uncertainty of ± 15 MHz. This value compares reasonably well with the pump offset frequency (190 ± 7 MHz) and confirms the Raman nature of the cw 12.08- μ m laser.

The Raman emission exhibits other features which distinguish it from a single-photon process. For the copropagating wave, the Raman linewidth should be roughly equal to the difference between the Doppler width of the pumped and emission lines (i.e. 23 MHz FWHM) as discussed in the previous chapter. The Raman linewidth was estimated by recording the 12- μ m output power as a function of the ring resonator length while the NH_3 cavity length was scanned over the gain bandwidth with the aid of a piezoelectric translator. The lower trace of Fig. 3.6 shows the linear ramp applied to the piezoelectric translator (linearity within 5%). The total variation of the ramp corresponds to a frequency change of 37 MHz in the position of the cavity modes. The upper trace of Fig. 3.6 displays the chopped (~ 1 kHz) 12.08- μ m signal as the ramp progresses. Although the CO_2 laser was stabilized at line center, small amplitude and frequency fluctuations in the pump caused a modulation in the NH_3 output. The effect of this modulation was particularly severe when the MIR laser was detuned from its peak output, and results in the gaps seen near both ends of the cavity scan. The results shown in Fig. 3.6 were taken with the pumping set at twice the threshold value and a Raman linewidth of ~ 25 MHz (FWHM) was estimated from the envelope of the upper trace*. This width compares favorably

*This linewidth estimate utilizes the fact that Raman gain is proportional to pump intensity.

Fig. 3.6: Chopped 12.08- μm output as a function of the MIR resonator length. The lower trace displays the linear ramp applied to the MIR piezoelectric translator. The horizontal scale is 3.7 MHz per division.



with the initial estimate of 23 MHz, and is much narrower than the Doppler width in NH_3 at 12 μm (~ 74 MHz FWHM). Another consequence of the Raman nature of the gain is that any 12- μm photon propagating in a direction counter to the pump beam will experience a gain profile which is much wider (~ 176 MHz) but with a much smaller peak value (see Fig. 2.4). We have looked for the presence of a counterpropagating 12- μm beam and as expected lasing was not observed in this direction.

3.4 Discussion and Conclusions

This chapter describes the first experiments performed on optically-pumped MIR lasers using low-power laser pulses. The mechanism responsible for the optical gain in such lasers is clearly identified as a Raman-type two-quantum process. This circumstance is very beneficial to the operation of low-power off-resonantly pumped MIR lasers. The presence of the Raman process obviates the need for a population inversion and the consequent high pumping intensities. Indeed, under our pumping conditions a very strong absorption exists at the 12- μm line center. It is only because the 12- μm Raman gain is shifted to the far wings of this absorption profile that lasing can take place. The enhancement of the Raman gain as the pump offset is decreased is illustrated in the threshold pumping measurements of Table 3.1. With smaller pump offsets (< 90 MHz) the single-photon process becomes increasingly important as we transfer a significant fraction of the pumped level population to the upper laser level. This situation will be discussed in Chapter 7 when the pump frequency is shifted into coincidence with the line center of an NH_3 transition.

In establishing the threshold dependence on pump offset, we were able to obtain threshold pumping powers well within the reach of conventional cw CO₂ lasers. Based on these results, we produced the first optically-pumped cw laser operating on a vibrational-rotational transition. As expected, a two-photon process was demonstrated to be the dominant mechanism responsible for the 12- μ m gain. Our scheme is general and can be applied to other transitions in NH₃ (as shown in Chapter 5) or other molecular gases to produce many additional cw laser lines in a spectral region where powerful cw sources are almost nonexistent. The experiments performed in section 3.3.1 show several important characteristics of the cw 12.08- μ m laser. However, further improvements of the present cavity design require a better understanding of the gain dynamics. The next chapter gives a detailed quantitative description of the 12- μ m small-signal gain using a tunable diode laser as a probe. These measurements led to the construction of the high power cw 12.08- μ m laser described in Chapter 5.

CHAPTER 4

INVESTIGATIONS OF THE 12- μ m SMALL-SIGNAL GAIN

4.1 Introduction

The previous chapter described the operation of a 1 W optically-pumped cw 12.08- μ m Raman laser. The pumping scheme is potentially scalable to higher powers, applicable to other wavelengths, and opens the way to the development of new sources of powerful line-tunable cw lasers in the MIR region. Full exploitation of the potential of this new laser system requires a detailed understanding of the laser dynamics, and thus we have carried out a comprehensive investigation of the R(30)-pumped NH_3 system. This chapter presents extensive measurements of the small-signal gain made in amplifier cells using a 12- μ m tunable diode laser (TDL) as a probe. These measurements allow us to develop an understanding of the various mechanisms involved in the lasing process. The experiment is compared with the theory of two laser fields interacting with a three-level system over a wide range of conditions. Gain coefficients are measured for both the co- and counter-propagating radiation and the NH_3 pressure is varied from <200 mTorr (Doppler broadening region) to \sim 1 Torr (mixed broadening), at which pressure heating effects become significant. Gain measurements are made in both large diameter and waveguide amplifiers. The use of a capillary tube as a waveguide allows a large range of pump intensities over significant interaction lengths to be investigated. The wide tunability of the TDL is fully exploited in the measurements

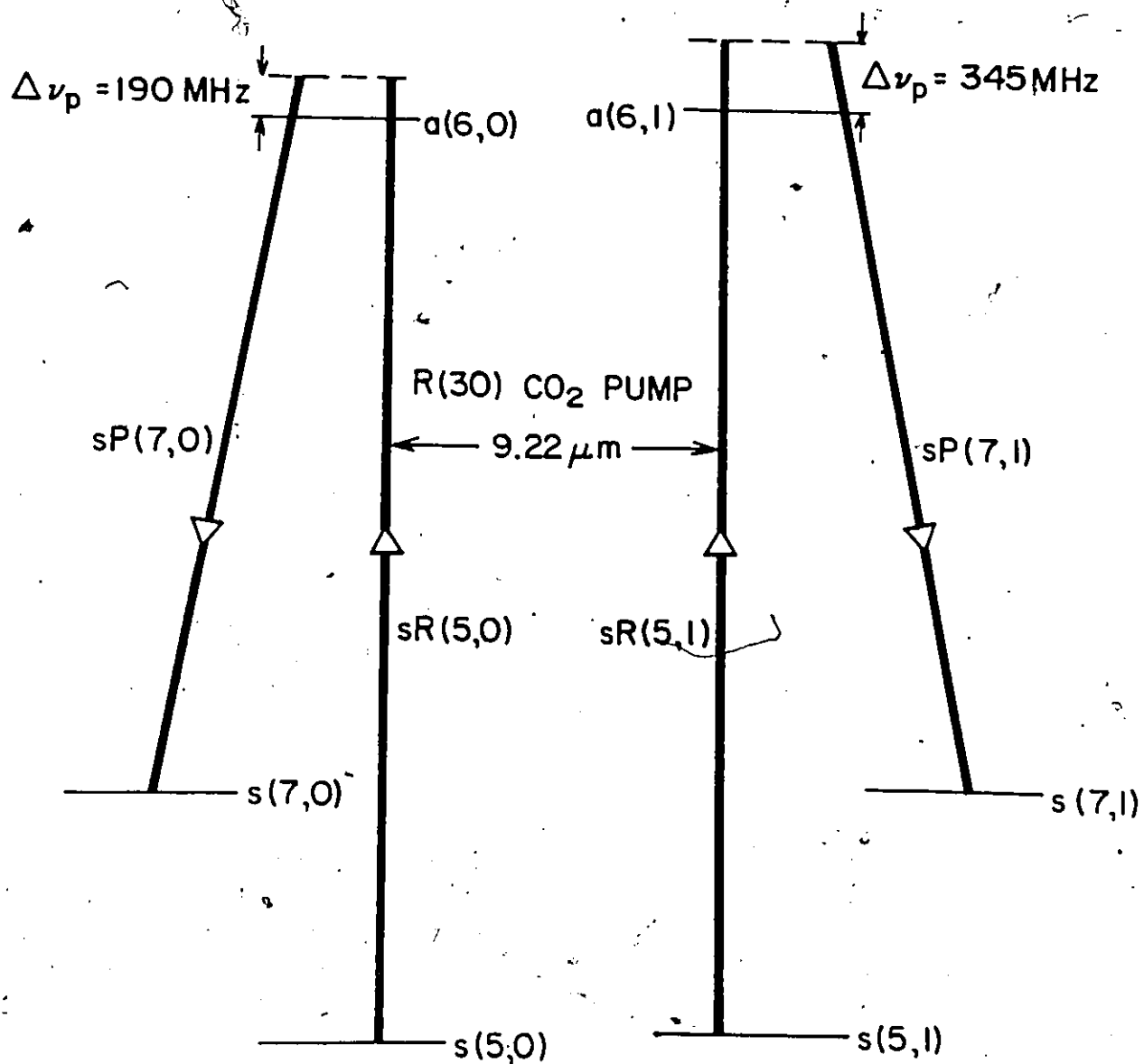
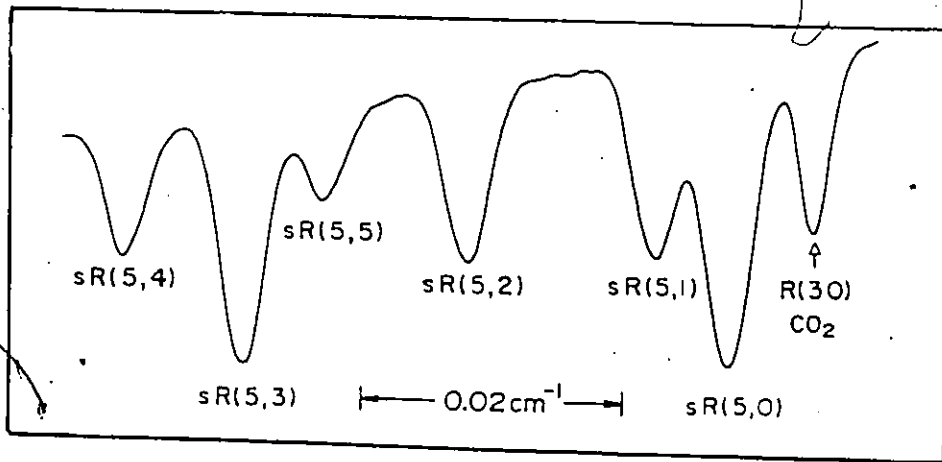
of Raman gain as a function of pump offset frequency presented in section 4.3. Pump offsets from 190 MHz up to 1.55 GHz are studied. The influence of the polarization states of the pump and probe beams on the gain is also examined.

4.2 Experimental Technique and Preliminary Results

Figure 4.1 illustrates the pumping scheme used in this work. The R(30) 9- μm CO_2 laser line is in near coincidence with the sR(5,K) manifold in NH_3 . The pump offset frequency varies from 190 ± 7 MHz [40] for the sR(5,0) line to 1547 ± 2 MHz for the sR(5,4) [58]. Our experiment consists in pumping the sR(5,K) multiplet with an intense 9.22- μm radiation field and probing the gain induced on the associated sP(7,K) transitions using a 12- μm tunable diode laser. The measurements are then compared with the theory of two laser fields interacting with a three-level system described in Chapter 2.

Previous research has been reported for both resonant and offset Raman transitions in optically-pumped cw FIR lasers and good agreement was found between experiment and a theory based on a density matrix formalism [37,59-61]. However, experiments in the far-infrared are difficult to carry out because of a lack of stable and tunable sources. There are several practical advantages to be realized in studying Raman processes in the MIR region. The chief one is the availability of TDLs to probe the MIR gain. TDLs are widely tunable and can probe frequencies far from the lasing transition; one is not limited to the narrow frequency interval commonly present in conventional oscillator-amplifier measurements. This feature becomes particularly

Fig. 4.1: Simplified energy level diagram of NH_3 . The insert is a TDL scan of the $\text{sR}(5, \text{K})$ multiplet in NH_3 near 1084.6 cm^{-1} . Also shown is the $\text{R}(30) \text{ CO}_2$ absorption line indicated by an arrow. The relevant energy levels of the transitions with the two smallest pump offsets are illustrated below.

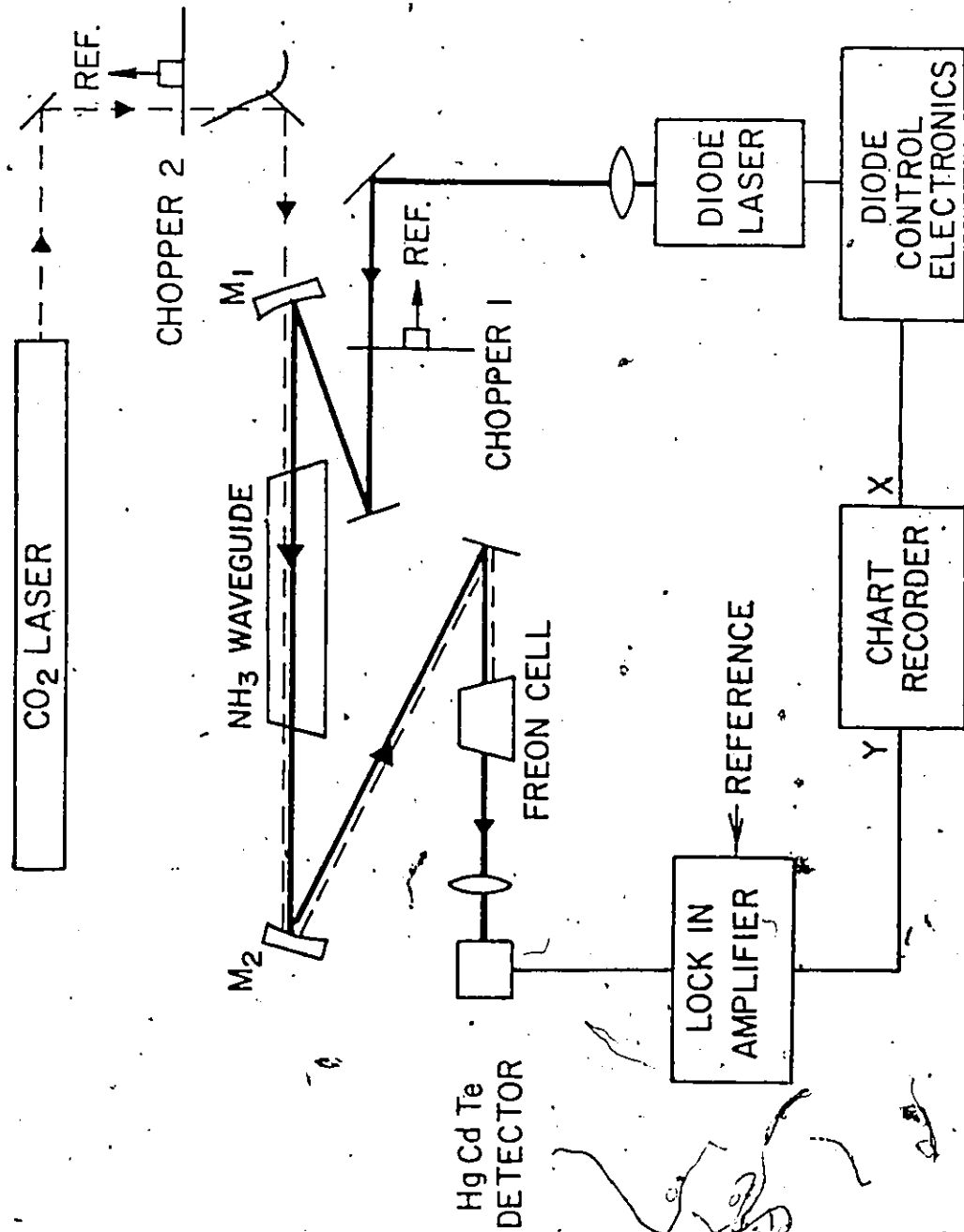


useful for off-resonantly pumped transitions where small values of Raman gain can appear at a wavelength not generally available from a probe oscillator. The TDL can also be tuned to a variety of transitions in the NH_3 molecule to monitor population changes and increases in temperature induced by absorption of the pump radiation. In addition, the exceptional amplitude and frequency stability of the TDL allow gain to be measured with very high sensitivity. Gain coefficients as low as 0.001 %/cm were monitored using the TDL in conjunction with a phase sensitive detection technique.

We have carried out gain measurements over a wide range of amplifier conditions, using the apparatus shown schematically in Fig. 4.2. Coarse tuning of the wavelength emitted from the PbSnSe tunable diode laser is controlled by the junction temperature, which can be set between 10-70 K, while the fine tuning of the laser emission is obtained by varying the drive current supplied to the diode. The junction temperature and the operating current of the TDL were adjusted to give single-mode operation near 827 cm^{-1} . A dither-stabilized* cw CO_2 laser emitting 33 W on the R(30) 9- μm transition is used to pump two types of NH_3 cell: a 3-cm i.d. cell which allows the pump beam to propagate in a free space mode and a pyrex capillary tube which acts as a waveguide for both the 9- μm and 12- μm radiation. These cells will be referred to as the open cell and waveguide, respectively. The 26-cm long open cell was used to make measurements with a well-

*The frequency modulation used to keep the CO_2 laser tuned to peak power had no measurable effect on the 12- μm gain line shape.

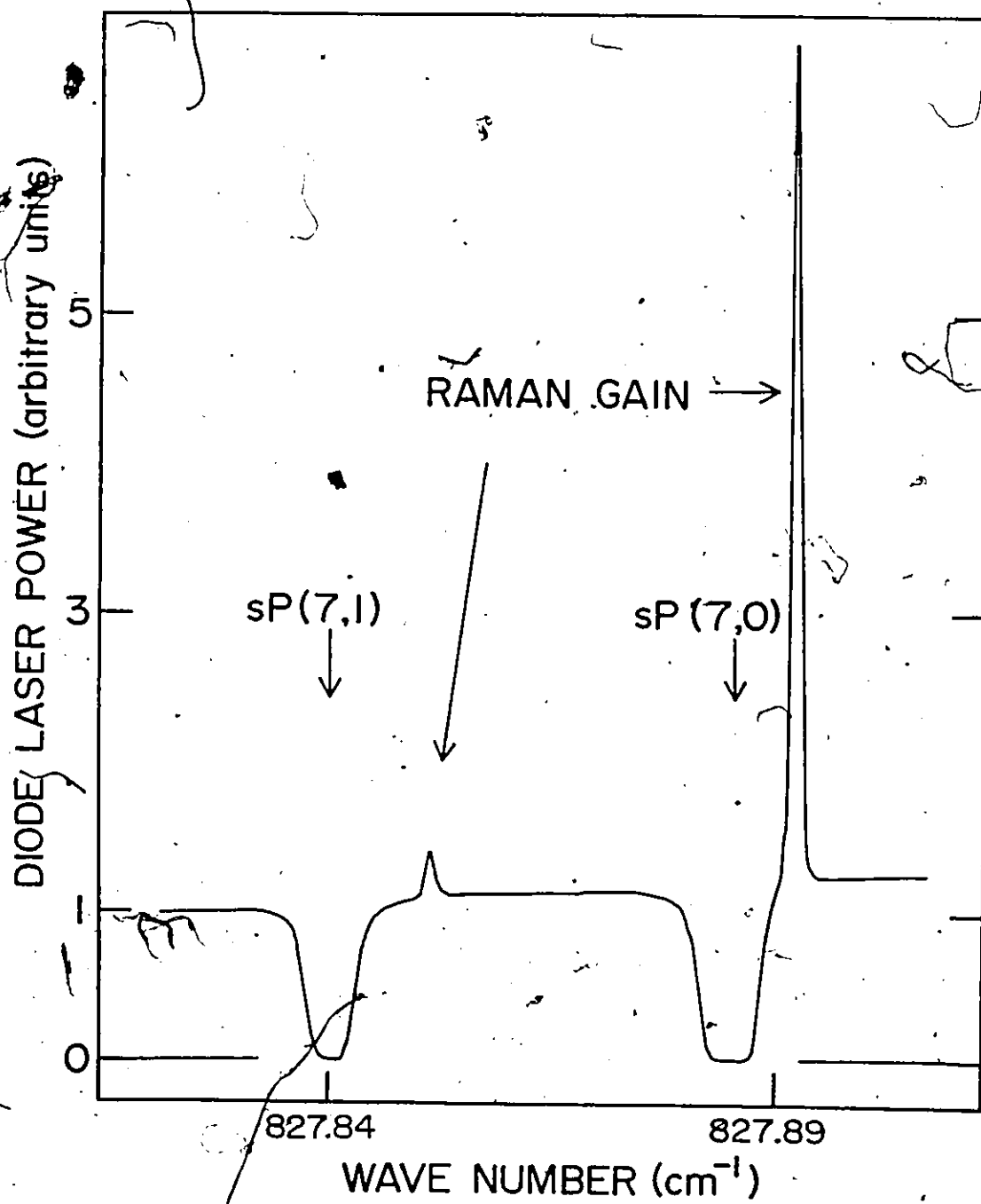
Fig. 4.2: Schematic diagram of the apparatus used for the copropagating small-signal gain measurements. The pump CO_2 beam is represented by a dashed line and the probe TDL beam by a solid line. Dichroic mirrors M_1 and M_2 transmit 90% of the $9\text{-}\mu\text{m}$ CO_2 radiation and reflect 97% of the $12\text{-}\mu\text{m}$ beam. Two types of cell are probed; either a large diameter cell or a waveguide capillary tube. The Freon cell is used to prevent residual CO_2 radiation from reaching the HgCdTe detector.



characterized pump intensity. The small bore waveguides (1.5-mm bore, 60-cm long and 1.65-mm bore, 15-cm long) were employed whenever a high intensity pump beam was required. Figure 4.2 illustrates the case where the TDL and CO_2 beams are copropagating in the amplifier cell. For counterpropagating experiments, the CO_2 laser beam is sent through M_2 instead of M_1 . In both cases, the 9- and 12- μm beams are carefully aligned to give maximum spatial overlap. The TDL radiation is focused on a HgCdTe detector after the residual 9- μm light is eliminated with a Freon-12 cell. The signal at the detector is fed into a lock-in amplifier and the resulting dc voltage goes into the Y-axis of a recorder. The X-axis of the chart recorder is driven by the diode control electronics which gives an output proportional to the drive current.

Two different detection schemes were implemented. For direct detection, chopper 1 acts on the TDL amplitude to give a conventional scan of TDL transmission versus wavelength. When high-sensitivity gain measurements were needed, chopper 1 was removed and chopper 2 was used for synchronous detection. The detection system is now sensitive only to changes in the TDL transmission induced by the CO_2 beam. By using the second technique, changes as small as 0.02% could be routinely measured. Figure 4.3 displays an example of a conventional amplitude scan taken in a 1.5-mm bore, 60-cm long waveguide. The strong line center absorptions show that the pump intensity is insufficient to create a population inversion between the upper and lower laser levels. The two narrow Raman gain spikes are associated with the $\text{SP}(7,0)$ and $\text{SP}(7,1)$ transitions. The offsets of both Raman peaks from their respective line center were determined to be $186 \pm$

Fig. 4.3: TDL scan of the $sP(7,0)$ and $sP(7,1)$ transitions in the presence of CO_2 radiation. The two sharp spikes offset from the line center absorptions are the Raman transitions associated with the $sP(7,0)$ and $sP(7,1)$ lines. The pump and TDL probe beams are copropagating in a 60-cm long waveguide. Pump intensity is $\sim 1 \text{ kW/cm}^2$ at an NH_3 pressure of $\sim 800 \text{ mTorr}$.

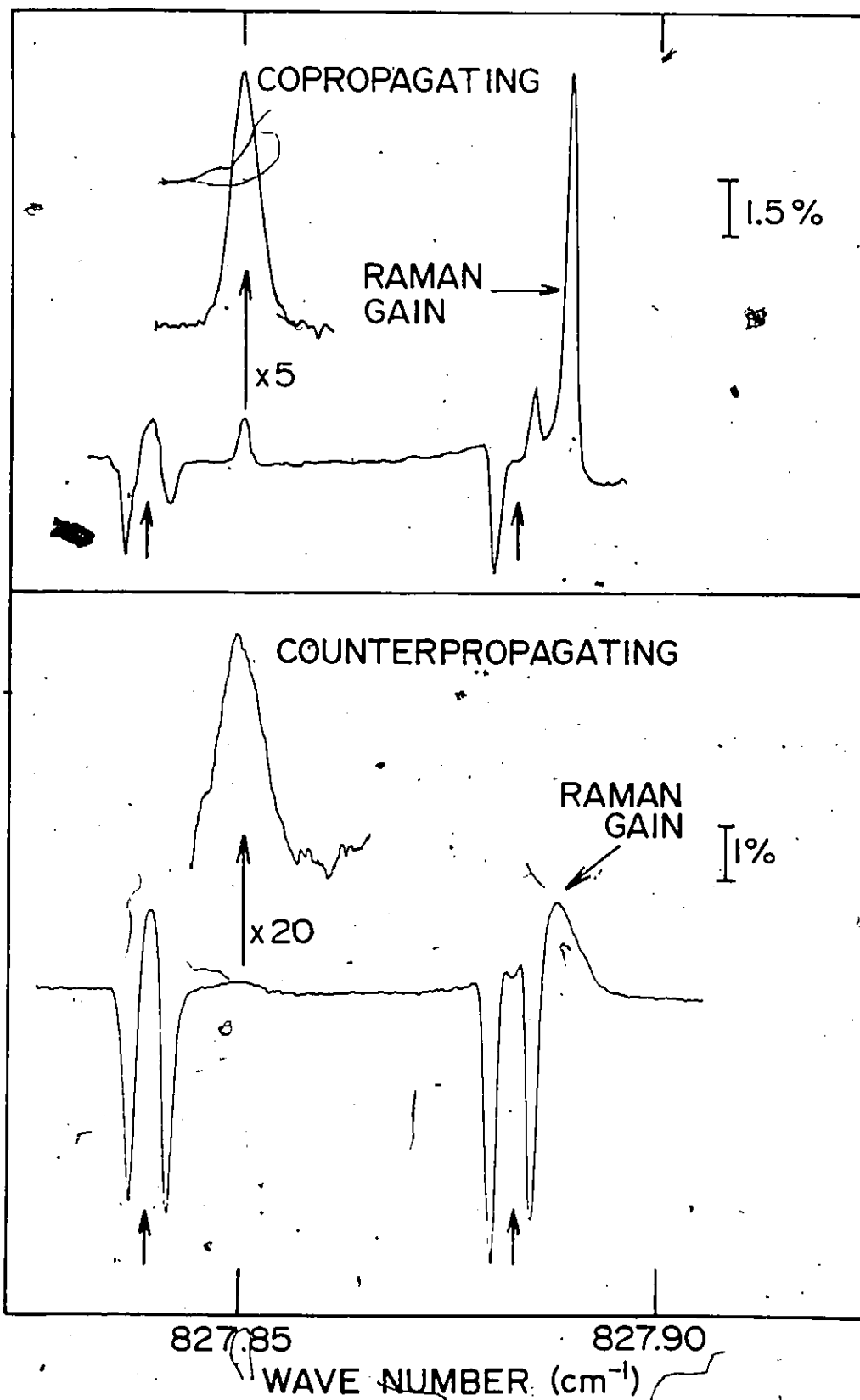


13 and 365 ± 13 MHz, in reasonable agreement with the previously measured pump offset frequencies of 190 ± 7 MHz [40] and 345 ± 2 MHz [58] respectively. The smaller Raman amplitude of the $\text{SP}(7,1)$ line in Fig. 4.3 is expected from the inverse square relationship between the Raman gain and the pump offset. Gain coefficients as high as 3.1%/cm were measured on the $\text{SP}(7,0)$ transition with a CO_2 laser intensity of $\sim 1 \text{ kW/cm}^2$. These large gains have important consequences for the design of practical systems as shown in section 4.4.

While scans of the type shown in Fig. 4.3 give a direct display of the Raman gain and line center absorption, a much more sensitive detection technique involves the use of chopper 2. The upper trace in Fig. 4.4 displays typical results obtained by chopping the copropagating CO_2 beam and synchronously detecting the TDL. This technique is sensitive only to changes in TDL transmission induced by the CO_2 laser. The measurements were taken in a 26-cm long open cell at an NH_3 pressure of ~ 400 mTorr and for a pump intensity of $\sim 200 \text{ W/cm}^2$. In this upper scan, the large line center absorptions seen in Fig. 4.3 are replaced by much smaller change signals, which reflect a combination of population transfer and gas heating induced by the CO_2 pump beam. The line center signals (indicated with the vertical arrows) were found to be alignment and pressure dependent, and were observed with reduced amplitude on NH_3 transitions other than the $\text{SP}(7,K)$ multiplet. Figure 4.4 shows Raman gain near both the $\text{SP}(7,0)$ and $\text{SP}(7,1)$ transitions. The lower trace of Fig. 4.4 was taken with the CO_2 laser beam passing through the NH_3 cell in the direction opposite to the TDL beam. As predicted by

Fig. 4.4: High-sensitivity scans of 12- μm Raman gain. The CO_2 laser is chopped and the TDL beam synchronously detected. Results are given for co- and counter-propagating beams in $\sim 400\text{-mTorr}$ NH_3 . Average pump intensity is $\sim 200 \text{ W/cm}^2$. The line centers of both the $\text{SP}(7,0)$ and $\text{SP}(7,1)$ lines are indicated with arrows. In each trace, the Raman feature near the $\text{SP}(7,1)$ line is shown on an expanded scale. In addition to the indicated amplitude expansion, the wave number scale has been expanded in the upper trace by a factor of 4. The signals observed near the $\text{SP}(7,0)$ and $\text{SP}(7,1)$ line centers are discussed in the text.

DIFFERENTIAL TDL SIGNAL



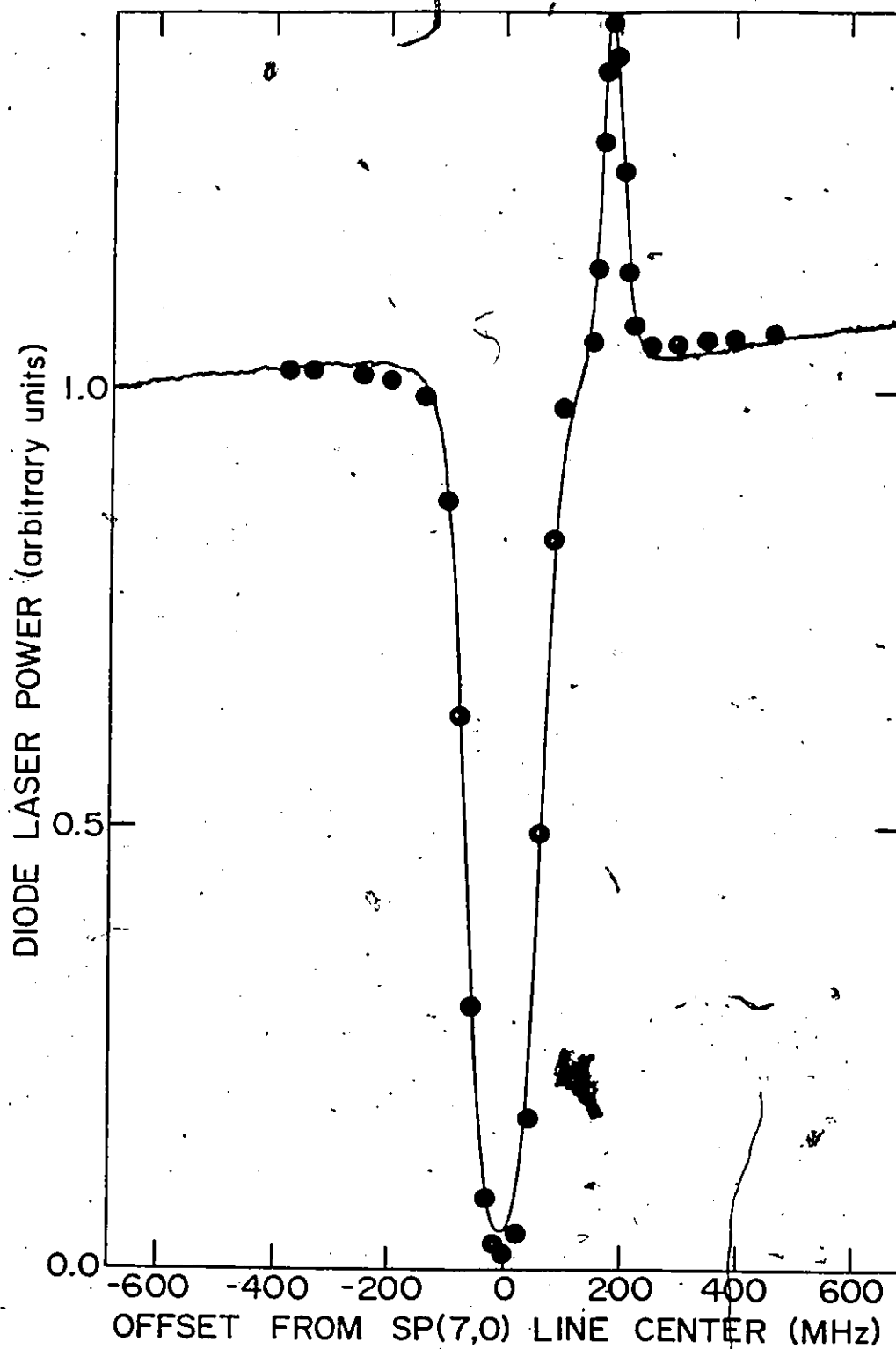
theory (see Fig. 2.4), the Raman features are much smaller and broader than in the copropagating case.

Line shapes such as those illustrated in Figs. 4.3 and 4.4 can be reproduced using our computer model. For example, Fig. 4.5 compares a direct TDL amplitude scan of the $\text{SP}(7,0)$ transition (solid line) with a calculated spectrum (•) based on the theory given in Chapter 2. This measurement was made in a 1.65-mm bore, 15-cm long capillary tube at a pressure of 500 mTorr and an incident CO_2 input power of ~ 14 W. For the purpose of this comparison, a theoretical pump intensity of 900 W/cm^2 was chosen to fit best the amplitude of the Raman gain. The fitted pump intensity compares reasonably well with the experimental average pump intensity* of 750 W/cm^2 . The sloping background in the experimental scan (caused by the variation of the TDL power with current) was taken into account in the calculation. Note that the model reproduces closely the entire TDL spectrum†. At low pressure, the limiting linewidth of the Raman line shape was measured as 28 ± 3 MHz (FWHM) in the copropagating case whereas the counterpropagating linewidth was 176 ± 11 MHz (FWHM). These results are in good agreement

* This average is carried out in both transverse and longitudinal directions. The transverse average simply consists in dividing the pump power by the waveguide area. For the longitudinal direction, we utilize the fact that the pump amplitude decreases exponentially along the waveguide length. Consequently, our average pump intensity is calculated as $I_{\text{avg}} = I_0(1 - \exp(-\alpha L))/\alpha L$ where I_0 is the incident intensity on the waveguide, α the absorption coefficient and L the waveguide length.

† The small difference between the experimental and calculated line center absorption is well within the range produced by the uncertainties in the input parameters used in our computer model.

Fig. 4.5: Comparison of experimental and theoretical spectra near the $SP(7,0)$ transition. The solid line is a conventional TDL scan taken with 500 mTorr of NH_3 in a 15-cm long waveguide. The calculated spectrum (\bullet) uses a pump intensity of 900 W/cm^2 to best fit the experimental peak gain. The sloping background caused by the TDL is included in the calculation.



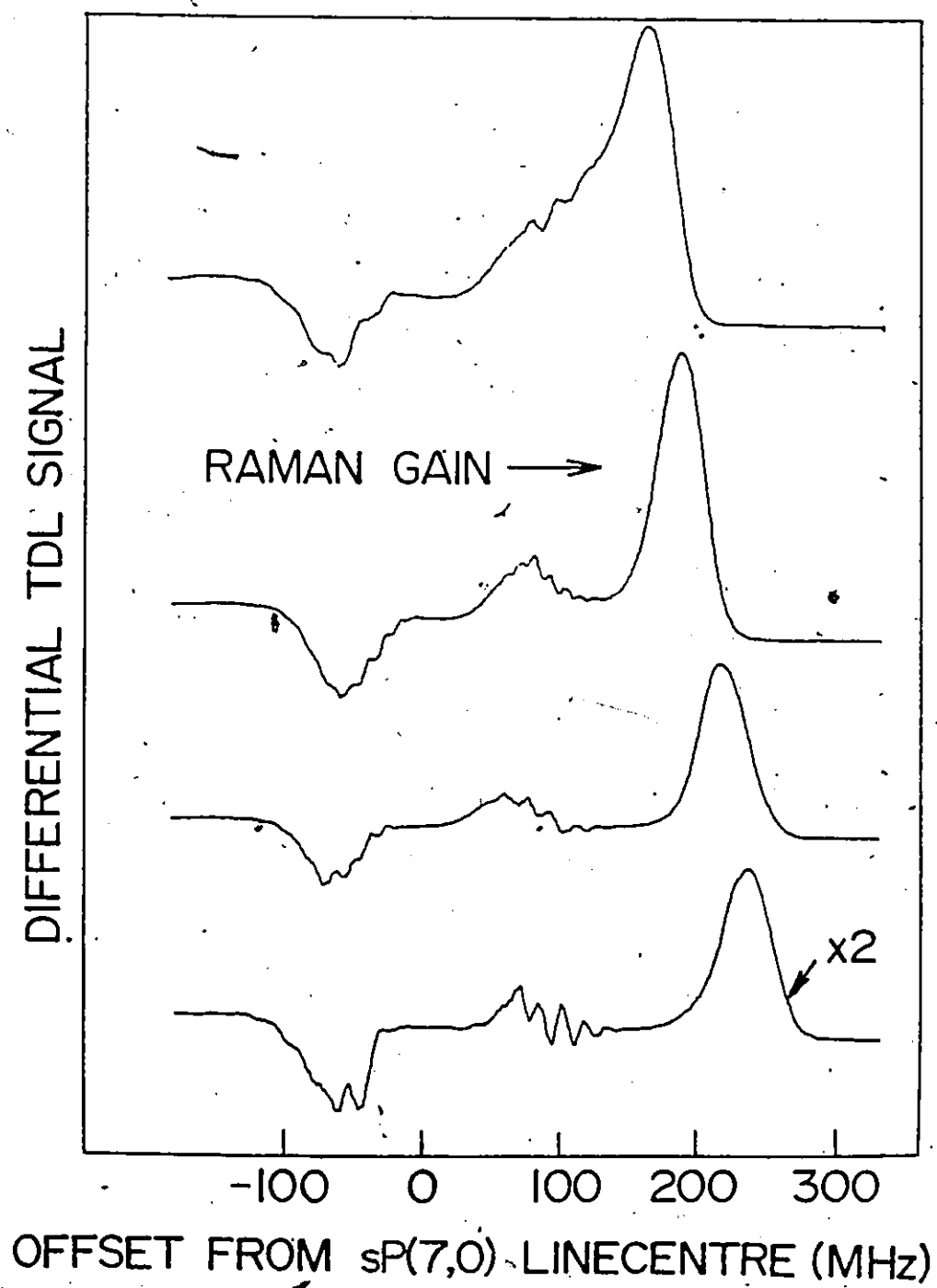
with the model predictions of 26 MHz and 176 MHz for the co- and counter-propagating cases.

An important characteristic of the Raman process is the strong dependence of the Raman peak gain on the pump offset frequency. Figure 4.6 illustrates the frequency tuning of the Raman gain with pump offset. The four scans in Fig. 4.6 were taken by tuning the CO_2 laser frequency in steps of ~ 25 MHz using a piezoelectric translator. As expected, the frequency of the Raman gain line center moves by amounts equal to the pump frequency shifts. Figure 4.6 also shows in a qualitative fashion the increase in Raman gain as the pump offset is reduced. No attempt was made to carry out quantitative measurements, since the CO_2 laser power also varies when its output mirror is tuned by the piezoelectric translator. In the next section, a different technique is employed to measure the amplitude variation of the Raman gain with pump offset.

4.3 Detailed Small-Signal Gain Measurements

Using the two detection techniques described in section 4.2, detailed measurements of the Raman peak gain were made as a function of pump intensity, pressure, pump offset and polarization, and the results were compared with the computer model. In addition to validating the theoretical model over a wide range of experimental conditions, these results are very useful in the design of efficient $12\text{-}\mu\text{m}$ lasers as discussed in section 4.4. Most of the data presented in this section deal with the Raman gain associated with the $\text{sp}(7,0)$ transition. This line gives higher gain values than the other $\text{sp}(7,K)$ levels and enables

Fig. 4.6: Differential scans of the $\text{sp}(7,0)$ region taken to illustrate the frequency tuning of the Raman gain. Results are shown as the CO_2 laser is tuned from -25 to 50 MHz around the line center. The TDL signal in the bottom trace was expanded by a factor of 2. The measurements were made in the 26-cm open cell at an NH_3 pressure of only ~ 300 mTorr to minimize pressure broadening.



relative gain measurements to be made with good accuracy (typically $\sim \pm 5\%$). However, similar results were obtained for the $sp(7,1)$ line and clearly our approach can be extended to other NH_3 pumped lines.

At a fixed NH_3 pressure, theory predicts that the Raman gain increases linearly with pump intensity in the range of experimental conditions investigated ($\leq 1 \text{ kW/cm}^2$). Preliminary measurements in both the open and waveguide cell confirmed this prediction. The open cell was used to make a comparison between theory and experiment for absolute gain as the pump intensity can be accurately measured in this cell.

The linearity of the gain was checked in a 1.65-mm bore waveguide which provided a large range of pumping intensity. For the measurements in the open cell, the pump CO_2 beam was collimated to give a uniform spot size (TEM_{00} mode with a beam diameter of $\sim 1 \text{ cm}$ at the 1/e intensity points) along the cell. The TDL was tightly focused ($\sim 2\text{-mm}$ diameter) at the center of the CO_2 beam and used to probe 500 mTorr of NH_3 pumped by a well-defined intensity of $15 \pm 2 \text{ W/cm}^2$ over a length of 26 cm. Slight heating of the gas occurs due to absorption of the 9- μm pump radiation. Variation in the gas temperature changes the thermal population in the different levels and thus the Raman gain value. By tuning the diode laser to the $sp(2,0)$ and $sp(10,2)$ transitions in NH_3 , absorption coefficient changes resulting from gas heating were monitored. The temperatures corresponding to these absorption coefficients were then computed. The NH_3 gas temperature in the probed region was estimated to be $320 \pm 10 \text{ K}$ for the absolute gain measurements and this temperature was used for the theoretical gain calculations.

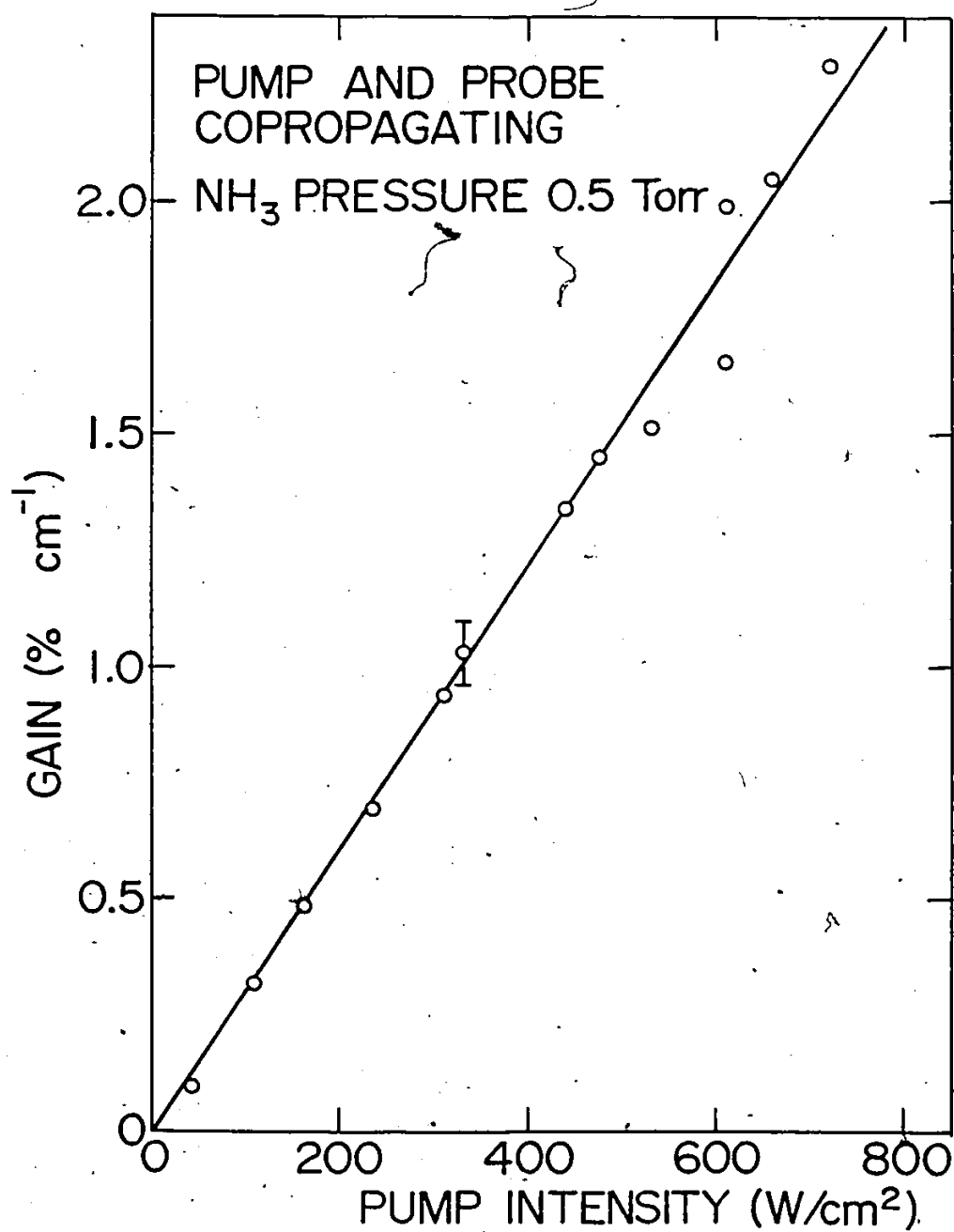
In the copropagating case, the peak Raman gain was measured to be 2.37

$(\pm 10\%) \times 10^{-5} \text{ cmW}^{-1}$ *, 15% lower than the theoretical prediction. In the counterpropagating case, the measured Raman gain is smaller, $4.03 (\pm 15\%) \times 10^{-6} \text{ cmW}^{-1}$, and is 27% lower than theory predicts. In view of the uncertainties in some of the experimental parameters and the input data (see section 2.4.3), this represents a good agreement between theory and experiment.

Figure 4.7 shows results obtained by varying the pump intensity in the waveguide. In this case, the CO_2 pump and TDL probe beams are copropagating in a waveguide mode and the measured gain coefficient is the result of a convolution of the TDL probe with the radially varying Raman gain profile. A further complication occurs due to the radial temperature profile in the NH_3 gas. Even though the NH_3 pressure was reduced below optimum to minimize heating effects, the average gas temperature is $345 \pm 10 \text{ K}$ at the maximum pump intensity. This temperature change was measured using the technique described above. Since the TDL probes the entire cross section of the waveguide, the temperature increase represents an average over the radial temperature profile of the NH_3 gas. In Fig. 4.7, the Raman gain is plotted against the average pump intensity in the waveguide. The solid line is a best-fit straight line through the data points. The slope of this line is $3.04 \times 10^{-5} \text{ cmW}^{-1}$ close to the calculated value of $2.75 \times 10^{-5} \text{ cmW}^{-1}$ for 500 mTorr NH_3 at 320 K. The waveguide measurements should not be used for accurate comparisons of absolute gain since such measurement requires a precise knowledge of the pump and probe intensity profiles and their spatial overlap. However, the data of Fig. 4.7 clearly display the linearity of the Raman gain with pump

*The Raman gain values are normalized with respect to the pump intensity.

Fig. 4.7: Raman gain coefficient as a function of pump intensity measured in a 15-cm long waveguide at a constant pressure of 500 mTorr. The best fit straight line through the data gives a slope of $3.04 \times 10^{-5} \text{ cmW}^{-1}$.



intensity and also indicate the gain magnitude to be expected at high pumping intensities. The consequences of these results for the design of practical systems will be discussed in section 4.4.

The variation of the 12- μm Raman gain with NH_3 pressure is illustrated in Figs. 4.8 and 4.9. The measurements were taken with the open cell for both co- and counter-propagating beams. In the copropagating case, the gain is proportional to pressure below ~ 200 mTorr (Fig. 4.8(a)) and starts to level off at pressures above 600 mTorr (Fig. 4.8(b)). The nonlinear dependence of the Raman gain on pressure above ~ 200 mTorr results from a significant increase of the Raman gain linewidth compared to its low-pressure limit of 26 MHz. The situation is quite different in the counterpropagating case where the minimum Raman linewidth is 176 MHz. As the self-broadening coefficient of the lasing transition is 19 MHz/Torr (FWHM), the results in Fig. 4.9 display the expected linear dependence at pressures up to 500 mTorr. Measurements were not taken at higher pressures due to excessive gas heating and significant broadening of the $\text{sp}(7,0)$ line center absorption. These pressure measurements were performed utilizing tightly focused beams to obtain appreciable gain. An average pump intensity was estimated from the measured beam waist. In Figs. 4.8 and 4.9, the calculated gain coefficients were scaled by 0.63 and 0.76 respectively, to give a best fit to the experimental data. This reduction in the calculated values is consistent with our measurements of absolute gains combined with the uncertainties in the average pump intensity. Once again the overall experimental behavior is well reproduced by the theory.

Fig. 4.8: Raman gain coefficient as a function of NH_3 pressure for copropagating beams. The low-pressure range is displayed in (a) and the high-pressure in (b).

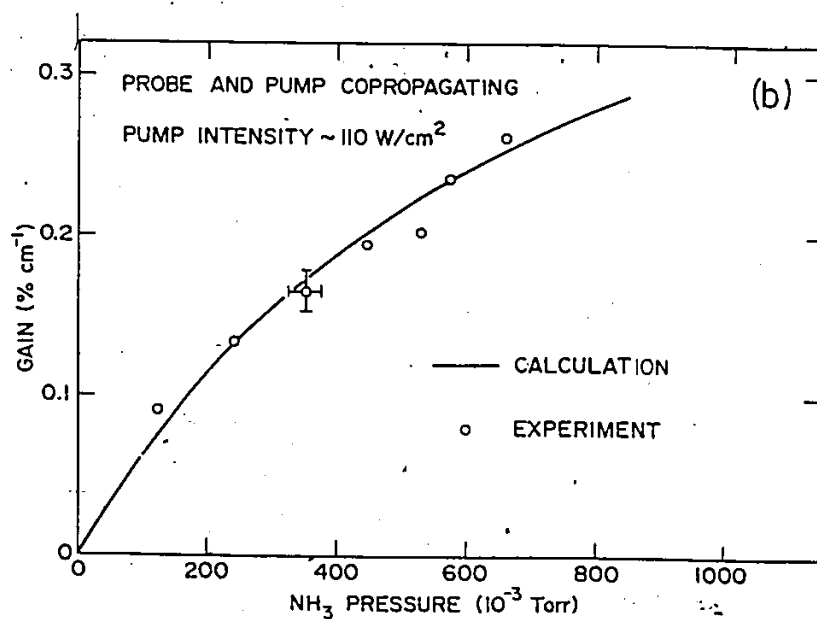
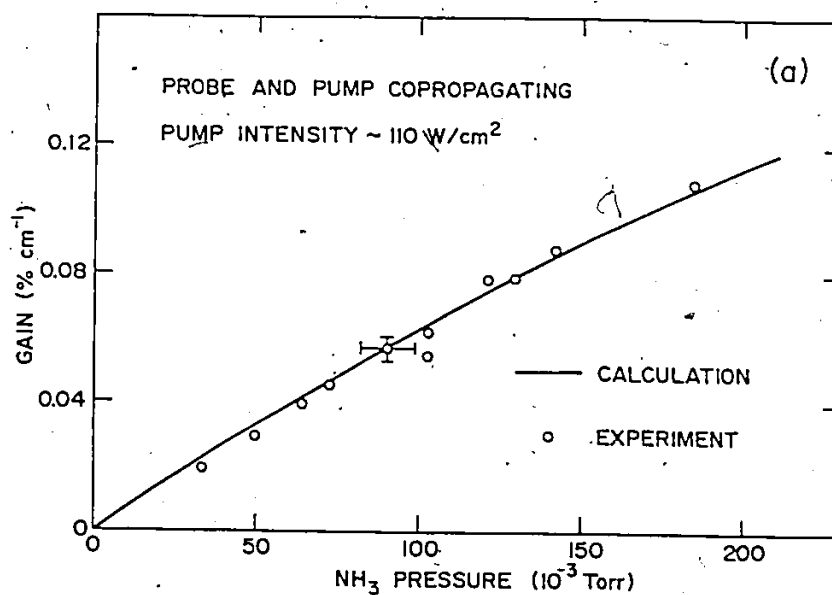
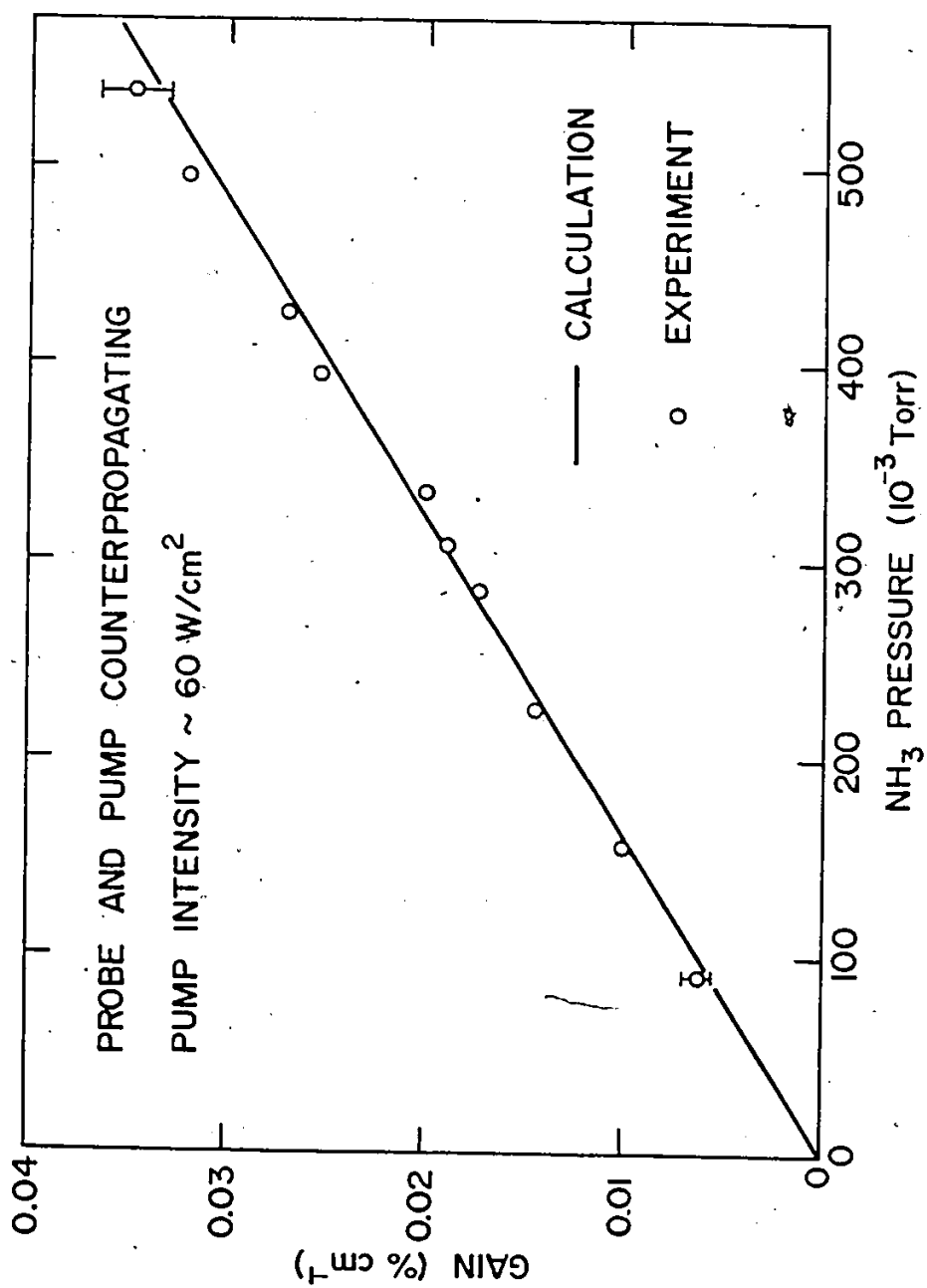


Fig. 4.9: Raman gain coefficient as a function of NH_3 pressure for counterpropagating beams.



Figures 4.6 illustrated qualitatively the importance of the pump offset frequency on the Raman gain of the $sp(7,0)$ line. To make quantitative observations, we utilize the fact that the $R(30)$ CO_2 line actually pumps six different NH_3 lines with varying offsets, as shown in Fig. 4.1. These offset frequencies are well known [40,58], and our TDL could be tuned to five of the coupled $sp(7,K)$ transitions near $12\ \mu m$. The measurements were carried out in a 1.5-mm bore, 60-cm long waveguide with a NH_3 pressure of 500 mTorr and an average pump intensity of $\sim 1\ kW/cm^2$. The Raman gain coefficients were measured on the five lines under identical experimental conditions and the results were then normalized to the $sp(7,0)$ line. A similar procedure was used for the calculated values with Taylor's published linewidths as input parameters [41]. Results are summarized in Table 4.1. The good agreement between theory and experiment indicates that the theoretical model accurately predicts the pump offset dependence of the gain. The existence of an inverse square relationship between the gain and pump offset can be ascertained from Table 4.1 by normalizing the gain to the same pump and lasing transitions. The high sensitivity of the TDL was invaluable in performing this experiment; typical gain coefficients observed in the $sp(7,5)$ line were only 0.006%/cm. As expected, the Raman gain for each transition was offset from line center by a frequency equal to the pump offset frequency (see Fig. 4.3).

All the results described so far were obtained using 9- μm pump and 12- μm probe beams which had parallel linear polarizations. However, the small-signal gain is expected to depend strongly upon the relative polarization of pump and probe beams. This dependence results from the

Table 4.1

Gain ratio versus pump offset.

Transition	Pump Offset (MHz)	Measurement	Calculation
sP(7,0)/sP(7,0)	190	1	1
sP(7,1)/sP(7,0)	345	0.12(1)	0.12
sP(7,2)/sP(7,0)	761.3	0.023(2)	0.020
sP(7,4)/sP(7,0)	1546.7	0.0025(3)	0.0022
sP(7,5)/sP(7,0)	1075.6	0.0020(2)	0.0020

M-degeneracy of the levels and the values taken by the individual matrix elements for different polarizations of the pump and emitted radiations. Petuchowski and DeTemple [62] have published results for high-J transitions (a reasonable approximation for the $sR(5,K)$ transitions). Measurements were made to compare the parallel linear case to the situation where the pump and probe beams have orthogonal linear polarizations. Our arrangement used two wire-grid polarizers in the path of the probe beam, and the rotation of one of them by 90° provided a direct comparison between parallel and orthogonally linearly polarized beams. If our measurements are normalized to the parallel linear case, for orthogonally linearly polarized pump and probe beams the gain coefficient should be reduced by 0.75. A reduction of 0.76 ± 0.02 was measured in the waveguide. For circularly polarized beams, Petuchowski and DeTemple [62] predict factors of 0.25 and 1.5 for corotating and counterrotating beams, respectively. A Fresnel prism was employed as a $\lambda/4$ plate to produce circular polarized light, and approximate factors of 0.2 (± 0.05) and 1.3 (± 0.1) were obtained in the co- and counter-rotating cases respectively and thus the strong dependence of the gain on polarization was confirmed.

4.4 Discussion and Conclusions

The experiments described in this chapter constitute one of the most detailed tests carried out on the interaction of two laser fields with a three-level molecular system. The validity of the theory was established over a wide range of experimental conditions and thus the model can be used with confidence to predict gain on other NH_3 lines.

In particular, this work has several practical implications for the construction of efficient cw 12- μm lasers. The data of Fig. 4.7 demonstrate that gain coefficients of 1%/cm can be attained in a waveguide for input powers of only 10 W (equivalent to 400 W/cm² in a 1.65-mm bore capillary tube). Such gain coefficients are more than sufficient for the construction of compact 12- μm waveguide lasers. In Chapter 3, a ring resonator was utilized for the 12- μm cavity to prevent feedback to the pump CO₂ laser. A linear waveguide configuration can be used provided a polarizer and a $\lambda/4$ plate decouple the two laser cavities [63]. The waveguide is then pumped with circularly polarized radiation leading to a further enhancement of the 12- μm gain by a factor of 1.5. This gain increase is beneficial to the operation of 12- μm lasers since it diminishes the threshold pumping power requirements and thus leaves a greater fraction of the 9- μm input radiation available to be converted into 12- μm photons. Based on the results of this chapter, a linear waveguide 12- μm laser was constructed with output powers in excess of 10 W and quantum conversion efficiency >40%. The design and performance of this laser are the subjects of the next chapter.

CHAPTER 5

HIGH POWER CW 12- μ m NH_3 LASER

5.1 Introduction

This chapter describes the design and performance of an efficient 12.08- μ m NH_3 Raman laser. The 12- μ m cavity design is based on results discussed in the previous chapter, in particular, on the fact that large Raman gains can be produced in small-bore capillary tubes. Our preliminary experiments on cw 12.08- μ m laser (section 3.3) produced 0.9 W at 12 μ m using 33 W of 9- μ m pump radiation in a non-optimized system. More recent work using similar pump powers reported 12- μ m output powers of 1.5 W in pure NH_3 , and 3.3 W in a buffered mixture of NH_3 with He or H_2 [64,65]. In all these experiments the NH_3 cavity consisted of an open resonator pumping a ring configuration to avoid feedback into the pump laser. In view of the difficulty of constructing a ring waveguide cavity, we chose a linear pumping scheme in which the isolation of the pump laser from the NH_3 cavity was accomplished using circularly polarized light [63]. Results with this simple configuration are given in this chapter for different waveguide bores and lengths. Threshold pumping powers as low as 1 W are measured in our optimum 12- μ m cavity. The consequence of such low thresholds for the extension of cw operation to other off-resonantly pumped NH_3 transitions is discussed in section 5.3.

5.2 Experimental Apparatus and Results

Figure 5.1 shows a schematic diagram of the apparatus, which contains a major improvement over that used in our initial work. The NH_3 is now confined in a capillary tube acting as a waveguide for both the 9- μm and 12- μm radiation. This enables high pumping intensities to be maintained over long interaction regions, greatly enhancing the single pass Raman gain at 12 μm . Furthermore, the use of a waveguide facilitates cooling of the NH_3 gas at the walls. Feedback of the pump radiation from the 12- μm input mirror into the CO_2 laser is eliminated with a wire-grid polarizer and a Fresnel prism [63]. This isolation scheme functions as follows. The pump beam emerges from the Fresnel prism with, for example, left-circular polarization. The pump radiation reflected from the NH_3 laser is right-circularly polarized and is transformed by the Fresnel prism into a linearly polarized beam. However, the reflected pump radiation is now linearly polarized in a plane perpendicular to the transmission axis of the wire-grid polarizer and thus no reflected pump radiation reaches the CO_2 laser. As a result, careful adjustment of the prism allows feedback to the pump to be eliminated. This technique has the additional benefit that a factor of 1.5 increase in the 12- μm Raman gain is generated due to the use of circularly polarized rather than linearly polarized pumped radiation [62]. Brewster windows can no longer be utilized in this NH_3 cavity, and the waveguide ends are sealed by slightly tilted pieces of AR (anti-reflection) coated ZnSe (transmission >98% at 12.08 μm and 88% at 9.22 μm). The mirrors in the NH_3 cavity




Fig. 5.1: Schematic diagram of the optically-pumped 12- μm waveguide laser.

are placed as close as possible to the ends of the waveguide (~ 0.5 cm) to minimize coupling losses* [66]. The input mirror is mounted on a piezoelectric translator to tune the cavity into resonance. The $12\text{-}\mu\text{m}$ output power is separated from the collinear pump radiation transmitted through the waveguide by a combination of two dichroic mirrors (same mirrors as in Chapter 4). This arrangement allows us to monitor simultaneously the $12\text{-}\mu\text{m}$ output power on a calibrated Scientech power meter and on a HgCdTe detector. The gas pressure in the waveguide is measured with a capacitance manometer.

Preliminary experiments performed with the 1.5-mm bore, 56-cm long waveguide were described in Chapter 4. One watt cw was obtained for 20 W of pumping power corresponding to an energy conversion efficiency of 5%. This efficiency is a factor of two larger than that obtained in our initial experiments (see Chapter 3). However, there are problems in using bores of 1.5 mm or smaller. The optical propagation loss increases with decreasing diameter [67] and significant $9\text{-}\mu\text{m}$ and $12\text{-}\mu\text{m}$ transmission losses were measured in the 1.5-mm bore tube ($>20\%$ loss in 56 cm). The tube diameter was thus increased to 2.5 mm resulting in a $9\text{-}\mu\text{m}$ transmission $>95\%$ in a 60-cm long tube. Initially, our experiments consisted of varying the length of the waveguide, and optimizing NH_3 pressure and output coupling for different capillary tubes. For several measurements, the $12\text{-}\mu\text{m}$ waveguide was surrounded with dry ice as calculations based on the computer model

*Experimentally, we found that the waveguide mirror separation could be increased to ~ 2 cm without a significant decrease in the $12\text{-}\mu\text{m}$ output power.

predicted an increase of ~ 1.5 in the optimum small-signal gain if the NH_3 gas temperature was reduced from 300 K to 195 K. The larger gain obtained at lower temperature results mainly from a reduction in the thermal population of the lower laser level which increases the population difference driving the Raman gain. Table 5.1 summarizes results obtained for various lengths of 2.5-mm bore tubing. Maximum 12- μm output power was achieved in the longest available tube of 1.2 m. Higher output powers may be produced in longer capillary tubes. However, the increase is expected to be marginal because of the increased waveguide losses and the low pumping intensity present in the additional part of the tube. For some applications, shorter waveguides may be advantageous since they are much easier to align and optimize than the 1.2-m tube while still producing significant output powers. The larger 12- μm output powers measured in longer waveguides are the results of lower threshold pumping powers. Low threshold values leave a larger fraction of the pump power available to be converted into 12- μm photons. Optimum output coupling was found to be 25%-50% in the 1.2-m tube and the measurements displayed in Table 5.1 were taken with an output coupler which transmitted 28% of the 12- μm radiation, and 23% of the residual 9- μm radiation.

Investigations were carried out to determine the effect of varying gas pressure and mixture. Optimum NH_3 pressures were found to be close to the pressure which gives the peak small-signal gain calculated from the average longitudinal pump intensity (see section 4.2). For example, the optimum NH_3 pressure was calculated to be 450 mTorr

Table 5.1
Performance of the 2.5-mm bore waveguide laser.

Tube length (cm)	Pumping Power (W)	12- μ m Output Power (W)		Threshold Pumping Power (W)		Optimum Pressure (mTorr)	
		Room Temp	Cooled	Room Temp	Cooled	Room Temp	Cooled
120	38	8	10.5	5.5	3.8	475	300
60	35	5.3	7.3	9.5	5	660	480
20	34	1.1	-	17.5	-	800	-

($T=300$ K) and 350 mTorr ($T=200$ K) in the 1.2-m long waveguide, in good agreement with the measurements of Table 5.1. Figure 5.2 displays the 12- μ m output power versus NH_3 pressure. The maximum operating pressure is limited by strong absorption of the pump radiation by the pressure broadened $\text{sR}(5,0)$ transition. At 1 Torr, this effect reduces the average pump intensity to $\sim 1/3$ of the value in the evacuated capillary tube. The influence of buffer gases was also examined as the addition of such gases to NH_3 have been shown to be beneficial in work reported by Wazen and Lourtioz [65]. Figure 5.3 shows pressure scans of the 12- μ m power in pure NH_3 and buffered mixtures of 50% and 5% NH_3 in He. Similar results were obtained with other mixtures and using N_2 as a buffer gas. Contrary to the results of Wazen *et al.* [65], mixtures of NH_3 with He did not increase the 12- μ m output power. The difference in these two experimental results is probably explained by the fact that wall cooling dominates in our waveguide cell, while Wazen *et al.* required a low mass buffer gas to improve the thermal conductivity of NH_3 in an open resonator. The main effect of dilute NH_3 mixtures in our experiments is to allow higher total pressures to be attained.

The dependence of the 12- μ m output power on pump intensity was measured to characterize further the performance of this new laser system. Figure 5.4 is a plot of 12- μ m output power as a function of CO_2 input power. Measurements were made for both a room temperature and a dry-ice cooled 1.2-m long tube. The majority of the data displayed in Fig. 5.4 were taken with a 1/5th duty cycle chopper in the pump beam to prevent damage to the optical components, particularly the

Fig. 5.2: 12- μm output power as a function of NH_3 pressure for an input power of 31 W at 9 μm . The 1.2-m long capillary tube was not cooled for these measurements.

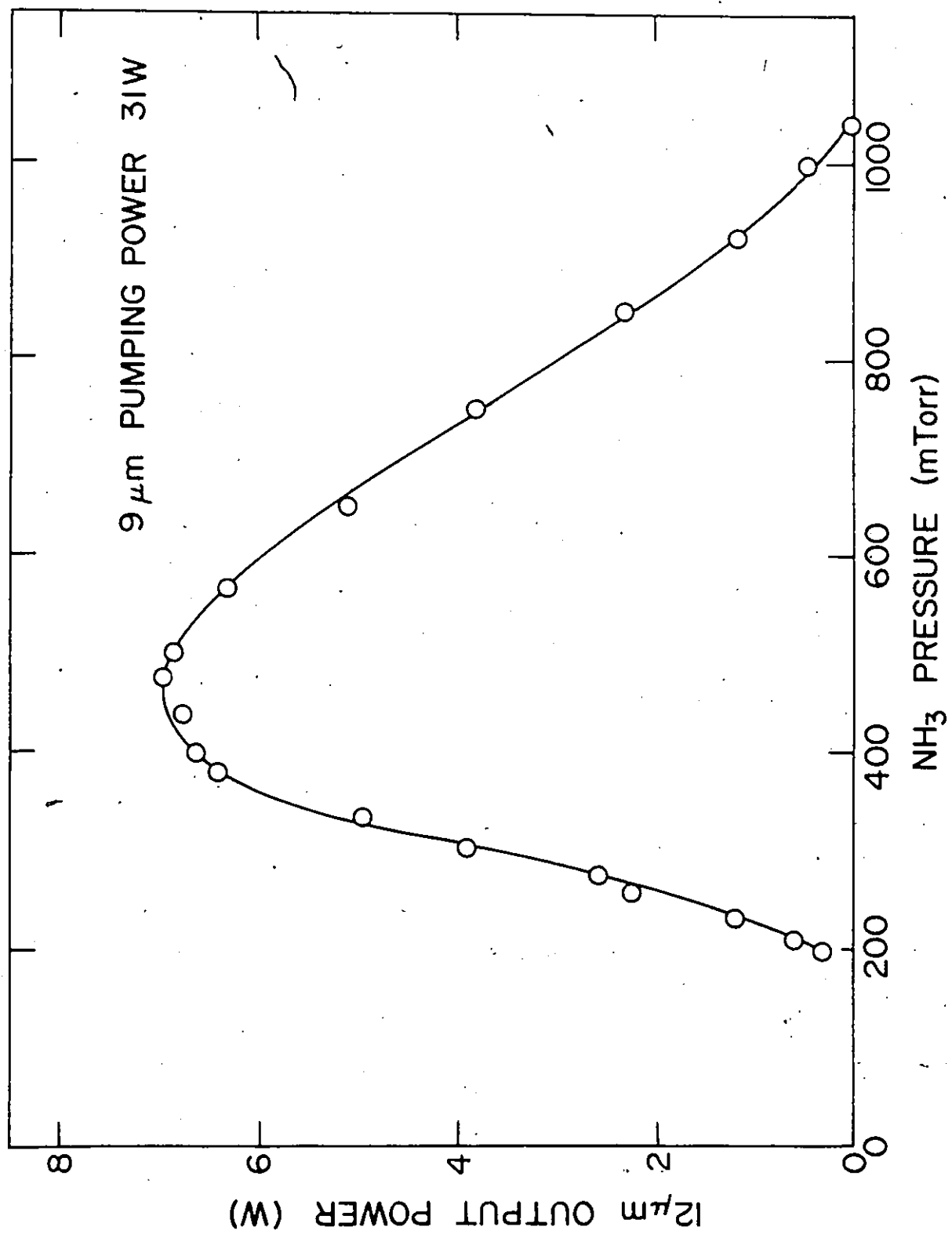
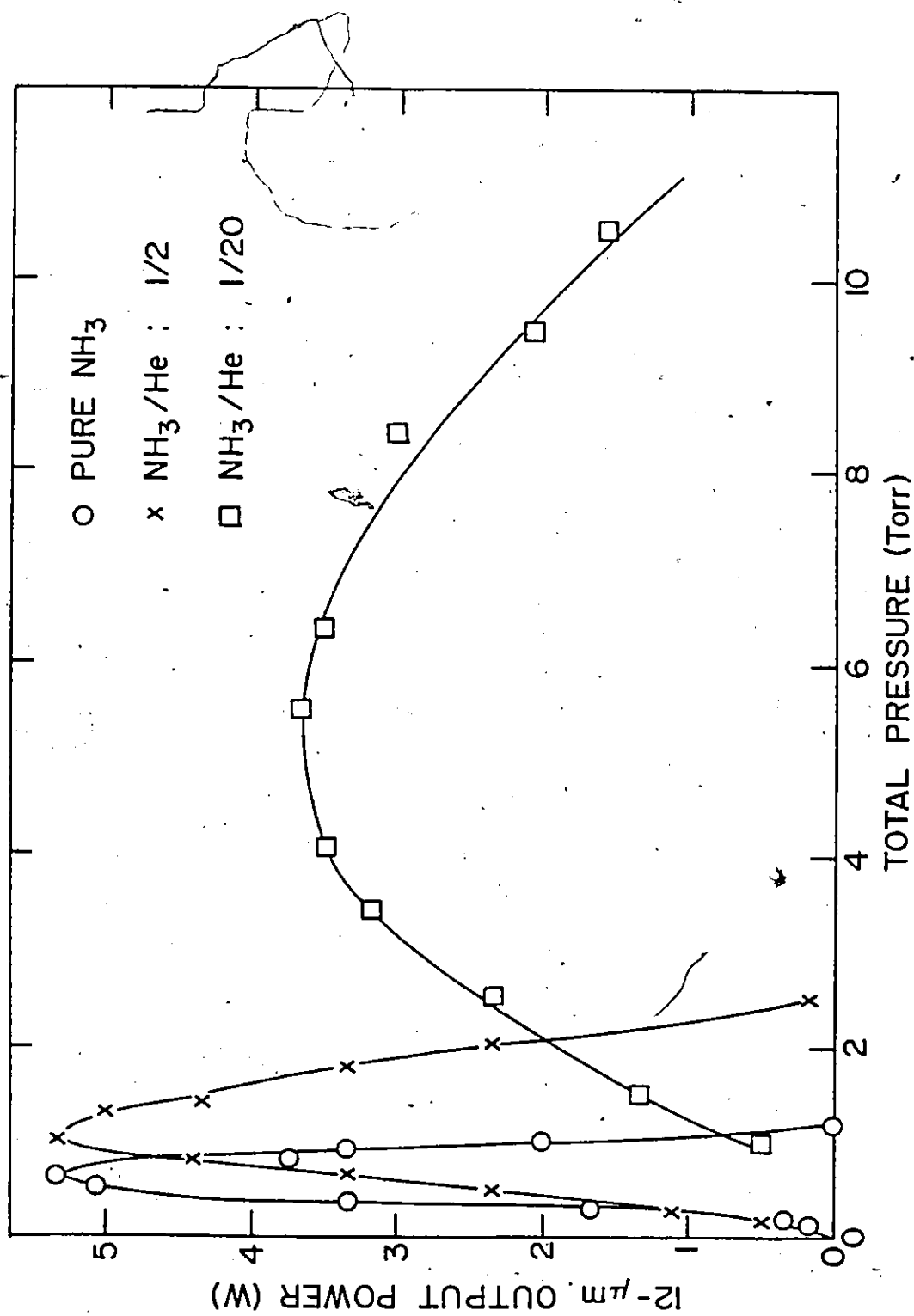


Fig. 5.3: 12- μm output power as a function of the total gas pressure.

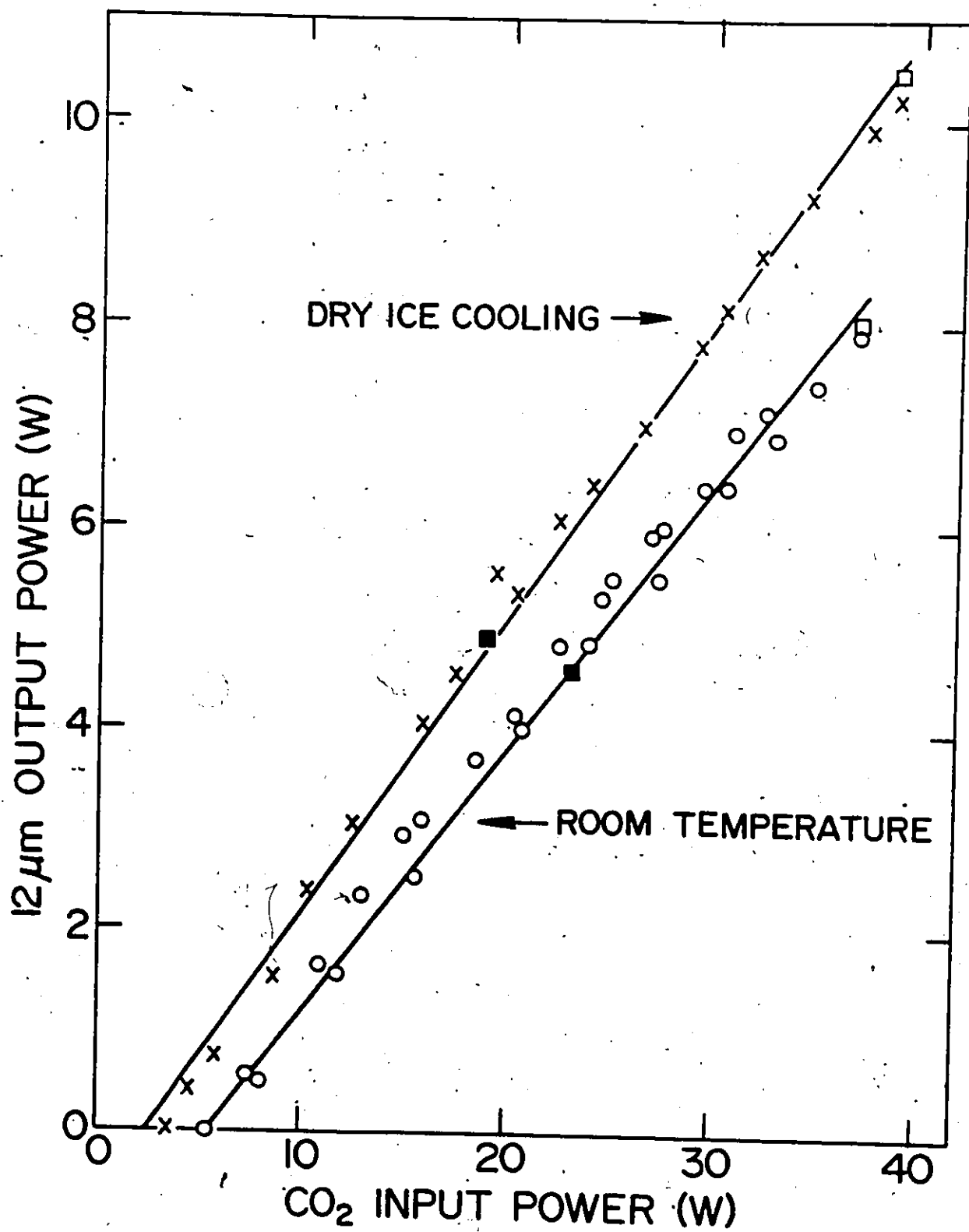
Measurements are shown in pure NH_3 (o) and for NH_3/He mixtures of 1:2 (x) and 1:20 (\square), respectively. The measurements were made in a 60-cm long tube at room temperature with a pump power of 38 W. Note that the maximum 12- μm power does not increase when the NH_3 is diluted with the buffer gas.



5

Fig. 5.4: 12- μ m output power as a function of pump power for a room temperature (o) and with dry ice cooled (x), 1.2 m-long, 2.5-mm bore waveguide cavity. Most of the results were taken with a 1/5th duty cycle chopper. Also shown are measurements with a 1/2 duty cycle (\square) and without a chopper (\blacksquare). The chopped values have been scaled by the duty cycle to give cw values.

1



wire-grid polarizer. However, in selected cases, identical results were obtained with a 50% duty cycle chopper, and with the chopper removed. All the results shown in Fig. 5.4 have been corrected to account for the small measured losses caused by two reflections from the dichroic mirrors. As expected, the 12- μm radiation emerges with circular polarization and propagates like a Gaussian TEM_{00} mode*. Note that 3.8 W of CO_2 pump power were required to reach threshold in the cooled tube. This value agrees reasonably well with small-signal gain calculations based on our computer model (average amplification of 43%/round trip) and the estimated cavity losses ($\sim 38\%$ /round trip). Once above threshold, the 12- μm output power increases linearly with input power, reaching 10.5 W for 38 W of input power. No signs of saturation with pump intensity are observed, suggesting that much higher 12- μm output powers can be attained with a more powerful pump.

There are several ways to calculate the efficiency of the present system. From a practical point of view, the power conversion efficiency is very important and has its highest value of 28% with 38 W of input power in the cooled tube. However, the photon or quantum efficiency is a more fundamental parameter. Only 30 W of the 9- μm radiation actually enters the NH_3 gas, the remainder is reflected from the input mirror and the AR coated ZnSe. The 30 W of pump can convert

* Other mode structures were observed (e.g. annular-shaped mode) depending on the waveguide alignment. Nevertheless, maximum 12- μm output powers were generally measured in a Gaussian-like mode which is close to the far-field diffraction pattern of a EH_{11} mode (known to have the lowest waveguide propagation losses [68]).

into a maximum of 23 W of 12- μm radiation. 10.5 W of 12- μm output is measured corresponding to a quantum efficiency of 45%. This 10.5 W laser represents the maximum known output power, quantum efficiency, and power efficiency of any optically pumped cw infrared laser. With the view to improving the laser performance further, it is appropriate to consider the loss mechanisms in the laser cavity. Of the 30 W of pump radiation coupled into the waveguide, a total of 10 W is estimated to be absorbed by the NH_3 and the waveguide walls or emerges from the cavity under lasing conditions. The remaining 20 W of pump radiation is converted into 15 W of 12- μm radiation. 10.5 W of 12- μm power is coupled out, while window, coupling and waveguide losses, plus reabsorption in NH_3 account for the additional losses. Thus, the laser efficiency can certainly be increased by reducing waveguide losses and using internal mirrors [65].

The ultimate performance of the 12- μm laser strongly depends upon the exact saturation mechanism responsible for the reduction of the small-signal gain to a value which satisfies the cavity threshold condition (gain equals loss). In our laser system, there exist two competing saturation processes: (1) depletion of the pump by the conversion of 9- μm photons to 12- μm photons and (2) population transfer from the $s(5,0)$ level to the $s(7,0)$ level in the NH_3 ground state and the consequent reduction of the Raman gain. By measuring the 9- μm transmission through the waveguide, we found that *under lasing conditions* the average 9- μm intensity could be as much as five times the pump intensity required to achieve threshold. This result indicates that pump depletion is not the dominant mechanism leading to the reduction

of the 12- μm gain [69] and that significant population transfer must occur in the NH_3 ground state. Experiments using an oscillator-amplifier arrangement have confirmed these observations and the results are presented in the next chapter.

5.3 Extension to Other NH_3 Transitions

The work described in this chapter has mainly concentrated on the development and characterization of an efficient 12.08 μm cw laser. However, the same pumping geometry can be utilized to produce cw lasing on other NH_3 lines, in particular those listed in Table 3.1. To examine the possibility of line tunability, the CO_2 laser was tuned to the R(16) 9- μm band transition. The R(16) line center is offset from the nearest NH_3 transition aP(8,0) by 1.36 GHz. This large pump offset frequency was selected to determine the maximum pump offset frequency which would still produce cw lasing. Table 3.1 shows that the threshold pumping power of the aP(8,0) line is ~ 30 times larger than for sP(7,0). The lowest threshold measured for sP(7,0) in section 5.2 was 3.8 W and clearly our 40 W cw CO_2 laser would not provide enough pumping power to produce cw lasing on the aP(8,0) line in the present cavity. Consequently, the optics of the 12- μm linear cavity were modified to minimize the cavity losses by changing the 28% output coupler to a total reflector. A dichroic mirror was placed before the 12- μm input mirror to allow detection of the 12- μm output. With lower cavity losses, the threshold on sP(7,0) was reduced to only 1 W and by tuning the CO_2 laser to the R(16) 9- μm line, cw lasing was observed for the first time on the aP(8,0) NH_3 transition.

This new laser line operates near threshold as only 33 W of pumping power was available. This threshold value is consistent with the measurements shown in Table 3.1.

The observation of cw lasing on this new line demonstrates that the pumping scheme is not limited to the $sP(7,0)$ line and can be extended to other transitions. In addition, the threshold behavior of the $aP(8,0)$ line gives an approximate upper limit on the pump offset frequency under which cw lasing should be feasible (given reasonable pumping powers). Frank *et al.* [70] have reported more than one hundred NH_3 transitions within 500 MHz of a pump laser line and cw MIR operation can be expected on many of these lines in the future.

5.4 Summary

This chapter described the design and performance of a 10.5 W cw 12- μ m Raman laser. In addition, experiments on pumping the $aP(8,0)$ line have demonstrated the feasibility of cw operation with pump offset frequencies as large as 1.4 GHz. The major improvement of our present cavity design over that used in previous work consists in confining the pump radiation in a small bore tube to produce high pumping intensity and consequently high Raman gain. Energy and quantum conversion efficiencies of 28% and 45% respectively, were achieved in our optimum resonator, the highest yet reported for an optically-pumped cw laser in the infrared. Our laser system appears scalable to even higher powers as indicated by our measurements of the 12- μ m output power versus pumping intensity. However, an understanding of the gain saturation mechanism is necessary before one can predict the conditions

needed to increase the 12- μm conversion efficiency. In the next chapter, quantitative measurements are performed using an amplifier-oscillator arrangement to determine the relative importance of the different saturation processes involved in 12- μm Raman lasers.

CHAPTER 6

GAIN SATURATION IN CW 12- μm NH_3 RAMAN LASERS

6.1 Introduction

In the previous chapter, optical pumping of NH_3 was demonstrated to be a very efficient technique for generating powerful cw oscillation in the mid-infrared region. CW powers in excess of 10 W with energy conversion efficiencies of 28% were attained at 12.08 μm using a simple, linear pumping geometry. The high efficiency achieved in the 12.08- μm laser is partly due to the Raman nature of the lasing process but further development of this type of system towards even higher output powers and efficiencies requires a detailed understanding of the exact gain saturation mechanism. In Chapter 4, we have reported the measurement of the dependence of the Raman *small-signal* gain (g_0) on pump intensity, pump offset, pressure, etc... and compared the results successfully with the theory of one intense and one weak laser field interacting with a three-level system. However, there exists no equivalent experimental study in the case of intense fields at both 9 μm and 12 μm .

This chapter presents a study of the gain saturation of the $\text{SP}(7,0)$ transition using experimental conditions similar to those occurring in high power 12.08- μm waveguide lasers. Gain coefficients at 12- μm are measured in waveguide capillary tubes using a conventional oscillator-amplifier technique. The average intensity of the pump CO_2 laser is $\sim 700 \text{ W/cm}^2$ while 12- μm intensities in the amplifier can be

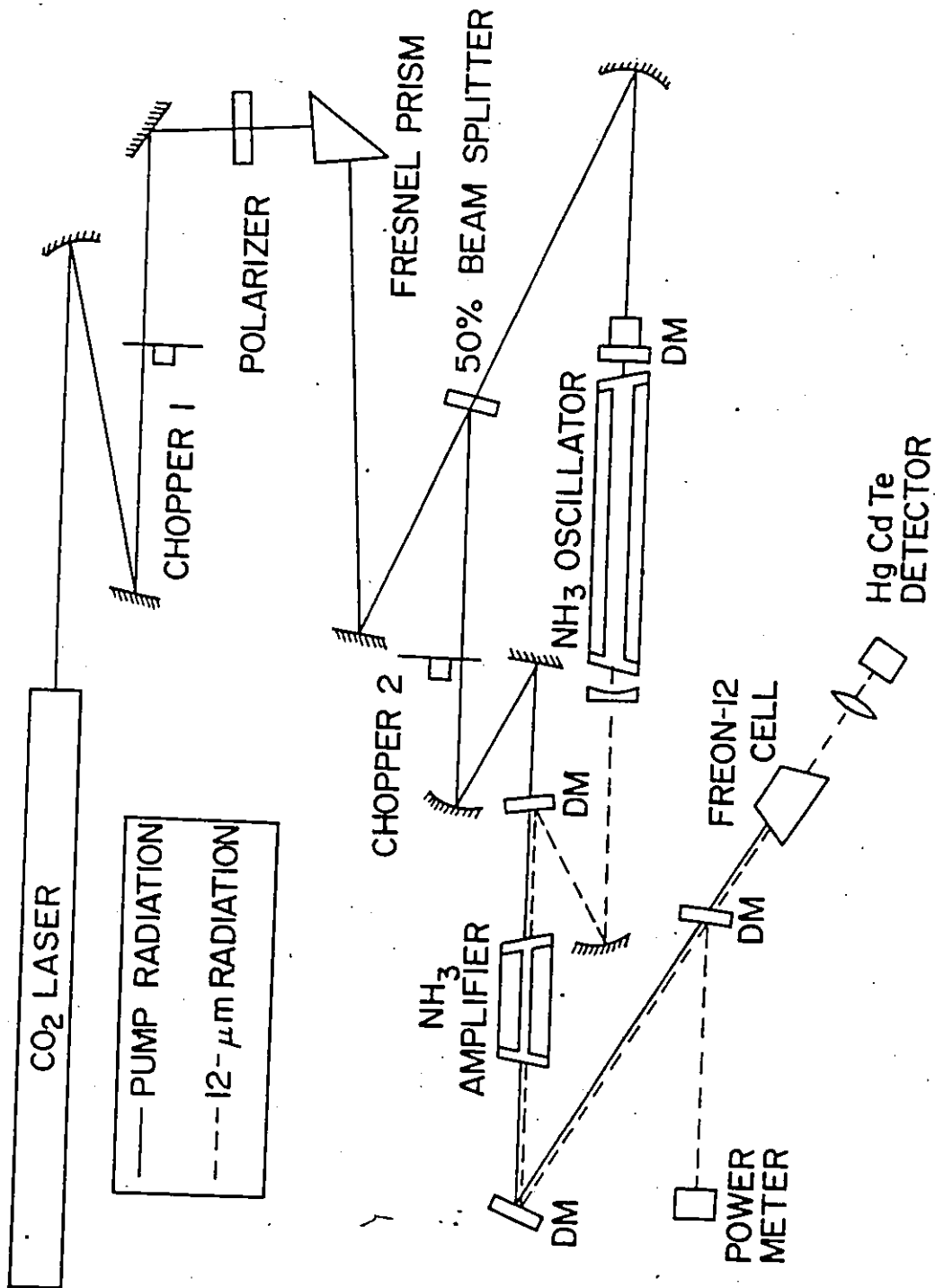
varied from 10 to $\sim 200 \text{ W/cm}^2$. Gain saturation is studied as a function of NH_3 pressure from 0 to 1 Torr, and results are compared with model calculations based on the theory described in Chapter 2.

Studies of optically-pumped cw FIR lasers have reported gain saturation only for resonantly-pumped laser lines [60]. The experiments described in this chapter demonstrate for the first time the presence of strong gain saturation for an optically-pumped cw Raman transition. In addition to providing a test for the theory of a three-level system interacting with two strong laser fields, the measurements of section 6.3 show that the mechanism mainly responsible for the gain reduction is population transfer in the NH_3 ground state rather than pump depletion [69]. This result explains the observed saturation behaviour of 12- μm Raman lasers; in particular the fact that incavity pump intensities are much higher during lasing than at threshold.

6.2 Experimental Apparatus

Figure 6.1 is a schematic diagram of the oscillator-amplifier apparatus. The arrangement is similar to the apparatus used in Chapter 4 to make the small-signal gain measurements (see Fig. 4.2). The major difference between the two pieces of apparatus is in the substitution of the TDL by a high power 12.08- μm laser as the probe. Isolation of the CO_2 pump laser from the 12- μm cavity is accomplished using a linear polarizer and Fresnel prism as discussed in Section 5.2. The CO_2 radiation is divided into two separate beams at a beam splitter; one beam pumps the 12- μm probe laser while the other is focused into an amplifier cell. This arrangement avoids the complexity

Fig. 6.1: Schematic diagram of the apparatus used to measure saturation of the 12.08- μm Raman gain. The dichroic mirrors (DM) transmit 90% of the 9- μm pump radiation, and reflect 97% of the 12.08- μm radiation.



of adding a second CO_2 laser [60], but reduces the maximum power in each pump beam to 16 W. The 12- μm waveguide laser consisted of a 60-cm long, 2.5-mm bore tube and the detailed laser design was described in Chapter 5. A maximum 12- μm output power of 3.5 W is produced by the oscillator and the 12- μm radiation is combined with the second pump beam using a dichroic mirror before entering the NH_3 amplifier.

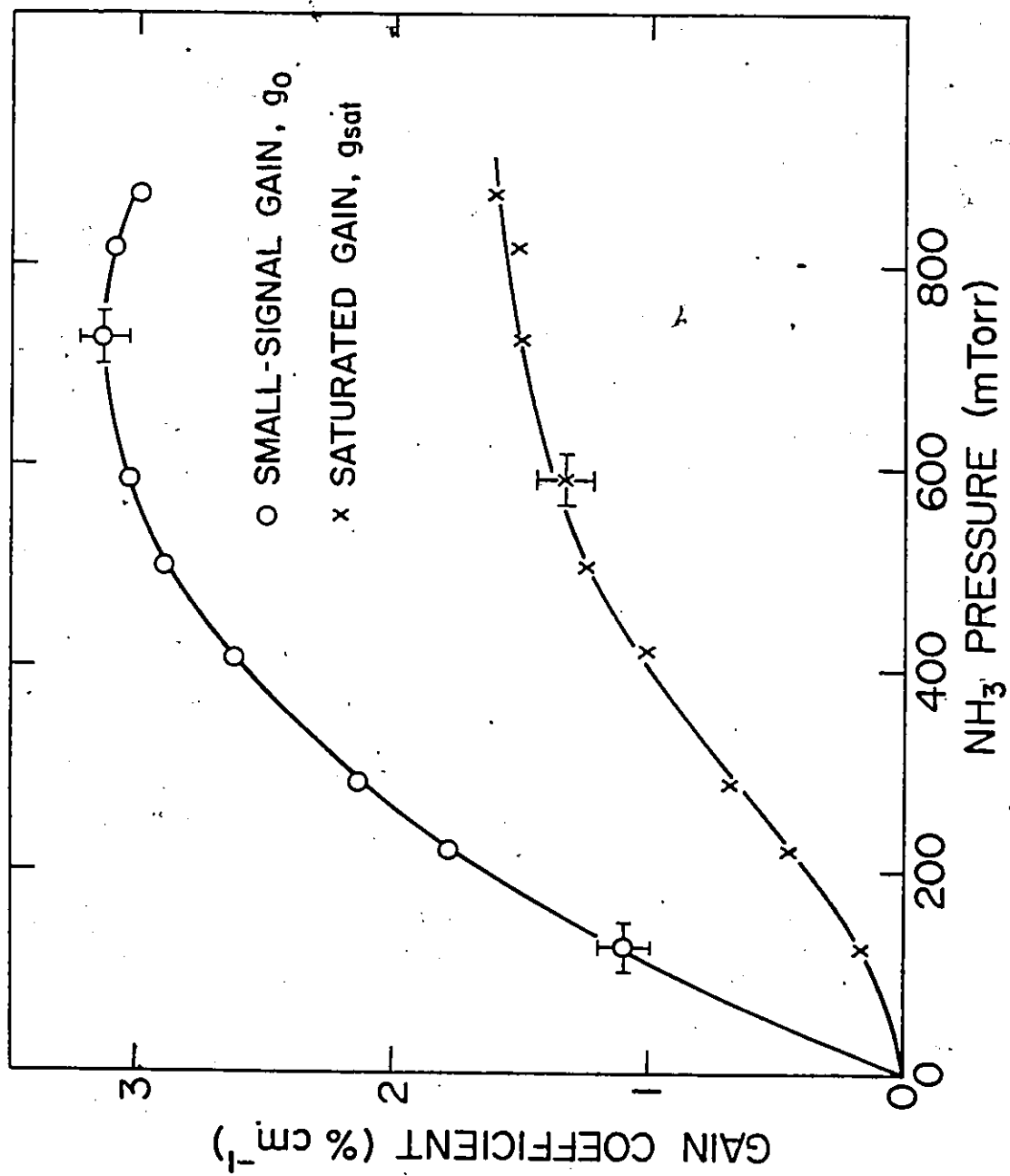
Two choppers are employed in the apparatus. Chopper 1 (duty cycle = 1/5th) reduces the average power incident upon the optics and generates a chopped 12- μm probe beam. The second chopper (chopper 2) acts on the CO_2 pump beam entering the amplifier, and results in the probe beam being alternately transmitted through the amplifier with and without amplification. This arrangement enables the HgCdTe detector to monitor simultaneously the initial (I_0) and amplified ($I = I_0 \exp(\alpha L)$) 12- μm signal. The chopped waveforms are displayed on an oscilloscope and amplification of $\geq 10\%$ in a single pass can be measured with reasonable accuracy ($\pm 0.5\%$ per pass). Note that this measurement technique is sensitive only to changes in the probe transmission and gives the Raman contribution to the gain. The gain measurements are performed by tuning the probe laser to give peak power (generally the most stable point) and using calibrated attenuators to vary the 12- μm power incident upon the amplifier from small-signal to saturated conditions. The experimental arrangement shown in Fig. 6.1 also allows easy measurements of the 9- and 12- μm powers transmitted through the amplifier.

6.3 Results

As one of the main objectives of this study was to elucidate the mechanism responsible for the saturation behaviour in high power waveguide 12- μm lasers, the first amplifier experiments were performed in a 56-cm long, 1.5-mm bore capillary tube. This tube has a length typical of waveguide lasers, while the 1.5-mm bore (instead of the 2.5 mm used in 12- μm waveguide lasers) is intended to maximize the 9- μm and 12- μm intensities*. Figure 6.2 shows the measured gain coefficient as a function of NH_3 pressure. The average pump intensity is $\sim 500 \text{ W/cm}^2$, while the average probe intensity is $\sim 180 \text{ W/cm}^2$ for the saturated gain (g_{sat}) measurements. A detailed analysis of the data of Fig. 6.2 is complicated as both the pump and probe intensities vary substantially along the length of the amplifier. These variations are caused by waveguide losses, NH_3 absorption, pump conversion, and 12- μm amplification. However, the curves of Fig. 6.2 are useful for the design of practical laser systems, and the results demonstrate the importance of population transfer as a saturation mechanism. For example, let us consider the measurements taken at 500 mTorr, a typical operating pressure for NH_3 Raman lasers. We find experimentally that conversion of 9- μm to 12- μm photons reduces the average pump intensity by $\sim 25\%$ in changing from small-signal to maximum 12- μm probe power. As Raman gain is proportional to pump intensity, and power broadening and ac Stark shifts are negligible under our experimental intensities, one

*The smaller waveguide diameter compensates for the reduction in the available 9- and 12- μm powers caused by splitting the pump beam in two.

Fig. 6.2: Experimental measurements of Raman gain coefficients at 12 μm . Measurements were made as a function of NH_3 pressure in a 56-cm long, 1.5-mm bore capillary tube. The incident CO_2 power in the waveguide was 14 W, and the 12- μm probe signal was varied from 3.2 W (saturated gain) to <10 mW (small-signal gain).

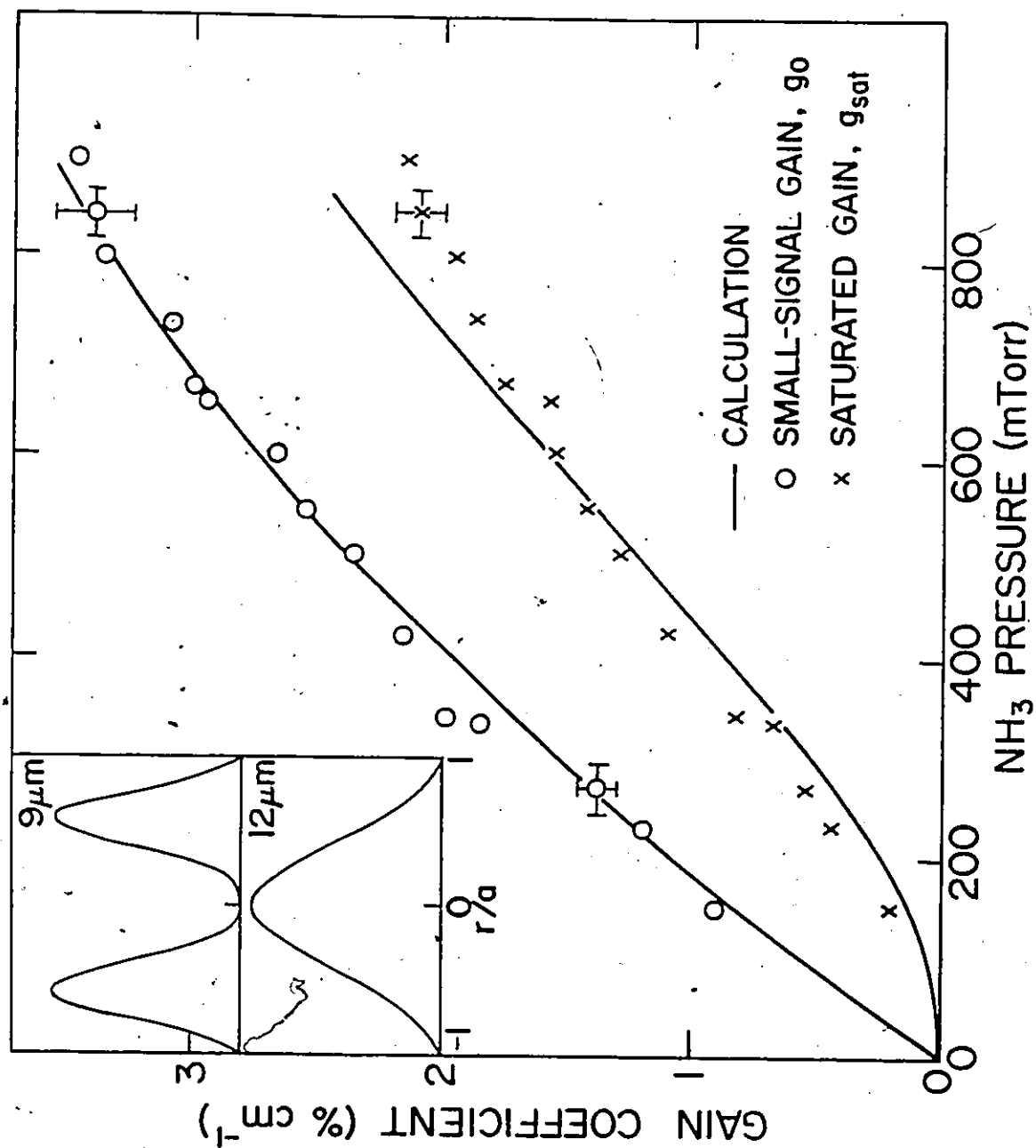


would expect the 12- μm gain to decrease by only 25%, provided there are no significant changes in molecular populations. However, the measured 12- μm gain coefficient is reduced by a factor of 2.4, indicating a substantial change in the population difference which provides the Raman gain.

To separate the effects of population transfer from those of pump depletion, the amplifier length was shortened to 10 cm (a compromise between longitudinal intensity variations and small amplification per pass). The results of experiments with the shorter tube are shown in Fig. 6.3. For these measurements, pump conversion was not significant (<5%) and the pump and probe intensities remained relatively constant along the amplifier length. In comparing Figs. 6.2 and 6.3, one notes a greater degree of saturation in the longer tube, particularly at higher pressures. This difference is primarily caused by pump conversion in the longer tube, with a consequent loss of pump intensity and gain in the latter portion of the amplifier.

To explain the saturation measurements, the model outlined in Chapter 2 was employed. This theory treats the various M sublevels as independent and uncoupled while the use of circularly polarized light induces $\Delta M = \pm 1$ transitions. The inclusion of M -changing populations would substantially complicate the calculations [71] and for simplicity, we continued to use the model described in Chapter 2 as it accounts for our experimental observations. Preliminary calculations were carried out using our computer code to determine the effect of varying the relaxation rate γ ($\gamma = \gamma_1 = \gamma_2 = \gamma_{12}$) in Table 2.1, since this rate is not well known. As discussed in section 2.4.2, g_0 is rather

Fig. 6.3: Experimental and calculated values of Raman gain coefficients in a 10-cm long, 1.5-mm bore capillary tube. Pump and probe powers incident in the waveguide are 14 W and 2.7 W respectively. Calculated values are given for the relaxation rate $\gamma = 25 \times 10^6 \text{ s}^{-1} \text{ Torr}^{-1}$ and use the radial intensity distributions (normalized to the waveguide radius a) given in the inserts. The calculated values are scaled by a factor of 0.5 (see text).



insensitive to the value of the relaxation rates but the degree of gain saturation is strongly dependent upon the relaxation rates of the (5,0) and (7,0) levels in the ground state of NH_3 . These model results have a simple physical explanation. In the presence of a strong pump field and a weak 12- μm field, there is very little population transfer because of the off-resonance nature of the pump field. Consequently, the Raman gain is determined primarily by the initial populations and matrix elements, and population relaxation is not important. However, if both pump and 12- μm fields are intense, significant conversion from 9 μm to 12 μm occurs, with a simultaneous transfer of population from the (5,0) to the (7,0) level. Collision relaxations from the (7,0) level to the (5,0) level now limits the recovery of the gain. Fast relaxation rates will keep the population of the perturbed levels near their thermal value and the gain will be difficult to saturate. In the case of fast relaxation rates, the pump power will be depleted before the 12- μm intensity reaches the saturation intensity*. For low γ values, small 12- μm intensities are required to decrease the 12- μm gain and the pump power is not substantially depleted by the passage of the 12- μm probe beam.

Before any accurate comparisons can be made between experiment and theory, one must consider the degree of spatial overlap between the pump and probe fields in the amplifier. The relative alignment of the two beams makes a substantial difference to the measured gain

*The saturation intensity is defined as the intensity at which the small-signal gain is reduced by a factor of 2 [72].

coefficient, and hence the spatial distribution of each beam must be included in any calculations. For the purposes of calculation, the waveguide area was divided into 20 annular zones. Pump and probe intensities are estimated for each zone from experimental observations of the spatial intensity variations, and the total gain coefficient is calculated by summing over all the zones. The inserts in Fig. 6.3 give the intensity distributions used in the model. These profiles approximate our experimental conditions (TEM₀₀ mode for the 12- μ m probe and an annular shape for the pump as the high-power cw CO₂ laser generally gave optimum power into an annular-shaped mode). The solid lines in Fig. 6.3 are the best fit to the data obtained by using $\gamma = 25 \times 10^6 \text{ s}^{-1} \text{ Torr}^{-1}$ and including a scaling factor (0.5) on the calculated gain values. This scaling factor is slightly larger than that anticipated from previous absolute measurements with a tunable diode laser (calculations were scaled by 0.65 for circularly polarized beams) but this difference is of the same order as the variation in experimental gain induced by minor changes in alignment*. Note that the overall experimental behaviour in Fig. 6.3 is well reproduced by the theory.

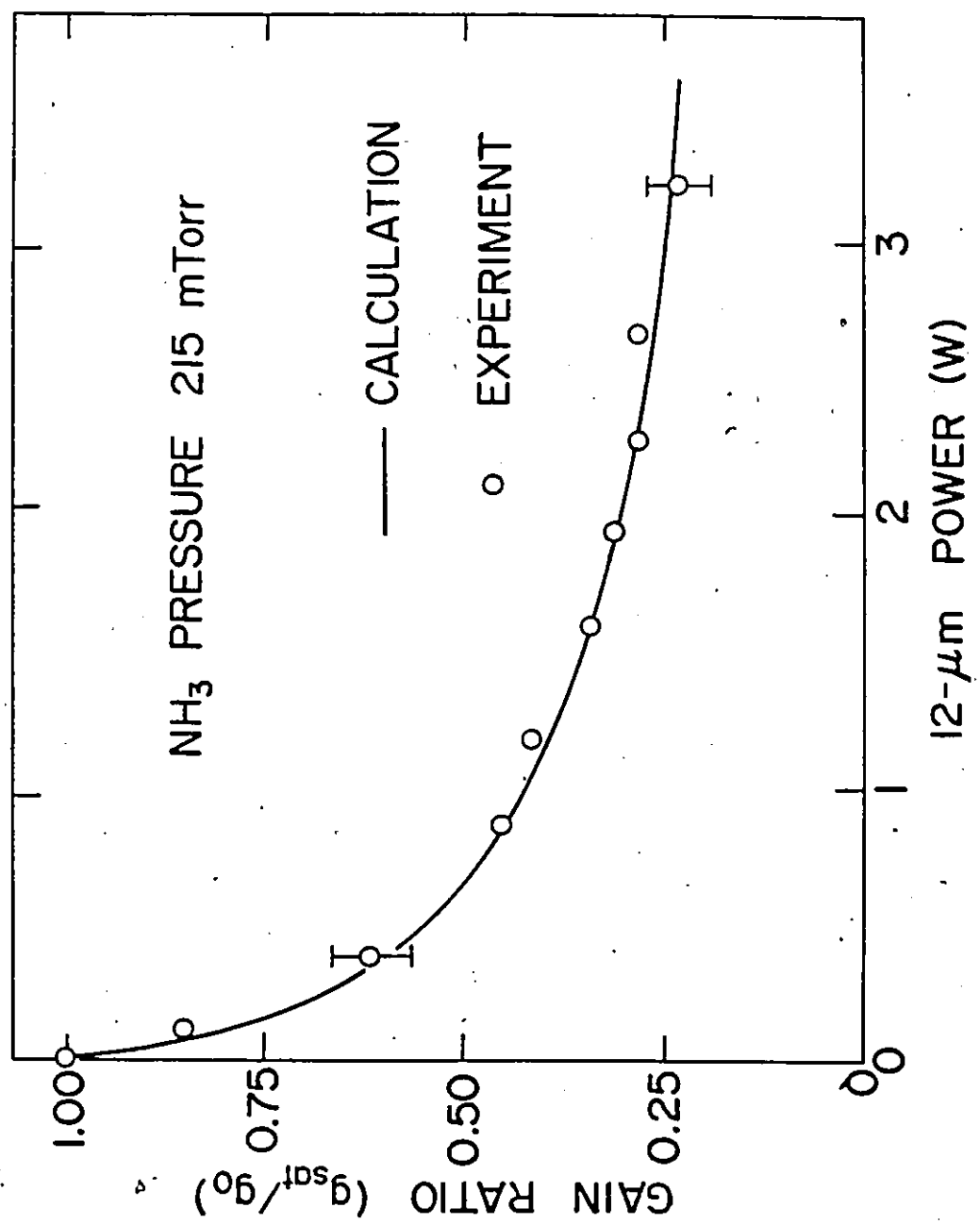
To evaluate the effect of different spatial overlaps of pump and

* The 15-cm long amplifier tube allows a certain degree of misalignment of both the pump and probe beams before the transmitted 9- μ m and 12- μ m powers decrease. Consequently, the degree of overlap between the pump and probe beams within the capillary tube could be varied to produce significant changes in the absolute value of g_0 . On occasion, measured g_0 values were 1.5 times larger than those displayed in Fig. 6.3, but the ratio g_{sat}/g_0 remained relatively constant.

probe beams, calculations were carried out for uniform intensity distributions across the waveguide, and for two perfectly aligned EH_{11} modes. In each case the same total power propagated through the waveguide (14 W at 9 μm and 2.7 W at 12 μm for saturation), and the same relaxation rates as for Fig. 6.3 were employed. At 500 mTorr NH_3 , the case of uniform intensities gives a ratio g_{sat}/g_0 of 0.64 while the overlapping EH_{11} modes produces a ratio of 0.32. For comparison, the spatial distributions shown in Fig. 6.3 gave $g_{\text{sat}}/g_0 = 0.5$ at 500 mTorr. These numerical examples demonstrate the importance of the transverse intensity profile, and also indicate the extent to which the best-fit relaxation rate is dependent upon the spatial distribution used in the model.

The influence of the spatial overlap on the saturation process can be understood by recognizing that the rate of molecular transfer from the (5,0) level to the (7,0) level is proportional to the product of the 12- and 9- μm intensities. Accordingly, two overlapping EH_{11} distributions display a larger gain saturation than two spatially uniform intensity distributions. To confirm the intensity dependence of g_{sat} the 12- μm power incident on the amplifier was varied. The results are plotted in Fig. 6.4. The experiment was performed at low NH_3 pressure (215 mTorr) to provide a large dynamic range between g_{sat} and g_0 , while the 56-cm long waveguide was utilized for accurate gain measurements. Depletion of the 9- μm pump was negligible at this pressure. The solid line was calculated using the same input data and overlapping spatial functions as in Fig. 6.3. Good agreement is found between theory and experiment. Note that at this pressure only 0.7 W

Fig. 6.4: Ratio of saturated gain to small-signal gain, g_{sat}/g_0 as a function of incident 12- μm power. Measurements are made in the 56-cm long, 1.5-mm bore waveguide with 14 W of 9- μm pump power. Calculations are carried out using the same spatial intensity distributions and relaxation rates as those utilized for Fig. 6.3.

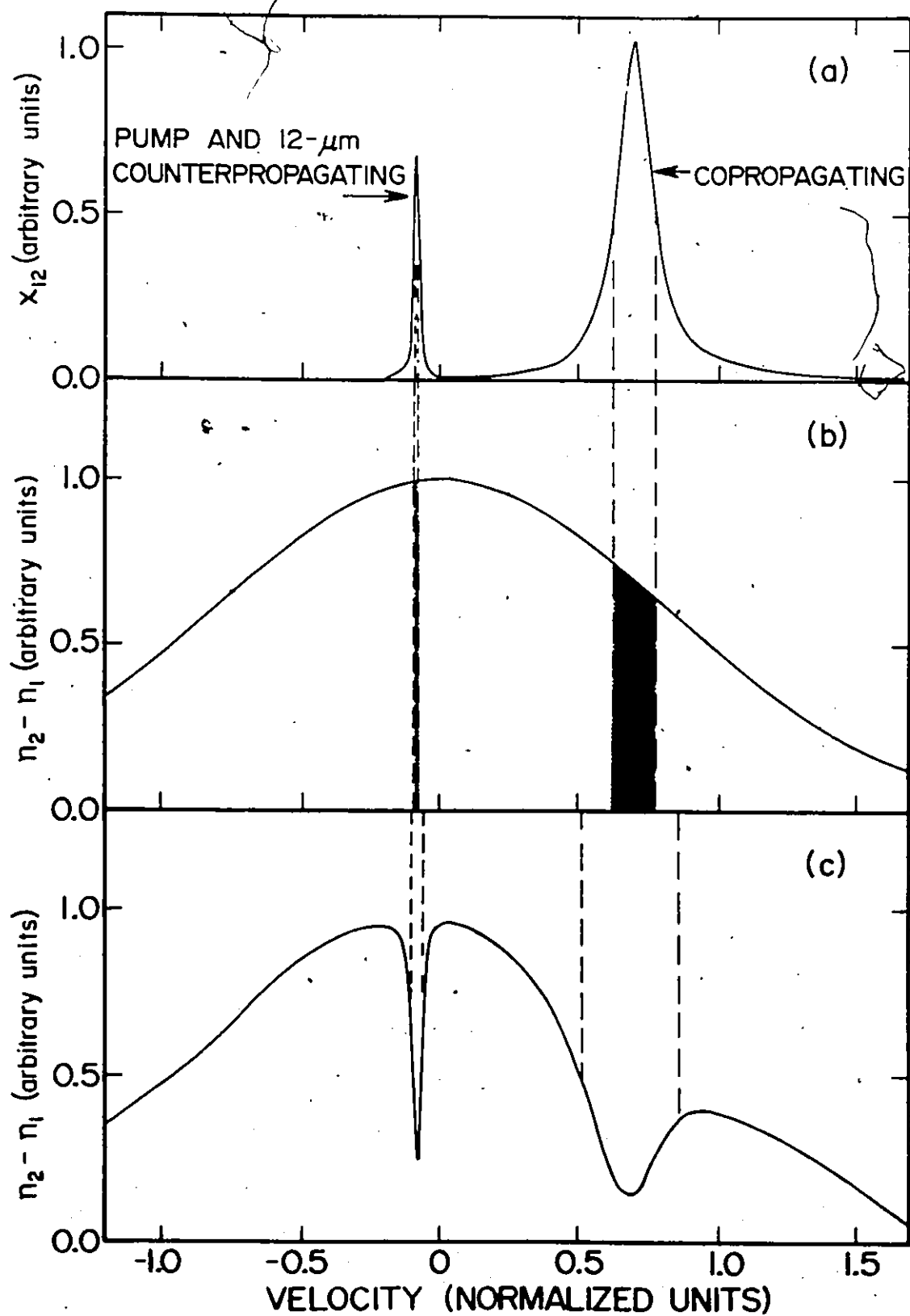


of 12- μm power is sufficient to reduce the gain to half its initial value. In addition to the measurements of g_{sat} as a function of 12- μm power, we have verified that the ratio g_{sat}/g_0 increased as the 9- μm pump power was reduced, thereby confirming the proportionality of the saturation process to the product of the 9- and 12- μm intensities.

While the measurements described above clearly demonstrate the importance of population transfer in the NH_3 ground state, the complexities associated with the spatial intensity distributions and circularly polarized radiation make it difficult to determine a precise value for γ . The fitted value of $25 \times 10^6 \text{ s}^{-1} \text{ Torr}^{-1}$ is somewhat slower than the value of $93 \times 10^6 \text{ s}^{-1} \text{ Torr}^{-1}$ used previously for small-signal gain calculations but is probably closer to the population relaxation rate occurring in $K=0$ levels. Such levels have no inversion splitting and thus the dominant mechanism for state changing collisions is $\Delta J=1$ collisions [27]. The relaxation rate for $\Delta J=1$ collisions is expected to be 5 to 10 times slower than the rate for collisions which simply change the state of inversion [73] and thus an effective relaxation rate of $25 \times 10^6 \text{ s}^{-1} \text{ Torr}^{-1}$ seems reasonable.

It is instructive to examine the predictions of the theoretical model in more detail to gain a better understanding of the saturation process. Although the Raman linewidth for copropagating beams is substantially narrower than the Doppler width, the resultant gain profile is still inhomogeneously broadened at our working pressures ($<1 \text{ Torr}$). The effect of a saturating 12- μm field is to burn holes in the molecular velocity distribution. These holes are very different for co- and counter-propagating beams, as illustrated in Fig. 6.5 for the $M=1$

Fig. 6.5: Velocity hole burning in the $M=1$ sublevel of NH_3 . Calculations are performed for a $9\text{-}\mu\text{m}$ intensity of 700 W/cm^2 pumping 200 mTorr of NH_3 at a frequency offset of 190 MHz from the $\text{sr}(5,0)$ line. The middle curve 5(b) gives the unperturbed population difference between levels (5,0) and (7,0) in the NH_3 ground state ($n_2 - n_1$). Velocities on the x-axis are normalized to the most probable velocity divided by $(n_2)^{1/2}$. The upper curves 5(a) show the two-photon contribution to the $12\text{-}\mu\text{m}$ small-signal Raman gain at an offset of 185 MHz. This Raman susceptibility (χ_{12}) is plotted as a function of molecular velocity for both co- and counter-propagating beam. Curve 5(c) illustrates the population hole-burning which occurs when a $12\text{-}\mu\text{m}$ beam of intensity 50 W/cm^2 is applied at an offset of 185 MHz from the $\text{sp}(7,0)$ line. The dashed lines indicate full-width-half-maximum linewidths.



sublevel. The small-signal Raman gain is proportional to the product of the molecular susceptibility (χ_{12} in Fig. 6.5(a)) and the population difference ($n_2 - n_1$) (see Fig. 6.5(b)). The velocity classes contributing to the small-signal gain are indicated by the shaded area of Fig. 6.5(b). The influence of an intense 12- μm field is illustrated in Fig. 6.5(c). Hole burning now appears in the population profile, and the gain saturates. The 12- μm field is intense enough to cause power broadening, as indicated by the dashed lines delineating the full width at half maximum in Fig. 6.5. Calculations similar to those used to produce Fig. 6.5 must be carried out for all the M sublevels, and the contributions added to obtain the total Raman gain. As mentioned earlier, the M-levels are assumed to be uncoupled and no account is taken of the complexities introduced by using circularly polarized radiation.

6.4 Discussion and Conclusions

This chapter described the first experimental study of gain saturation in an optically-pumped cw mid-infrared laser and provided further insight into the saturation mechanisms occurring in Raman lasers. The general behaviour of the gain was found to be in agreement with the theory of a three-level system interacting with two intense radiation fields. Our analysis emphasizes the role played by rotational relaxation in the NH_3 ground state, and shows that this relaxation rate determines the relative importance of population transfer and pump depletion mechanisms for reducing Raman gain in a practical laser. Accurate modelling of 12- μm linear oscillators is further complicated by the fact that the 9- μm and 12- μm fields propagate in both directions

in the waveguide laser. Thus four different combinations of co- and counter-propagating beams must be considered, and the same molecular velocity class can be saturated by more than one combination. In addition, spatial hole burning may occur due to the 9- μm and 12- μm standing wave patterns. Despite these additional complexities, the saturation measurements presented here account for the main features of the saturation behaviour observed in our high power cw 12.08- μm Raman lasers. For example, under lasing conditions, the 8 W laser of Chapter 5 (measured in the 1.2-m tube at room temperature) has an average incavity intensity of 600 W/cm^2 at 12 μm and 400 W/cm^2 at 9 μm . This pump intensity gives a small-signal gain which is ~ 5 times the value required to reach threshold. The simple model used in this chapter predicts that the presence of 600 W/cm^2 at 12 μm in the laser cavity decreases the gain by a factor of 3.3 in reasonable agreement with the observed reduction of ~ 5 , i.e., the model accounts for most of the gain saturation required to attain the steady-state conditions (gain equals cavity loss).

The results of this chapter should aid in improving the design of future 12- μm laser systems, which may advantageously be produced using a ring waveguide laser. More efficient operation of 12- μm Raman lasers will certainly increase the maximum pump offset frequency under which cw lasing can be expected. However, line tunability in a cw Raman MIR laser is still limited by the small number of good coincidences*

*By good coincidence, we mean an R-branch line offset from a reasonable powerful-pump source by a frequency of $< 200 \text{ MHz}$.

between the available pump frequencies and suitable absorbing transitions. The next chapter describes a different approach to produce cw line-tunable radiation. The technique requires pumping on only one NH_3 transition and relies on the transfer of a significant fraction of the ground state population to the $\nu_2=1$ vibrational mode in NH_3 to create gain in the entire P-branch.

CHAPTER 7

LINE-TUNABLE OSCILLATION OF A CW NH_3 LASER

7.1 Introduction

This chapter describes the design and characterization of the first reported line-tunable optically-pumped cw laser operating on vibrational-rotational transitions. CW lasing is obtained on a total of 20 different NH_3 transitions covering the range between 10.7 and 13.3 μm . These results are achieved by using a novel pumping scheme. In all the experiments described so far, the NH_3 transition was pumped off-resonance with a CO_2 laser. Calculations based on our model indicated that even with low pumping powers, very efficient pumping could be realized if the pump frequency is resonant with an absorbing NH_3 transition. Consequently, we decided to downshift the frequency of the R(30) CO_2 9- μm laser by 180 MHz to give an exact coincidence with the sR(5,0) NH_3 absorption line. Line center pumping facilitates the efficient transfer of a significant fraction of the ground state NH_3 population to the $v_2=1$ vibrational level. The addition of N_2 as a buffer gas allows rotational thermalization to take place in both the ground state and excited levels and, under optimum conditions, inversion occurs in the entire P-branch. A simple model based on rapid thermalization of the rotational populations is developed to account for the number of observed NH_3 laser lines. Good qualitative agreement is found between the model predictions and the experiment.

7.2 Theory

The pumping scheme described in this chapter owes its success to the fact that the $\nu_2=1$ vibrational mode in NH_3 can be inverted with respect to its ground state. The concept of partial and complete vibrational-rotational population inversion was initially discussed by Polanyi immediately after the operation of the first lasers [74]. In recent years, Golger and Letokhov [75] and Goela and Morse [76] have proposed that population inversion can be attained by optical resonance pumping of specific vibrational-rotational transitions under conditions ensuring thermal equilibrium of the populations in the rotational sublevels. This optical-pumping technique relies on the fact that, under suitable conditions for vibrational inversion, absorption is present in the R-branch while gain exists in the P-branch, particularly at high values of J . Inversion can be maintained by absorption of photons from a resonant R-branch pump, while lasing can take place in the P-branch. The idea is very attractive since by pumping on a single line, laser emission can be achieved at a large number of different frequencies.

One difficulty in applying the optical-pumping technique is that it works best with light molecules such as HF, CO and NH_3 *. However, these molecules have only a few widely-spaced R-branch transitions which are suitable for optical pumping, and there are no conventional cw pump lasers having exact coincidences with these lines.

* Light molecules have a large value for the rotational constant B which in turn allows high inversion ratio between the population of the two vibrational levels to be attained.

The near resonance existing between the $sR(5,0)$ NH_3 line and $R(30)$ $9\text{-}\mu m$ CO_2 transition is small enough to allow efficient line-tunable operation with high-power pulsed CO_2 laser [77-79], but the offset is too large for the use of conventional cw CO_2 lasers. This difficulty was overcome by downshifting the $R(30)$ pumped line into coincidence with the $sR(5,0)$ NH_3 absorption line. The downshifted radiation is an efficient optical pump of NH_3 and transfers a significant fraction of the ground-state NH_3 population to the $v_2=1$ vibrational level. The gain spectrum resulting from this population redistribution can be easily evaluated using the condition that the rotational populations are always thermalized. A thermalized rotational distribution is expected since with the addition of the buffer gas N_2 , the rotational relaxation rate is very fast relative to the vibrational-translational (V-T) relaxation rate*. Furthermore, as there is no interconversion between ortho- NH_3 ($K=3n$, n an integer) and para- NH_3 ($K=3n \pm 1$) (see the selection rules in section 2.3), only the population of the pumped species, i.e., ortho- NH_3 is included in the calculations. Thus, the gain spectrum is completely determined by the vibrational population distribution of the pumped species.

The model developed to predict the gain distribution assumes that the total population lies in the ground, N_0 and first excited, N_1 state of the v_2 mode. The population in the rotational level i ,

* Under typical conditions for our experiments, the V-T rate is $\sim 2 \times 10^5 \text{ sec}^{-1}$ while the rotational relaxation rate is $\sim 2 \times 10^8 \text{ sec}^{-1}$.

n_i , inside the vibrational level, N_j , is simply equal to

$$n_i = f_i N_j \quad (7.1)$$

where f_i is the rotational partition function given by Townes and Schawlow [25]. The model employs NH_3 spectroscopic constants from refs [42-46] to evaluate the rotational partition function. The gain (or absorption) between levels i and j is calculated using the following expression,

$$\alpha_{ij} = \sigma_{ij} (n_i - n_j (g_i/g_j)) \quad (7.2)$$

where g_i, g_j are the level degeneracies and σ_{ij} the absorption cross-section. σ_{ij} includes the transition dipole moment μ_{ij} and a Voigt profile for the lineshape [40]. The pressure-broadened linewidth, $\Delta\nu_{ij}$ is the sum of two contributions

$$\Delta\nu_{ij} = (\Delta\nu_{ij})_{\text{NH}_3} p_{\text{NH}_3} + (\Delta\nu)_{\text{N}_2} p_{\text{N}_2} \quad (7.3)$$

where the p 's are pressures of NH_3 and of the buffer gas N_2 . Taylor's calculated value is taken for the self-broadened coefficient $(\Delta\nu_{ij})_{\text{NH}_3}$ [41] while a constant pressure broadening parameter of $(\Delta\nu)_{\text{N}_2} = 7$ MHz/Torr (FWHM) is used for the N_2 contribution*.

The equations (7.1) and (7.2) show that the gain spectrum is completely determined by the vibrational populations N_0 and N_1 under the assumption of rotational thermalization. A more convenient way to express the degree of vibrational inversion is to use the ratio

*This parameter does not vary much with the different NH_3 transitions [80].

N_1/N_0 . The value N_1/N_0 specifies the gain (absorption) distribution in the P, Q and R branches. For example, significant gain first appears in the P-branch when $N_1/N_0 \sim 0.7$ while the Q-branch requires $N_1/N_0 \sim 1$ for inversion. The maximum value of N_1/N_0 is attained when the pump absorption becomes completely saturated. Considering the two rotational levels of the pumped transition, n_0 in N_0 and n_1 in N_1 , from eq. (7.2) saturation occurs when

$$n_0 = n_1 (g_0/g_1) \quad (7.4)$$

substituting eq. (7.1) in eq. (7.4) we get

$$\begin{aligned} (N_1/N_0)_{\max} &= (f_0/f_1) (g_1/g_0) \\ &\sim \exp(-E_0/kT) / \exp(-E_1/kT) \end{aligned} \quad (7.5)$$

where E_i is the rotational energy of level n_i . To a first approximation, E_i is equal to $hcB^2(J+1)$ (B is the rotational constant in cm^{-1}). Golger and Letokhov have shown that optimum condition for the inversion gain, i.e., large $(N_1/N_0)_{\max}$, is attained by pumping on a R-transition. Substituting the approximate expression of E_i into eq. (7.5) and assuming that we pump on a R-transition with the quantum number J in the lower level, we obtain

$$(N_1/N_0)_{\max} = \exp(2Bhc(J+1)/kT) \quad (7.6)$$

Clearly, maximum ratio of N_1/N_0 will be obtained for large B values and high- J rotational lines. Large values of $(N_1/N_0)_{\max}$ allow the transfer of a major fraction of the ground state population to the

upper vibrational level and the creation of substantial gain in the different branches. Figure 7.1 displays the calculated gain in the P, Q and R branches for different values of N_1/N_0 . Since there is no interconversion of ortho- and para- NH_3 , only transitions with $K=3n$ are plotted. With no pump present, N_1/N_0 is close to zero and there is a strong absorption on all the NH_3 transitions. When the ratio N_1/N_0 reaches .9, the low J-value transitions of the Q-branch are almost inverted. Finally, the $\text{SR}(5,0)$ ~~absorption~~ line becomes completely saturated for $N_1/N_0 = (N_1/N_0)_{\text{max}} \sim 2$ at which point substantial gain is present in the P, Q and R branches.

The model presented in this section calculated the gain spectrum assuming that the ratio of the total population of the $v_2=1$ level to that of the ground state is known. In practical systems, the degree to which a pumped line is saturated will depend on the pumping intensity available and on the exact dynamics governing the energy transfer among the various vibrational levels. These considerations are addressed in more detail in the next section.

7.3 Experimental Apparatus and Results

The experimental apparatus used to produce line-tunable operation in NH_3 is shown schematically in Fig. 7.2. Two acousto-optic modulators* successively downshift the CO_2 laser frequency by 90 MHz in

* An acousto-optic modulator is a device in which a light beam is scattered by an acoustic wave (Brillouin scattering). Most efficient diffraction of the optical wave in a practical device is obtained when the beam is incident near the Bragg angle in which case the magnitude of the photon wave vector is changed very little. From the conservation of energy, the frequency of the diffracted beam will be changed by an amount equal to the acoustic wave frequency.

Fig. 7.1: Calculations of gain versus wavelength for different N_1/N_0 ratio. The gain is calculated for a 1% NH_3/N_2 mixture at 8 Torr. The calculations are carried out for the $K=0$ lines in the R-branch, $J=K=3$ in the Q-branch and $K=0$ in the P-branch. The pumped transition is marked with an asterisk (*). Note that the absorption on the pumped line goes to zero when $N_1/N_0=2$.

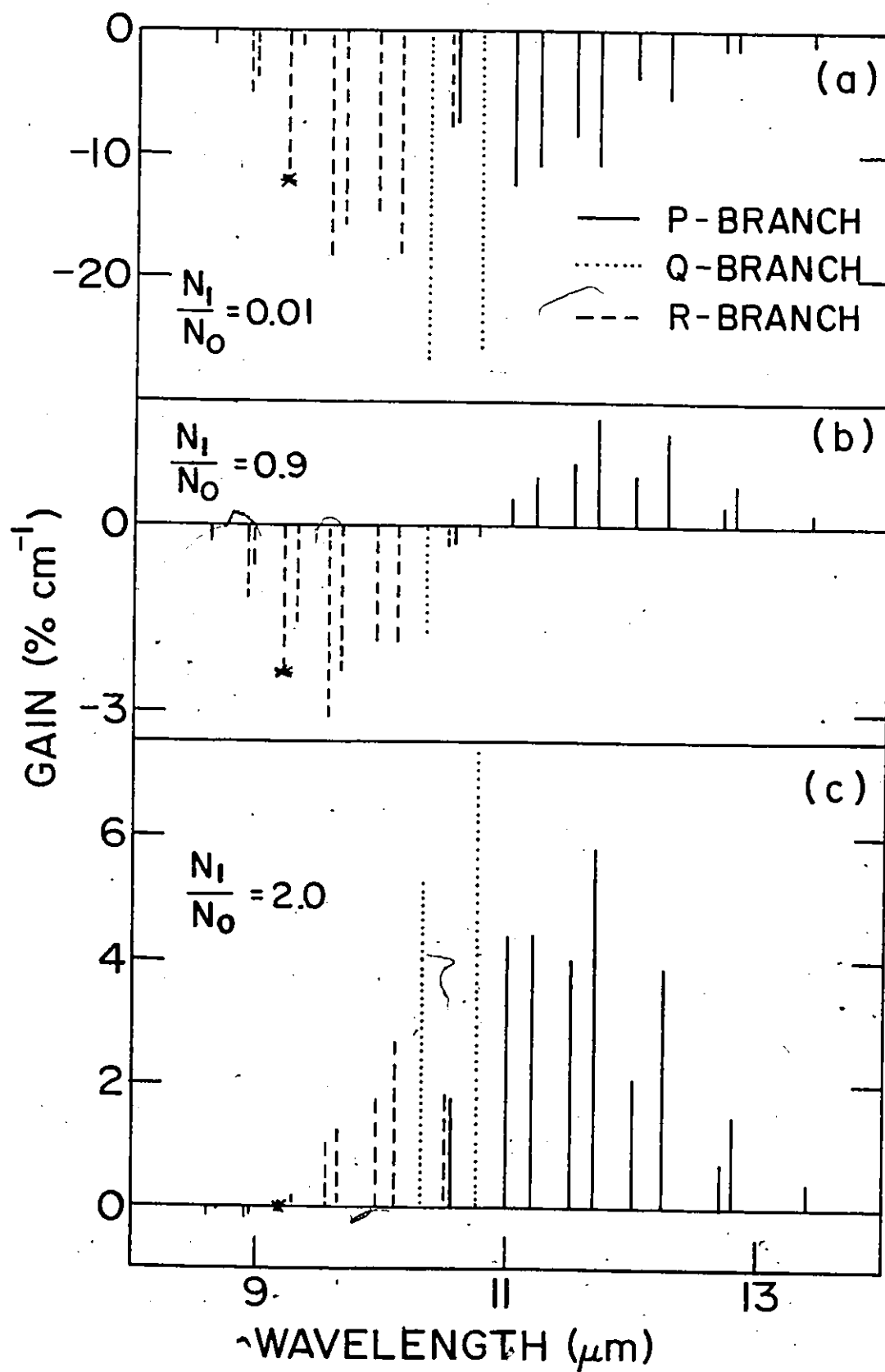
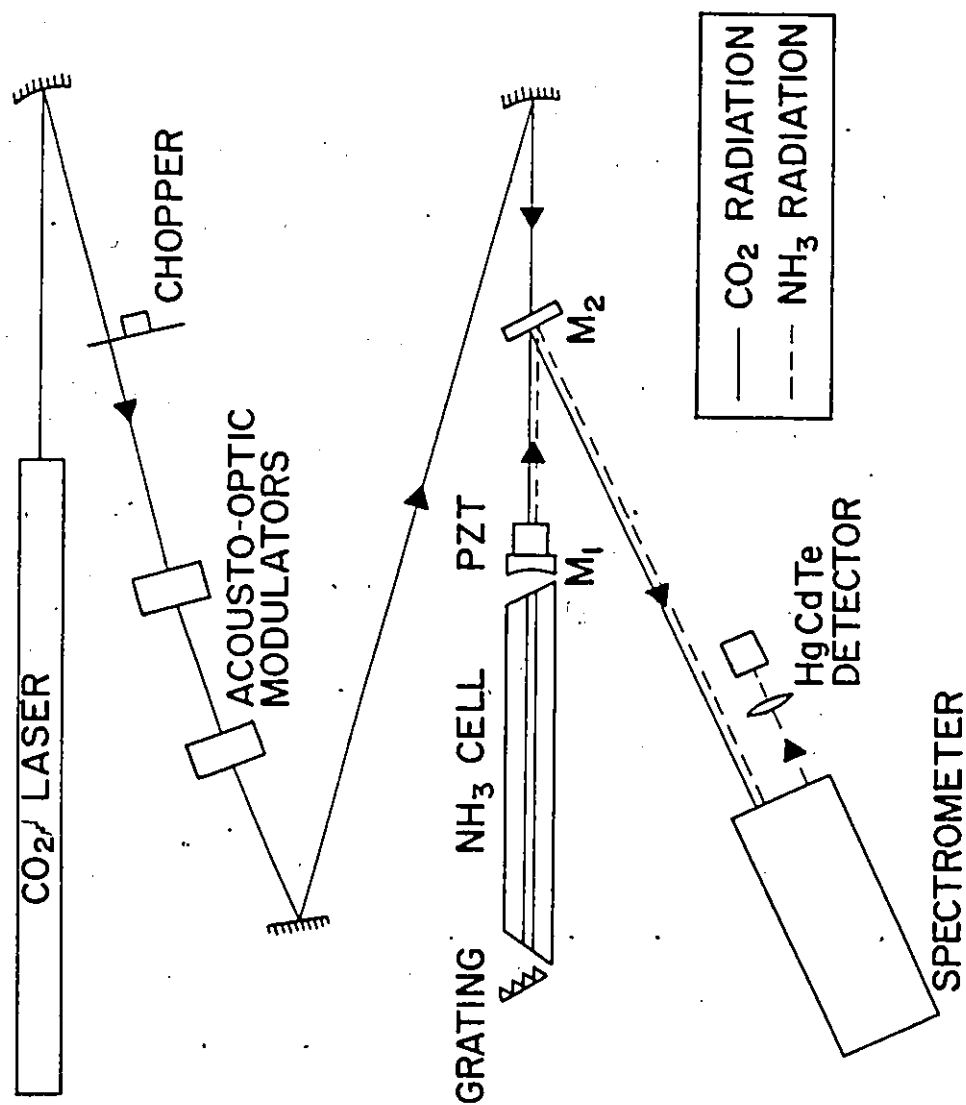


Fig. 7.2: Schematic diagram of the apparatus used to produce line-tunable cw operation in NH_3 between 10.7 and 13.3 μm in the selective cavity. Mirrors M_1 and M_2 transmit 90% of the 9- μm CO_2 radiation, and have $\sim 98\%$ reflectivity between 11.2 and 13.5 μm .



each modulator. Approximately 9 W of radiation emerges from the modulators downshifted by 180 MHz. The CO_2 pump frequency is now in resonance with the $\text{sR}(5,0)$ NH_3 line. The pump radiation passes through two dichroic mirrors M_1 and M_2 (the same as in Chapter 4), before being focused into a 1.5-mm bore, 57-cm long pyrex capillary tube. The use of a waveguide is once more crucial to our pumping scheme. The waveguide resonator allows high pumping intensities to be produced from our relatively modest CO_2 pumping powers. A 12- μm grating selects the lasing wavelength and a 0.5-m monochromator is used to determine the lasing frequency to $\pm 0.08 \text{ cm}^{-1}$. A simple linear pumping arrangement can be utilized since the feedback problems obtained from the reflection of the pump radiation back into the CO_2 laser are eliminated by the use of the modulators. The isolation of the two cavities functions as follow: the CO_2 power reflected from M_1 goes through the modulators for a second time and gets downshifted by another 180 MHz. The CO_2 laser is not perturbed by the different frequency of the feedback beam. Initial results were taken with an external chopper (duty cycle 1/5) in the CO_2 beam to avoid the possibility of optical damage to the modulators or M_1 ; later work gave identical results with true cw operation.

Table 7.1 lists the observed wavelengths and the relative power on each line in the selective cavity. A 1% NH_3 in N_2 mixture was used, at a total pressure of 8 Torr. The model described in section 7.2 was used to account for the distribution of the observed NH_3 laser lines. Figure 7.3 displays the calculated gain in the P, Q, and R branches for $N_1/N_0 = 1.1$. This ratio best fits the results in

Table 7.1

Observed cw NH_3 Laser Lines.

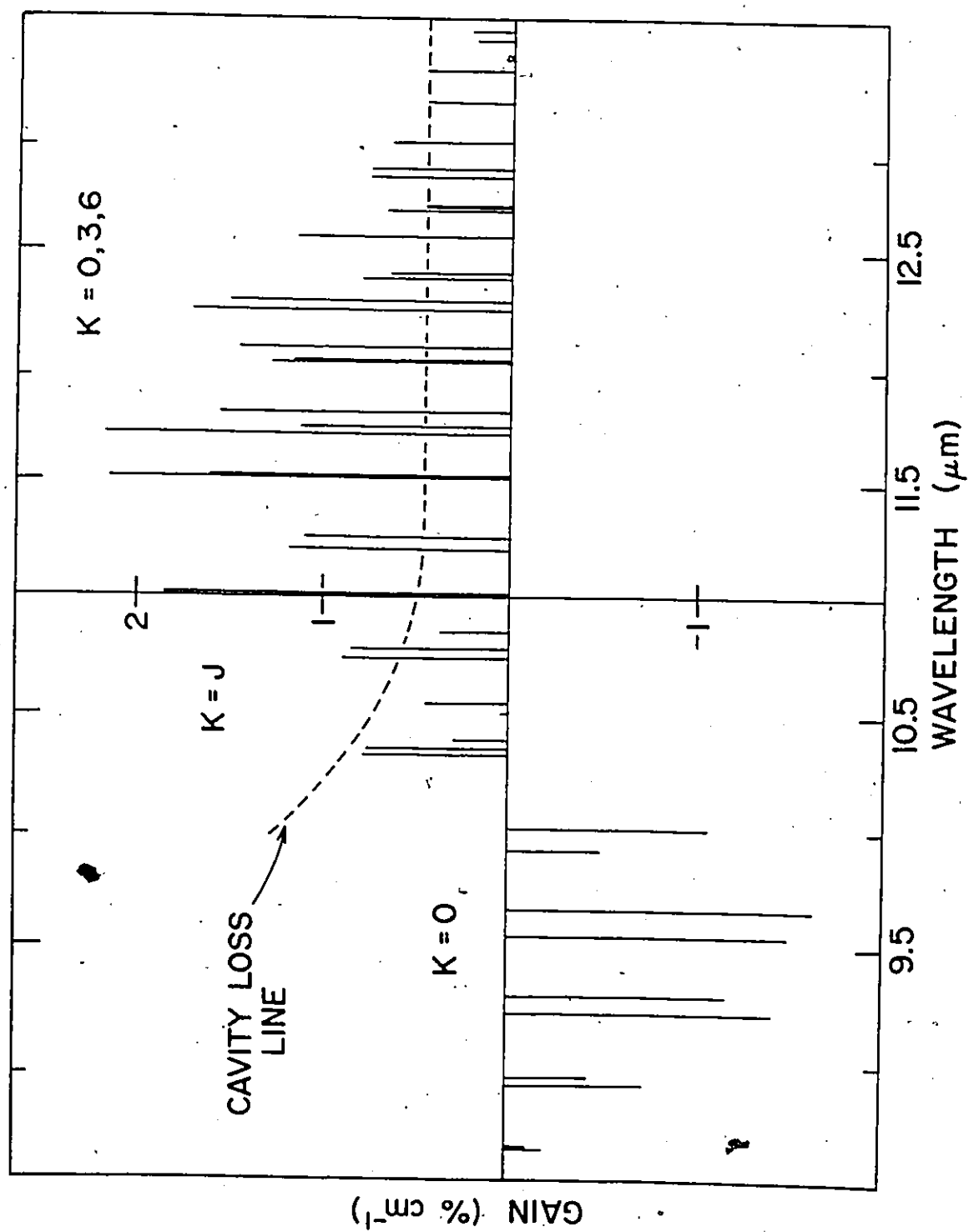
Wavelength ^a (observed) [$\pm 0.001 \mu\text{m}$]	Frequency (observed) [$\pm 0.08 \text{ cm}^{-1}$]	Transition ^b [cm^{-1}]	MIR Power	
			Selective Cavity Rela- tive Power	Optimum [mW]
13.23 ^c	753.9	aP(9,6)-753.590	<1	-
13.15 ^c	760.7	aP(9,3)-760.694	<1	-
12.970	770.98	aP(8,6)-770.914	3	-
12.849	778.28	aP(8,3)-778.290	3	-
12.810	780.61	aP(8,0)-780.568	7	-
12.681	788.55	aP(7,6)-788.510	2	-
12.560	796.19	aP(7,3)-796.134	9	200
12.383	807.54	sP(8,3)-807.472	5	-
12.281	814.23	aP(6,3)-814.241	38	300
12.245	816.62	aP(6,0)-816.651	44	500
12.079	827.91	sP(7,0)-827.878	50	760
12.009	832.70	aP(5,3)-832.635	50	540
11.798	847.57	sP(6,3)-847.578	38	250
11.746	851.36	aP(4,3)-851.327	50	180
11.712	853.84	aP(4,0)-853.818	70	630
11.521	868.00	sP(5,0)-868.000	100	710
11.208	892.22	aP(2,0)-892.157	14	190
11.010	908.21	sP(3,0)-908.199	16	150
10.783	927.34	aQ(6,6)-927.323	38 ^d	160
10.740	930.83	aQ(3,3)-930.757	75 ^d	160

(a) Vacuum wavelength.

(b) From Ref. [45].

(c) These wavelengths were measured in a 1/4 meter monochromator ($\pm 0.5 \text{ cm}^{-1}$).(d) For comparison purposes, these output powers should be reduced by a factor ~ 3 since the transmission of the output coupler triples in this wavelength region.

Fig. 7.3: Calculated gain as a function of wavelength for the P, Q, and R branches in NH_3 . The calculation assumed N_1/N_0 is 1.1, and was carried out for a 1% NH_3/N_2 mixture of 8 Torr. Only lines with $K=0$ (R-branch), $K=J=3,6,9$ (Q-branch), and $K=0,3,6$ (P-branch) are plotted. Also shown is the approximate loss line in the selective cavity, calculated assuming waveguide losses of 0.3%/cm, and coupling losses of ~10% per pass between 11.2 and 13.5 μm . The increase in the loss at shorter wavelength is caused by a transmission increase in the output coupler combined with larger grating losses.



the selective cavity. The dotted line represents the minimum gain required to obtain threshold and was estimated from a combination of loss mechanisms including waveguide propagation losses, output coupler transmission, and grating efficiency. Of the 27 transitions predicted to be above threshold in Fig. 7.3, 20 were observed in the grating tuned cavity of Fig. 7.2. The exceptions were transitions in close proximity to stronger lines and probably these transitions were not resolved by the 12- μm grating. As expected, only lines with $K=3n$ lase in the present system. Note that among the NH_3 lines listed in Table 7.1, the a-type transitions are more abundant than the s-type lines. This effect is due to the inversion splitting between the a and s levels. The splitting is negligible in the ground state (0.8 cm^{-1}) however in the $v_2=1$ state, the inversion splitting is 36 cm^{-1} and leads to significantly higher gain coefficients for the a-transitions than the corresponding s-transitions.

The relative output power listed in Table 7.1 scales approximately with the calculated gain of Fig. 7.3. Further work has been recently performed to measure the small-signal gain on several ortho- NH_3 lines using a tunable diode laser as a probe [81]. The diode laser measurements were made using an experimental setup similar to the one displayed in Fig. 4.2, except that the CO_2 laser frequency is shifted by 180 MHz using the two acousto-optic modulators. Figure 7.4 illustrates a typical amplitude scan of the TDL power versus wavelength taken with 5 W of downshifted cw CO_2 radiation incident upon the waveguide. Note that the presence of the pump radiation induces gain only on the ortho- NH_3 transitions while the para- NH_3


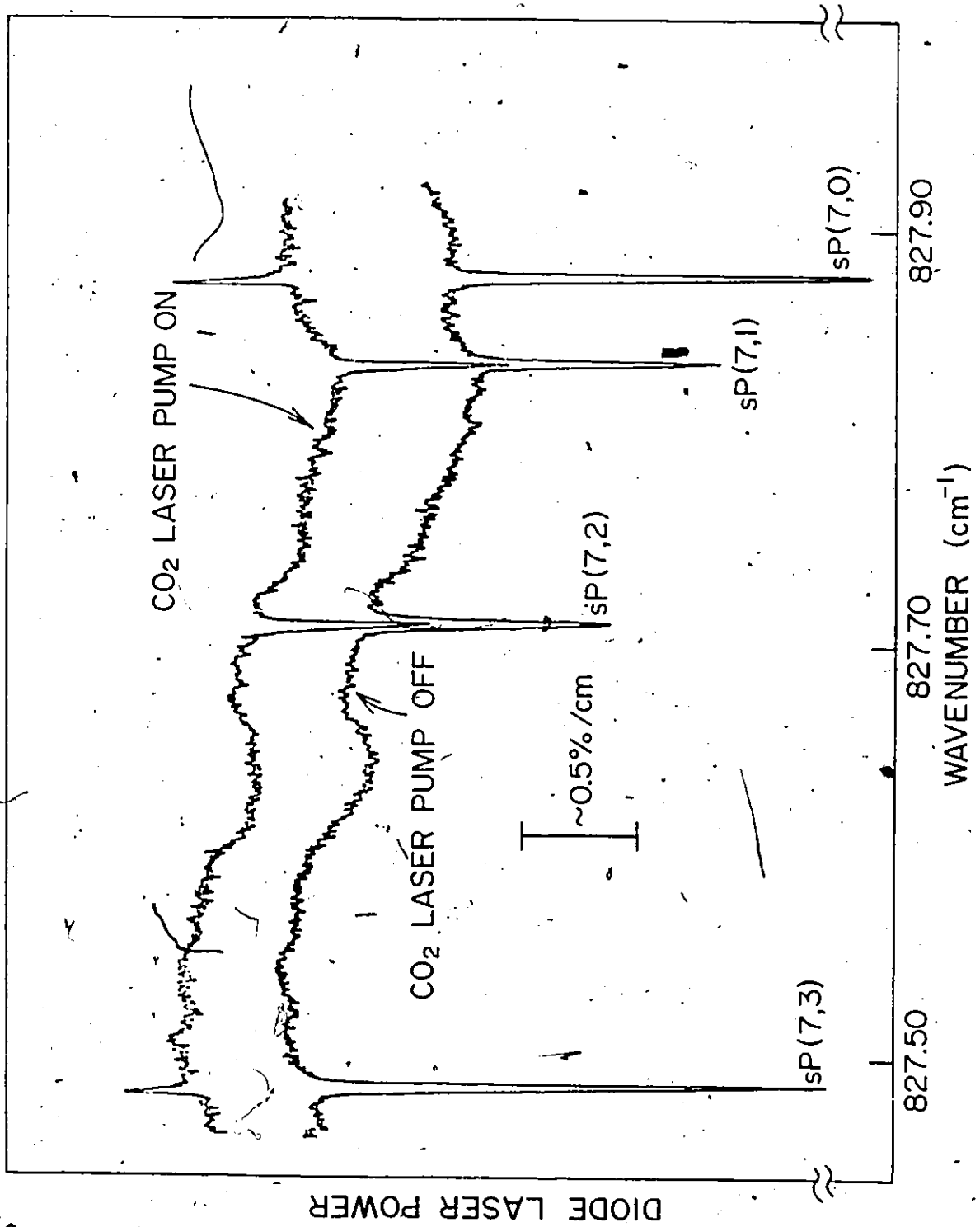


Fig. 7.4: Conventional tunable diode scans of gain and absorption in the $sp(7,K)$ multiplet of NH_3 . 5 W of resonant 9- μm radiation pump a 1% NH_3 in N_2 gas mixture at a total pressure of 5 Torr. The gas is contained in a 2.5-mm bore, 30-cm long waveguide cell. Note that gain only appears on the ortho-lines ($K=3n$).



transitions display a slight decrease in absorption due to the off-resonant pumping of the $\text{SR}(5,1)$ NH_3 transition. This behavior is in agreement with our experimental observations in NH_3 oscillators and confirms the absence of collisional coupling between the ortho- and para-forms of NH_3 . Using the TDL as a probe, detailed measurements of gain coefficients were made for different NH_3 transitions. The results were successfully compared with calculations based on a rate-equation model [82]. The outputs of the theoretical model are the ratio N_1/N_0 and the absolute populations in the vibrational levels. For the average pump intensity of 400 W/cm^2 used in our 1.5-mm bore tube, this model predicts a ratio $N_1/N_0 = 1.02$, in good agreement with our estimated value of $N_1/N_0 = 1.1$. In addition, the TDL measurements have validated the two major conditions used in section 7.2: (1) the fast rotational thermalization in all vibrational levels and (2) the absence of collisional coupling between ortho- and para- NH_3 .

The work described in this chapter was concentrated on developing a detailed understanding of the gain distribution and magnitude of the line-tunable NH_3 laser. As a consequence, the grating-tuned cavity of Fig. 7.2 had only a 1% output coupling. To improve the output power, the grating was replaced by a variety of output couplers having transmissions ranging from 5 to 50%. Line tunability and single line operation could still be obtained by simply changing the cavity length using a piezoelectric translator. Different NH_3 cells were investigated. Waveguide cells with a 1.5-mm bore and 15-cm length or 3-mm bore and 38-cm length were alternated with large diameter cells with lengths as

short as 8 cm. In general, best results were produced with the waveguide cells. Table 7.1 lists the optimum single-line output power observed on the NH_3 lines. These results were obtained with the 3-mm waveguide, NH_3 mixtures between 0.5 and 3% and total gas pressures ranging from 3 to 10 Torr. Output powers as high as 760 mW were measured with only 9 W of pump power and an absorbed power of ~ 3.4 W, i.e., a photon conversion efficiency of $\sim 30\%$. Moreover, threshold pumping powers as low as 1 W were measured* in high-Q cavities where the grating was replaced by a total reflector and an open cell was employed to minimize the 9- and 12- μm propagation losses. Low pump thresholds are of particular importance for producing efficient cw operation on the weaker lines.

7.4 Future Prospects

The line-tunable NH_3 laser described in this chapter is efficient and simple to construct and operate. Good short-term amplitude stability (typically $\sim 0.5\%$) was achieved without any active form of stabilization. It should be relatively easy to scale the output power to several watts on many NH_3 lines by increasing the waveguide length, using a more powerful CO_2 laser and possibly by cooling the waveguide. Our pumping technique is general and cw operation could be extended to para- $^{14}\text{NH}_3$ and both forms of $^{15}\text{NH}_3$.

*The measurements reported here concern line-tunable operation using a buffer gas. In pure NH_3 at low pressures (~ 300 mTorr), lasing only takes place on the coupled $\text{sp}(7,0)$ transition, and 12- μm lasing was observed with pump powers as low as 50 mW.

Table 7.2 lists suitable pump/absorber pairs and the frequency offset, which must be corrected with acousto-optic modulators [83]. The combination of $^{14}\text{NH}_3$ and $^{15}\text{NH}_3$ should provide over 100 cw laser lines between 10.3 and 13.5 μm . Extension to the 16 μm region may be feasible using ND_3 .

There exist several potential applications for this new laser system in fields such as high resolution spectroscopy or heterodyne detection. As emission takes place at the NH_3 line center* Lamb dip experiments can be carried out to stabilize the laser frequency or to make measurements of hyperfine splitting in NH_3 . With a stable NH_3 source, the frequency of a number of NH_3 transitions could be measured accurately, providing secondary frequency standards. Compact ammonia lasers can serve as local oscillators for heterodyne detection. This detection technique has been applied to study molecules such as NH_3 and C_2H_4 in stellar atmospheres using CO_2 or N_2O lasers as local oscillators [85]. Our laser system significantly extends the frequency range available for heterodyne detection in the infrared. One very interesting prospect is to use the 12- μm NH_3 laser to pump a variety of cw FIR NH_3 transitions. NH_3 is regarded as one of the best molecules for FIR lasers [4,86] but has received limited attention in the past due to the lack of exact coincidences between CO_2 pump lines and NH_3

*Line center emission was confirmed by measuring the absorption of several 12- μm lasing transitions in low pressure NH_3 .

Table 7.2

Other Pump/ NH_3 Combinations.

Gas	CO_2 Pump	NH_3 Transition	NH_3 Frequency (cm^{-1})	Shift from CO_2 Laser Line Centre (MHz)
$^{14}\text{NH}_3$	sequence P(7) 9 μm	aR(5,1)	1054.913 ^a	86 ^b
$^{15}\text{NH}_3$	regular R(10) 9 μm	aR(6,0)	1071.889 ^c	-157
$^{15}\text{NH}_3$	regular R(42) 10 μm	aR(2,0)	988.649	-72 ^c , -26 ^d
$^{15}\text{NH}_3$	sequence R(7) 9 μm	aR(6,5)	1066.433 ^c	120

^aReference [45].^bReference [53].^cReference [84].^dIf the pump offset is as little as 26 MHz (Reference [70]) this NH_3 transition may not require the use of acousto-optic modulators.

absorption lines*. The new line-tunable 12- μm NH_3 laser overcomes this limitation and provides an ideal pump source for FIR NH_3 lasers operating in the 60-400 μm region [88].

7.5 Summary

This chapter has dealt with the operation of the first line-tunable cw NH_3 laser in the mid-infrared. The success of our pumping scheme is based on pumping NH_3 at line center by shifting the pump frequency in resonance with the absorbing transition. The downshifted radiation optically pumps mixtures of NH_3 in N_2 , and creates a vibrational inversion in the $\nu_2=1$ mode of NH_3 . A simple model assuming rotational thermalization fully accounts for the characteristics of the NH_3 laser. Even at this early stage of development, energy conversion efficiencies of ~18% are measured using a waveguide cell. The operation of cw line-tunable NH_3 lasers is not limited to ortho- $^{14}\text{NH}_3$ and the use of the para-form and other isotopes should provide a new generation of lasers in the mid-infrared. Section 7.4 discusses a few potential applications in spectroscopy for a line-tunable MIR laser. The list is not exhaustive and this type of laser should prove to be a valuable tool in the future.

*Where an exact coincidence does exist, very efficient FIR lasing has been obtained, with pump power thresholds as low as 10 mW [87].

CHAPTER 8

CONCLUSIONS

In this chapter, we outline the important conclusions which can be drawn from the work described in this thesis. The aim of this work was to explore the possibility of producing cw laser action in the mid-infrared using the optical pumping technique, and thereafter to identify through a comparison of a model with experiment the physical mechanisms involved in the lasing process. Optical pumping is demonstrated to be a very attractive technique for developing new cw laser sources since it is energy selective, efficient and easy to implement. Prior to this work, only a handful of powerful cw sources existed between 10 and 30 μm [89,90]. Tens of new cw lasers yielding high output powers are now readily available in this region using fairly simple pumping schemes. The new cw sources are highly efficient and the techniques described in this thesis promise to be widely applicable in the entire mid-infrared spectrum. The significance of our experiments was discussed in the various sections of Chapters 3 to 7, and in a more condensed form in Refs. [91-97]. This chapter is concerned with giving a brief overall summary of the research accomplished in this thesis.

The search for optically-pumped cw MIR lasers was initiated by examining the threshold behavior of pulsed 12- μm NH_3 lasers. By optimizing the design of the MIR cavity, we were able to reduce the pumping power requirements of these lasers by several orders of magnitude

to levels accessible with cw CO_2 lasers. It quickly became apparent that the low pumping powers combined with the large pump offset frequencies used in our experiments were not sufficient to produce a population inversion. The measurements of the NH_3 lasing frequency clearly demonstrated that a two-photon transition is the basic mechanism involved in the 12- μm lasing process. Indeed, it is only because the Raman process can produce gain in the absence of a population inversion that low pumping thresholds are possible for these off-resonantly pumped transitions. The strong correlation between the magnitude of the pump offset frequency and the pump threshold value was a further indication of the Raman nature of the gain. These experiments led to the establishment of conditions for, and subsequently the construction of, the first optically-pumped cw laser to operate on a vibrational-rotational transition. An important factor which contributed to the success of this experiment was the substitution of the linear pumping geometry used for the pulsed experiments by a ring configuration. This new arrangement eliminated the strong feedback between the MIR cavity and the CO_2 laser and provided stable pumping powers.

A detailed understanding of the lasing process was achieved by measuring the 12- μm small-signal gain in a separate amplifier cell using a tunable diode laser as a probe. The dependence of the 12- μm gain on pump intensity, pump offset, pressure and polarization was examined and the results described in Chapter 4 were found to be in good agreement with a model describing the interaction of two laser fields with a three-level system. A major objective of this investigation was to provide an accurate and detailed test of the model, a

task which had never been accomplished in the mid-infrared region. In addition to this fundamental study, the TDL measurements were a crucial step in identifying the parameters which influence the gain. In particular, our experiment emphasized the importance of the pump intensity in determining the magnitude of the gain. The Raman gain was shown to be proportional to pumping intensity and this characteristic was fully exploited by using a waveguide tube to contain the NH_3 gas. The high intensities produced in the waveguide cell gave rise to large single pass amplification, of particular importance for the design of a high power cw 12- μm Raman laser.

Based on the findings of Chapter 4, we improved our initial cavity design and constructed a 12- μm waveguide laser. Waveguides with different bores and lengths were investigated and the results were summarized in Chapter 5. Quantum conversion efficiencies as high as 45% were obtained in an optimized waveguide resonator. In other words, for every two 9- μm photons entering the waveguide cell, one 12- μm photon is coupled out of the resonator. These photon conversion efficiencies are among the highest ever reported for an optically-pumped (both pulsed and cw) laser [10,17,98-100]. The use of a waveguide tube was undoubtedly a key element in achieving these results. A 12- μm output power of 10.5 W was measured for a maximum available pump power of 38 W. Even at these pumping levels, the 12- μm output was still increasing with the input CO_2 power indicating that the 12- μm laser can be scaled to higher powers by simply using a more powerful pump. In addition to providing high output powers, the optimization of the 12.08- μm cavity enabled threshold pumping powers

as low as 1 W to be obtained. Low pump thresholds are of particular importance when the pump frequency is far from the absorbing line center. To test the limits of the present system, we chose to pump an NH_3 transition offset by 1.4 GHz from the nearest CO_2 pump line. CW lasing was obtained for the first time at 12.18 μm , although the laser was operating near threshold. Clearly, the high pumping intensities produced in a waveguide resonator have considerably extended the range of pump offset over which cw operation is practical. As there are many NH_3 transitions with pump offset frequencies smaller than 1.4 GHz our cavity arrangement should provide several new off-resonantly pumped cw NH_3 transitions in the near future.

To optimize the energy extraction from the 12- μm Raman laser, it is essential to identify the role played by the different gain saturation mechanisms. There exist two major processes responsible for the reduction of the Raman gain; (1) the conversion of 9- μm photons to 12- μm photons as the pump beam propagates along the waveguide cell and (2) a decrease in the population difference which drives the Raman gain. The latter is caused by the transfer of a large fraction of the pumped level population to the lower laser level. In Chapter 6, the gain saturation effect is investigated for the first time by pumping a waveguide amplifier with intense 9- and 12- μm fields. Our measurements show that under conditions similar to those present in 12- μm oscillators, the Raman small-signal gain is reduced substantially without a corresponding change in the pump power. These results indicate that pump depletion is not the dominant saturation mechanism, in agreement with the lasing behavior observed in high power 12- μm

systems. The saturation measurements are accounted for using the simple model described in Chapter 2 and an effective relaxation rate (γ) for the individual level populations. Our analysis emphasizes the importance of the relaxation rate γ in determining the relative contribution of population transfer and pump depletion in reducing the gain in 12- μm lasers.

The results reported in this thesis have clearly demonstrated that off-resonant pumping is capable of producing very efficient ^{cw} laser operation. However, the technique is restricted somewhat by the fact that every lasing transition requires the use of a different pump line. Chapter 7 describes a different approach whereby cw operation on tens of NH_3 transitions is obtained between 10.7 and 13.3 μm by using a single CO_2 pump line. The success of our pumping scheme relies on the following two factors: (1) efficient pumping of the absorbing transition and (2) the presence of fast rotational relaxation rates in the vibrational levels. Very efficient pumping was accomplished by shifting the R(30) 9- μm CO_2 pump line into resonance with the sR(5,0) NH_3 absorbing transition using acousto-optic modulators. The down-shifted CO_2 radiation allowed the transfer of a significant fraction of the NH_3 ground state population to the $v_2=1$ vibrational level. The fast rotational relaxation rates obtained by adding a buffer gas (N_2) to NH_3 ensured rotational equilibrium inside the different vibrational levels. As a result, gain was produced in the entire P- and Q-branches. The dynamics of this new laser system are explained using a simple model which assumes complete rotational thermalization.

It is clear from the experiments reported in Chapters 3 to 6 that the creation of a vibrational inversion would not have been possible by pumping the $sR(5,0)$ transition off-resonance (contrary to the situation with pulsed lasers). One of the innovative ideas developed in this work was to utilize acousto-optic modulators to compensate for a pump offset frequency and the results presented in Chapter 7 indicate the great potential of such a technique for generating new line-tunable cw MIR lasers.

Although the research described in this thesis is concerned entirely with optically-pumped $^{14}\text{NH}_3$, most of the pumping schemes reported in this work can be applied to other NH_3 isotopes and possibly other molecules (e.g., CF_4 and CH_3F) [101]. In particular, the models validated by our experiments can be used to predict the gain attainable with molecules other than NH_3 . The work presented in this thesis has opened the way to a new generation of cw lasers in the mid-infrared and it is expected that this research will be of considerable value in the future development of cw MIR lasers.

APPENDIX A

DENSITY MATRIX SOLUTION

Heppner *et al.* [37] have derived an explicit solution of the density matrix equation system for the general case of arbitrary field strengths and broadenings. This appendix follows the treatment given in Heppner *et al.* and gives the explicit expressions used in our computer evaluations of the gain. The CGS system of units is employed in this appendix. The MIR gain for molecules moving with axial velocity v is given by

$$\alpha_{\text{mir}}(M, v) = k_{\text{mir}} \text{Im}(S_1(M, v) r_{10}(M, v) + S_2(M, v) r_{21}(M, v)) \quad (2.6)$$

where the various symbols were defined in section 2.4.1. This expression shows that the MIR gain is the sum of two different contributions. The first term is proportional to the population difference between the upper and lower laser level (r_{10}), while the second term is driven by the population difference between the pumped level and the lower laser level (r_{21}). S_1 and S_2 are given by

$$\begin{aligned} S_1(M, v) &= 4\pi \frac{|\mu_{20}|^2}{\hbar N} (|\alpha|^2 + L_1 R - |\beta|^2) \\ S_2(M, v) &= 4\pi \frac{|\mu_{20}|^2}{\hbar N} (L_1 R - |\beta|^2) \end{aligned} \quad (A.1)$$

where the following symbols are used

$$\alpha = \mu_{10} A_p(z) / \hbar, \quad \beta = \mu_{02}^* A_{\text{mir}}^*(z) / \hbar$$

$$A_p(z) = E_p / 2 \exp(-i(k_{\text{pump}} z - \phi_1))$$

$$\begin{aligned}
A_{\text{mir}}(z) &= E_{\text{mir}}/2 \exp(-i(\epsilon k_{\text{mir}} z - \phi_2)) \\
L_1 &= \omega_p - \Omega_{01} - k_p v + i\gamma_{10} \\
L_2 &= -\omega_{\text{mir}} + \Omega_{02} + \epsilon k_{\text{mir}} v + i\gamma_{20} \\
R &= (\omega_p - \Omega_{01}) - (\omega_{\text{mir}} - \Omega_{02}) - (k_p - \epsilon k_{\text{mir}})v + i\gamma_{12} \\
N &= L_1 L_2 R - L_1 |\alpha|^2 - L_2 |\beta|^2 \quad (\text{A.2})
\end{aligned}$$

ϕ_1 and ϕ_2 are arbitrary phase constants and the other symbols are defined in Chapter 2. Note that in a first approximation, R gives the difference between the pump and lasing offset frequencies and thus becomes resonant at the Raman condition. Moreover, R also accounts for the residual Doppler width between the 9- and 12- μm radiations which determines the Raman linewidth at low pressure. The population differences induced by the fields are given by

$$\begin{aligned}
r_{10}(M, v) &= (J_{22} r_{10}^0 + J_{12} r_{20}^0) / (J_{11} J_{22} - J_{12} J_{21}) \\
r_{20}(M, v) &= (J_{21} r_{10}^0 + J_{11} r_{20}^0) / (J_{11} J_{22} - J_{12} J_{21}) \\
r_{21}(M, v) &= r_{20}(M, v) - r_{10}(M, v)
\end{aligned}$$

with

$$\begin{aligned}
J_{11} &= 1 - \frac{2|\alpha|^2}{\gamma_0} \text{Im}\left\{ \left[\frac{2\gamma_{01}}{\gamma_1} (L_2 R - |\alpha|^2) + |\beta|^2 \right] / N \right\} \\
J_{12} &= \frac{2|\beta|^2}{\gamma_0} \text{Im}\left\{ \left[\frac{2\gamma_{10}}{\gamma_1} |\alpha|^2 + L_1 R - |\beta|^2 \right] / N \right\} \\
J_{21} &= \frac{2|\alpha|^2}{\gamma_0} \text{Im}\left\{ \left[\frac{2\gamma_{20}}{\gamma_2} |\beta|^2 + L_2 R - |\alpha|^2 \right] / N \right\} \\
J_{22} &= 1 - \frac{2|\beta|^2}{\gamma_0} \text{Im}\left\{ \left[\frac{2\gamma_{02}}{\gamma_2} (L_1 R - |\beta|^2) + |\alpha|^2 \right] / N \right\} \quad (\text{A.3})
\end{aligned}$$

where the population difference between levels i and j in the absence

of the fields is denoted by

$$r_{ij}^0 = \rho_{ii}^0/g_i - \rho_{jj}^0/g_j$$

with

$$g_i = 2J_i + 1$$

for the degeneracy of level J_i . In this model, the M-degeneracy of the molecular levels was removed by dividing the total level population equally among the different M sub-levels and by treating them separately. In such a case, the M-dependence of the dipole matrix elements must be taken into account. The direction-cosine matrix elements in the R and P branches are given as follows [25]:

$$\begin{aligned} R(J,K) : |\mu_{ij}|^2 &= \mu^2 \frac{[(J+1)^2 - K^2][(J+1)^2 - M^2]}{(J+1)^2(2J+1)(2J+3)} \\ P(J,K) : |\mu_{ij}|^2 &= \mu^2 \frac{(J^2 - K^2)(J^2 - M^2)}{J^2(2J-1)(2J+1)} \end{aligned} \quad (A.4)$$

where μ is the molecular dipole moment.

The equations (A.1) to (A.4) are used to calculate the gain for molecules belonging to the M sub-level and moving at a velocity v . The total gain expression is given in Chapter 2 (see eq. 2.7) and includes the integration over a Doppler velocity profile and sums over all M-values. A computer code was implemented to evaluate the gain and Fig. 2.4 displays an example of a gain calculation.

REFERENCES

1. T.Y. Chang and T.J. Bridges, Opt. Commun. 1, 423 (1970).
2. D.J.E. Knight, "Ordered list of far-infrared lines (continuous, >12 μm)", Nat. Phys. Lab. Rep. Qu 45 (1st revision) (1981).
3. K.J. Button, Reviews of Infrared and Millimeter Waves, (Plenum, New York, 1982).
4. E.J. Danielewicz and C.O. Weiss, IEEE J. Quantum Electron. QE-14, 705 (1978).
5. T.A. DeTemple and E.J. Danielewicz, Infrared and Millimeter Waves, Vol. 7; Ch. 1, (K.J. Button editor, Academic Press, New York, 1983).
6. R.V. Ambartzumian, V.S. Letokhov, and C.B. Moore, Chemical and Biochemical Applications of Lasers, Vol. III, (C.B. Moore editor, Academic Press, New York, 1977).
7. "Laser-Induced Chemistry", Chapter 1 in Advances in Laser Chemistry, Springer, Ser. Chem. Phys. No. 3 (A.H. Zewail editor, Springer-Verlag, Berlin 1978).
8. "Laser Photochemistry and Diagnostics", Report on a National Science Foundation/Department of Energy Seminar, June 4-5, 1979.
9. R.A. McClatchey, J.E. Selby, "AFCRL Atmospheric Attenuation of Laser Radiation from 0.76 to 31.25 μm ", AFCRL Report 74-0003 (1974).
10. T.Y. Chang and O.R. Wood II, Appl. Phys. Lett. 21, 19 (1972).
11. T.Y. Chang and O.R. Wood II, Appl. Phys. Lett. 22, 93 (1973).
12. H.R. Schlossberg and H.R. Fetterman, Appl. Phys. Lett. 26, 316 (1975).

13. W.E. Barch, H.R. Fetterman, and H.R. Schlossberg, Opt. Commun. 15, 358 (1975).
14. T.Y. Chang and J.D. McGee, Appl. Phys. Lett. 28, 526 (1976).
15. C.R. Jones, Laser Focus 14, August (1978), pp. 68.
16. R.G. Harrison and P.K. Gupta, Infrared and Millimeter Waves, Vol. 7, Ch. 2, (K.J. Button editor, Academic Press, New York, 1983).
17. P.K. Gupta, A.K. Kar, M.R. Taghizadeh, and R.G. Harrison, Appl. Phys. Lett. 39, 32 (1981).
18. B. Walker, G.W. Chantry, and D.G. Moss, Opt. Commun. 23, 8 (1977),
19. F.A. Al-Watban, R.G. Harrison, J.G. Crowder, and C.R. Pidgeon, J. Phys. D: Appl. Phys. 10, L167 (1977).
20. J.J. Tiee and C. Wittig, J. Appl. Phys. 49, 61 (1978).
21. N. Skribanowitz, I.P. Herman, and M.S. Feld, Appl. Phys. Lett. 21, 466 (1972).
22. E.J. Danielewicz, E.G. Malk, and P.D. Coleman, Appl. Phys. Lett. 29, 557 (1976).
23. T.Y. Chang and J.D. McGee, Appl. Phys. Lett. 29, 725 (1976).
24. G. Herzberg, Infrared and Raman Spectra of Polyatomic Molecules (D. Van Nostrand, New York, 1947).
25. C.H. Townes and A.L. Schawlow, Microwave Spectroscopy (Dover, New York, 1975).
26. K. Gullberg, B. Hartmann, and B. Kleman, Phys. Scripta 8, 177 (1973).
27. T. Oka, J. Chem. Phys. 48, 4919 (1968).
28. T. Oka, J. Chem. Phys. 49, 3135 (1968).
29. J.O. Henningsen and H.G. Jensen, IEEE J. Quantum Electron. QE-11,

248 (1975).

30. J.R. Tucker, Opt. Commun. 16, 209 (1976).
31. R.J. Temkin and D.R. Cohn, Opt. Commun. 16, 213 (1978).
32. M.S. Feld and A. Javan, Phys. Rev. 177, 540 (1969).
33. R.L. Panock and R.J. Temkin, IEEE J. Quantum Electron. QE-13, 425 (1977).
34. D. Seligson, M. Ducloy, J.R.R. Leite, A. Sanchez, and M.S. Feld, IEEE J. Quantum Electron. QE-13, 468 (1977).
35. Z. Drozdowicz, R.J. Temkin, and B. Lax, IEEE J. Quantum Electron. QE-15, 170, (1979).
36. T.A. DeTemple, Infrared and Millimeter Waves, Vol. 1, Ch. 3, (K.J. Button editor, Academic Press, New York, 1979).
37. J. Heppner, C.O. Weiss, U. Hübner, and G. Schinn, IEEE J. Quantum Electron. QE-16, 392 (1980).
38. M. Sargent III, M.O. Scully, and W.E. Lamb Jr., Laser Physics, (Addison-Wesley, Massachusetts, 1974).
39. J.R.R. Leite, M. Ducloy, A. Sanchez, D. Seligson, and M.S. Feld, Phys. Rev. Lett. 39, 1465 (1977).
40. C. Rolland, M.Sc. thesis, McMaster University, 1980.
41. F.W. Taylor, J. Quant. Spectrosc. Radiat. Transfer. 13, 1181 (1973).
42. K. Shimoda, Y. Ueda, and J. Iwahori, Appl. Phys. 21, 181 (1980).
43. S. Urban, V. Spirko, D. Papousek, J. Kauppinen, S.P. Belov, L.I. Gershtein, and A.F. Krupnov, J. Mol. Spectrosc. 88, 274 (1981).
44. R.L. Poynter and J.S. Margolis, Molec. Phys. 48, 401 (1983).
45. R.L. Poynter and J.S. Margolis, Molec. Phys. 51, 393 (1984).
46. D.C. McKean and P.N. Schatz, J. Chem. Phys. 24, 316 (1956).

47. T. Shimizu, F.O. Shimizu, R. Turner, and T. Oka, J. Chem. Phys. 55, 2822 (1971).
48. M.M.T. Loy, Phys. Rev. Lett. 32, 814 (1974).
49. J.D. Wiggins, Z. Drozdowicz, and R.J. Temkin, IEEE J. Quantum Electron. QE-14, 23 (1978).
50. E.D. Shaw and C.K.N. Patel, Opt. Commun. 27, 419 (1978).
51. B.I. Vasilev, A.Z. Grasyuk, A.P. Dyadkin, A.N. Sukhanov, and A.B. Yastrebkov, Sov. J. Quantum Electron. 10, 64 (1980).
52. K. Midorikawa, I. Matsuda, M. Obara, and T. Fujioka, Opt. Commun. 32, 447 (1980).
53. T.A. Znotins, J. Reid, B.K. Garside, and E.A. Ballik, Opt. Lett. 5, 528 (1980).
54. J.P. Sattler, L.S. Miller, and T.L. Worchesky, J. Mol. Spectrosc. 88, 347 (1981).
55. J. Reid and K. Siemsen, J. Appl. Phys. 48, 2712 (1977).
56. S.J. Petuchowski, A.T. Rosenberger, and T.A. DeTemple, IEEE J. Quantum Electron. QE-13, 476 (1977).
57. K. Midorikawa, I. Matsuda, T. Nakazawa, M. Obara, and T. Fujioka, Opt. Lett. 6, 177 (1981).
58. P. Minguzzi, M. Tonelli, A. Carrozzi, and A. Di Lieto, J. Mol. Spectrosc. 96, 294 (1982).
59. G.D. Willenberg, U. Hübner, and J. Heppner, Opt. Commun. 33, 193 (1980).
60. J. Heppner and U. Hübner, IEEE J. Quantum Electron. QE-16, 1093 (1980).
61. R. Marx, U. Hübner, I. Abdul-Halim, J. Heppner, Y.-C. Ni, G.-D.

- Willenberg, and C.O. Weiss, IEEE J. Quantum Electron. QE-17, 1123 (1981).
62. S.J. Petuchowski and T.A. DeTemple, Opt. Lett. 6, 227 (1981).
63. D.K. Mansfield, A. Semet, and L.C. Johnson, Appl. Phys. Lett. 37, 688 (1980).
64. P. Wazen and J.-M. Lourtioz, Opt. Commun. 47, 137 (1983).
65. P. Wazen and J.-M. Lourtioz, Appl. Phys. B 31, 105 (1983).
66. R.L. Abrams, IEEE J. Quantum Electron. QE-8, 838 (1972).
67. D.R. Hall, E.K. Gorton, and R.M. Jenkins, J. Appl. Phys. 48, 1212 (1977).
68. E.A.J. Marcatili and R.A. Schmeltzer, Bell Syst. Tech. J. 43, 1783 (1964).
69. F. Julien, P. Wazen, J.-M. Lourtioz and T.A. DeTemple, IEEE J. Quantum Electron. QE-19, 1654 (1983).
70. E.M. Frank, C.O. Weiss, K. Siemsen, M. Grinda, and G.D. Willenberg, Opt. Lett. 7, 96 (1982).
71. G.D. Willenberg, J. Heppner, and F.B. Foote, IEEE J. Quantum Electron. QE-18, 2060 (1982).
72. A. Yariv, Quantum Electronics, Second Edition (John Wiley & Sons, New York, 1975).
73. T. Oka, private communication (1984).
74. J.C. Polanyi, Appl. Opt. supplement 2 of Chemical Lasers, 109 (1965).
75. A.L. Golger and V.S. Letokhov, Sov. J. Quant. Electron. 3, 15 (1973).
76. J.S. Goela and T.F. Morse, Opt. Lett. 4, 375 (1979).

77. S.M. Fry, Opt. Commun. 19, 320 (1976).
78. N. Yamabayashi, T. Yoshida, K. Miyazaki, and K. Fujisawa, Opt. Commun. 30, 245 (1979).
79. H. Tashiro, K. Suzuki, K. Toyoda, and S. Namba, Appl. Phys. 21, 237 (1980).
80. H.D. Morrison, Ph.D. thesis, McMaster University, 1984.
81. R.L. Sinclair, J. Reid, H.D. Morrison, B.K. Garside, and C. Rolland, accepted for publication in J. Opt. Soc. Am. B, February (1985).
82. H.D. Morrison, J. Reid, and B.K. Garside, accepted for publication in IEEE J. Quantum Electron., September (1984).
83. The use of acousto-optic modulators to shift the pump frequency into coincidence with an absorption transition can also be applied to optically-pumped FIR systems.
84. G. DiLorenzo, L. Fusina, A. Trombetti, and I.M. Mills, J. Mol. Spectrosc. 92, 298 (1982).
85. A.L. Betz, Laser Spectroscopy V, Part I, Springer Ser. in Optical Sciences (A.R.W. McKellar, T. Oka, B.P. Stoicheff editors, Springer-Verlag, Berlin, 1981) pp. 81.
86. P.D. Coleman, J. Opt. Soc. Am. 67, 894 (1977).
87. R.A. Wood, A. Vass, C.R. Pidgeon, and W.J. Firth, Opt. Commun. 35, 105 (1980).
88. N. Yamabayashi, K. Fukai, K. Miyazaki, and K. Fujisawa, Appl. Phys. B26, 33 (1981).
89. B.L. Wexler, T.J. Manuccia, and R.W. Waynant, Appl. Phys. Lett. 31, 730 (1977).
90. V.A. Akinov, A. Yu. Volkov, A.I. Demin, E.M. Kudryavtsev, N.B.

- Rodionov, and V.F. Sharkov, Sov. J. Quantum Electron. 13, 556 (1983).
91. C. Rolland, J. Reid, and B.K. Garside, IEEE J. Quantum Electron. QE-18, 182 (1982).
 92. C. Rolland, B.K. Garside, and J. Reid, Appl. Phys. Lett. 40, 655 (1982).
 93. C. Rolland, J. Reid, B.K. Garside, P.E. Jessop, and H.D. Morrison, Opt. Lett. 8, 36 (1983).
 94. C. Rolland, J. Reid, B.K. Garside, H.D. Morrison, and P.E. Jessop, Appl. Opt. 23, 87 (1984).
 95. C. Rolland, J. Reid, and B.K. Garside, Appl. Phys. Lett. 44, 380 (1984).
 96. C. Rolland, J. Reid, and B.K. Garside, Appl. Phys. Lett. 44, 725 (1984).
 97. C. Rolland, B.K. Garside, and J. Reid, submitted to Appl. Opt. June (1984).
 98. E.J. Danielewicz, T.A. Galantowicz, F.B. Foote, R.D. Reel, and D.T. Hodges, Opt. Lett. 4, 280 (1979).
 99. R.A. Wood, A. Vass, C.R. Pidgeon, M.J. Colles, and B. Norris, Opt. Commun. 33, 89 (1980).
 100. F. Julien and J.-M. Lourtioz, Opt. Commun. 38, 294 (1981).
 101. J. Telle, IEEE J. Quantum Electron. QE-19, 1469 (1983).